Transpressional kinematics of ductile shear zones and its implications for emplacement of granitic rocks in the western margin of the South Delhi Fold Belt, Rajasthan, India: a field-based study

Thesis submitted by

AYAN KUMAR SARKAR

INDEX No.: 166/18/Geol. Sc./26

Submitted to
Jadavpur University
For the degree of Doctor of Philosophy (Science)

Department of Geological Sciences

Jadavpur University

Kolkata-700032, India

August, 2023

যাদবপুর বিশ্ববিদ্যালয়
কলকাতা - ৭০০০৩২, ভারত

JADAVPUR UNIVERSITY
KOLKATA-700 032, INDIA

FACULTY OF SCIENCE : DEPARTMENT OF GEOLOGICAL SCIENCES

CERTIFICATE FROM THE SUPERVISOR

This is to certify that the thesis entitled "**Transpressional kinematics of ductile shear zones and its implications for emplacement of granitic rocks in the western margin of the South Delhi Fold Belt, Rajasthan, India: a field-based study**", submitted by **Mr. Ayan Kumar Sarkar,** who got his name registered on **12.09.2018** for the award of **PhD (Science)** degree of Jadavpur University, is absolutely based upon his own work under the supervision of **Dr. Sadhana M. Chatterjee** and that neither this thesis nor any part of it has been submitted for either any degree/ diploma or any other academic award anywhere before.

Sadhana M. Chatterjee
28/08/2023

Dr. Sadhana M Chatterjee
Associate Professor
Department of Geological Sciences
Jadavpur University
Kolkata-700032, India

Dr. Sadhana M Chatterjee
Associate Professor
Department of Geological Sciences
Jadavpur University
Kolkata-700 032

Website : www.jaduniv.edu.in
E-mail : hod.geology@jadavpuruniversity.in

HOD Phone : 033 2457 2719
Office : 033 2457 2268

Dedicated to my Parents

and Madam

Acknowledgements

My foremost acknowledgement is dedicated to my esteemed supervisor, Dr. Sadhana M. Chatterjee, an Associate Professor in the Department of Geological Sciences at Jadavpur University, Kolkata. Her unwavering support, proactive guidance, and wealthy ideas, valuable beyond estimation, have been throughout this accomplishment. Completion of this work without her indispensable counsel would have been a legendary enthusiasm.

I am thankful to the Head of this Department of Geological Sciences as well as to all other esteemed faculty members, persistent research scholars and dedicated non-teaching staffs who have rendered their heartiest assistance and excellent support throughout the process of my project. I am really indebted to the INSPIRE-Fellowship program under the aegis of the Department of Science and Technology for their generous support.

Furthermore, my appreciation is extended to the Department of Geology, Geophysics at IIT, Kharagpur and Acme Laboratories in Canada for kind access to their cutting-edge laboratory facilities, enabling the execution of EPMA and Whole-rock analysis on the samples. Special thanks are also due to Activation Laboratories in Ancaster, Ontario, Canada for their proficient execution of LA-MC-ICP-MS U-Pb age analysis on Zircons.

I am deeply overwhelmed by my fellow labmates namely Anirban Manna, Dr. Alip Roy, Dr. Subhrajyoti Das, Dr. Manideepa Roy Choudhury and Dr. Vibha Katiyar who have voluntarily offered unbelievable assistance in diverse ways contributing significantly to the successful culmination of this work.

Lastly, I am immensely grateful to my cherished family members, friends, and lab juniors too who have undoubtedly supported me with encouragement as a constant source of motivation from the beginning to the end of this journey.

Ayan Kumar Sarkar

Contents

Abstract:

Granite emplacement within transpressional shear zones is a complex geological process that plays a crucial role in the structural and tectonic evolution of Earth's crust. Transpressional shear zones represent regions where compressional and strike-slip tectonic forces interact, leading to the deformation and displacement of crustal rocks. The emplacement of granite bodies within these zones is a result of an intricate system that interplays between magmatic processes and tectonic stresses. Several tectonic models on the emplacement of granites have been proposed for different tectonic settings. However, to understand the tectonic framework, different approaches have to be done, such as analyses of geometry and kinematics of shear zone structures and detailed analyses of petrological, geochemical and geochronological factors of the affected rocks. In the north western Indian shield, the NE-SW trending South Delhi Fold Belt (SDFB) is a multiply folded and poly-metamorphosed rock of the Proterozoic age. Phulad Shear Zone (PSZ) is described as a terrane boundary shear zone that separates the SDFB to the east and Marwar craton to the west. The PSZ has developed in a ductile transpressive regime with a top-to-the-NNW reverse sense of movement during 810 Ma. The present study deals with the deformation of PSZ and a variably deformed porphyritic granite named Phulad granite that occurs about 200 by 6 km along and across the PSZ. This shear zone is defined by steep southeasterly dipping mylonitic foliation and strong downdip stretching lineation. The PSZ shows regional NE-SW trends with small bends of N-S orientation. The Phulad granite is characterized by a bi-modal grain size population with prominent euhedral grains of feldspar clasts (2-6 cm long) in a fine-grained (<3mm) mosaic of recrystallized feldspar and quartz aggregates. It consists of phenocrysts of K-feldspar that show characteristic features of magmatic origin. Mesoscopic field relations show evidence of

magmatic fabric in the studied granite. The granite also preserves tectonic foliation parallel to this magmatic fabric. Strong foliation developments with a mean attitude of 23˚/77˚E and prominent stretching lineation (both gentle and steep) have been developed in the granitic rock. A detailed study of structural elements of Phulad granite and PSZ demonstrates a similarity in geometry and style, signifying that the deformation in both units is synchronous. The study of microstructures reveals a series of magmatic, submagmatic, high-temperature and solid-state deformation features in this granite, which further suggests that the granite was emplaced syn-tectonically. A detailed study of structural elements suggests that Phulad granite has formed during the regional deformation in the country rock shear zone prior to its complete crystallization. The present study indicates that the N-S orientation within the PSZ acted as releasing bends and provided the space required for the emplacement of the Phulad granite in a transpressional regime. Geochemical investigation suggests the Phulad granite was emplaced syn-tectonically from a predominant crustal source. Monazite chemical age data and conventional zircon age data suggest a magmatic age of 819.1±4 and 818±18 Ma, respectively. Integrating micro-meso and macro scale structures along with the geochemistry and geochronology of the Phulad granite, it is suggested that the Phulad granite acted as a stitching pluton along the PSZ during the suturing of the Marwar craton with the remaining part of India around 810- 820 Ma.

Chapter 1

Introduction

1.1 Introduction:

Studies of granitic rocks in transpressional orogens indicate that the tectonic features may act as fundamental controls on the ascent and emplacement of the granitic rocks. Regional tectonics and granite generation may be consistently linked processes with granitic melts influencing crustal behaviour during their ascent within actively deforming shear zones. Thus, study of pluton emplacement could give valuable information about the regional context. Significant research into the emplacement of granitic rocks in transpressional orogens suggests that tectonics play a crucial role in governing the rise and placement of these granitic formations (Hutton, 1988a, 1997; Hutton and Reavy, 1992; McCaffrey, 1992; Saint-Blanquat et al., 1998, 2011). Syntectonic granite emplacements in broadly transpression shear zones or along terrane boundaries have been reported from different parts of the world and of diverse age (Hutton, 1982, 1988a, 1988b, 1996, 1997; Crawford et al., 1987; Guinerberteau et al., 1987; Karlstrom, 1989; McCaffrey, 1989, 1992; Reavy, 1989; Hutton et al., 1990; D'Lemos et al., 1992; Hutton and Reavy, 1992; Ingram and Hutton, 1994; Tikoff and Blanquat, 1997; Klepeis and Crawford, 1999; Nummer et al., 2007; Zibra et al., 2014). Several tectonic models on the emplacement of granites have been proposed by different workers for different tectonic settings (Figures 1.1-1.4). The mechanism of granite emplacement in these shear zones or terrane boundaries largely depends on the interaction between the ambient tectonic forces and the natural magma buoyancy (Hutton, 1988a). Thus, the emplacement

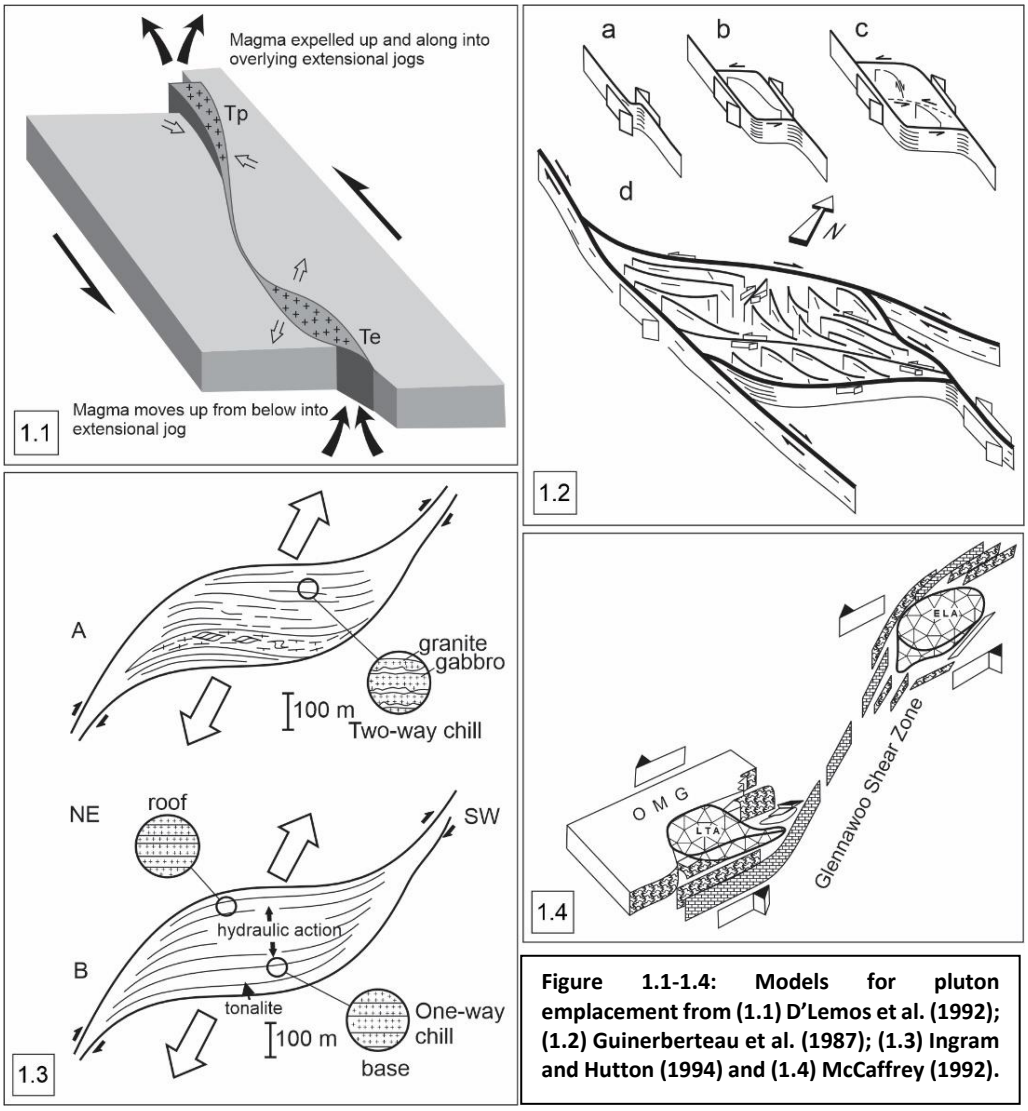

Figure 1.1-1.4: Models for pluton emplacement from (1.1) D'Lemos et al. (1992); (1.2) Guinerberteau et al. (1987); (1.3) Ingram and Hutton (1994) and (1.4) McCaffrey (1992).

mechanism varied widely depending on the tectonic set up and the evolution of the particular area. It is therefore crucial to understand the spatial and temporal patterns of the fabrics within granites as well as their relationship with the structure of the country rocks in order to assess the process of granite emplacement in a region (Guineberteau et al., 1987; Hutton, 1988a, b, 1996; Reavy, 1989; Hutton and Reavy, 1992; D'Lemos et al., 1992; McCaffrey, 1992; Merle and Vendeville, 1995; Pitcher, 1997; Brown and Solar, 1998; Cruden, 1998; Saint-Blanquat et al., 1998, 2001, 2006, 2011; Vigneresse et al., 1999; Petford et al., 2000; Barraud et al., 2001).

In northwestern India, the Phulad Shear Zone (PSZ) demarcates the boundary between South Delhi Fold Belt (SDFB) to the east and Marwar craton to the west (Figure 1.5)

(Heron, 1953; Sychanthavong and Desai, 1977; Gupta et al., 1980; Sen, 1980; Sinha-Roy, 1988; Sugden et al., 1990; Volpe and Macdougall, 1990; Sinha-Roy et al., 1993, 1995, 1998; Golani et al., 1998; Tewari et al., 1998; Ghosh et al., 1999, 2003; Roy and Jakhar, 2002; Sengupta and Ghosh, 2004, 2007; Chatterjee et al., 2017). The Phulad Shear Zone is described as a terrane boundary shear zone (Sinha-Roy, 1988) along which the Greater India landmass accreted with the Marwar craton at ~810 Ma (Chatterjee et al., 2017). The Phulad Shear Zone is characterized by NE-SW trend and steep easterly dipping mylonitic foliation that runs for several kilometers (Heron, 1953; Sychanthavong and Desai, 1977; Gupta et al., 1980; Sen, 1980; Sinha-Roy, 1988; Sinha-Roy et al., 1993; Golani et al., 1998; Sinha-Roy et al., 1998; Ghosh et al., 1999, 2003; Roy and Jakhar, 2002; Sengupta and Ghosh, 2004, 2007). Structural studies of the Phulad Shear Zone indicate that deformation in the shear zone is transpressional with a reverse sense of movement (Ghosh et al., 1999, 2003; Sengupta and Ghosh, 2004, 2007). The rocks of the Marwar craton belong to the footwall unit, and the rocks of the South Delhi Fold Belt belong to the hangingwall unit. There are several reports of granitoid intrusives of ~800 Ma close to this PSZ (Van Lente et al., 2009; Dharma Rao et al., 2013; Zhao et al., 2018; Singh et al., 2021) (Figure 1.5). However, the structural relationship of these granitoid rocks with PSZ and the differentiation of these granitoid bodies remained unclear. In this present work ~200 km long contact between the Marwar cratonic rocks and the rocks of SDFB has been mapped. New field relations, structural elements, microstructural features, geochemistry, and radiometric age data are discussed, and the implications of the data for the emplacement process of granitic pluton in relation to the Phulad Shear Zone deformation and tectonics of northwestern India are delivered in the present study.

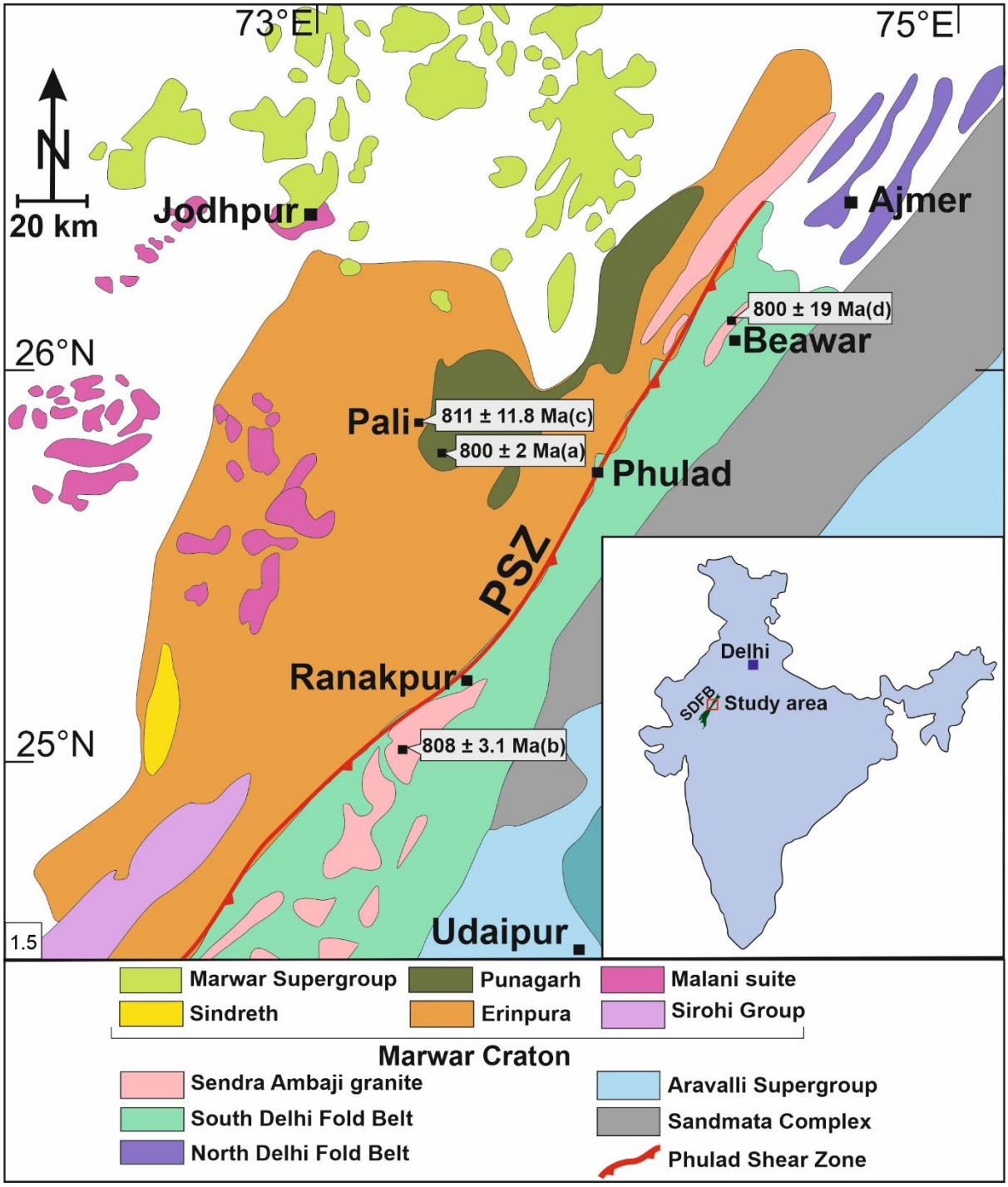

Figure 1.5: Geological map depicting the different crustal domains in northwestern India (modified after Heron, 1953; Gupta et al., 1980; Roy and Jakhar, 2002; and Chatterjee et al., 2017). Inset shows the position of Delhi and the study area on the map of India. Available concordant zircon data are shown in boxes. Data sources: (a) Van Lente et al. (2009); (b) Dharma Rao et al. (2013); (c) Zhao et al. (2018); (d) Singh et al. (2021).

1.2 Geological Background:

The Delhi Fold Belt (DFB), is a 700 km long mountain chain with NE-SW orientation. It consists of extensively folded and poly-metamorphosed rocks from the Proterozoic age. Gupta et al. (1980) suggested distinct depositional environments north and south of Ajmer, leading to the division of DFB into the older North Delhi Fold Belt (NDFB) and the younger South Delhi Fold Belt (SDFB). The western portion of the Delhi Fold Belt, primarily mapped by Coulson (1933), Heron (1953), Gupta et al. (1980), and Sinha-Roy et al. (1998), features the 'Erinpura granite,' sometimes described as an unclassified granite. Erinpura granite is characterized by its white to greyish color and porphyritic nature. The rocks of the South Delhi Fold Belt, including the Erinpura granite, have been dated to approximately 850 ± 50 Ma based on Rb–Sr isotopic data. The Erinpura granite or gneisses, characterized by porphyritic nature, extend over 325 km in length and 3 to 15 km in width within the western part of SDFB. The granitic emplacement of Erinpura is divided into two magmatic episodes according to Coulson (1933), while others consider it as a single larger magmatic event occurring between 860-830 Ma (Crawford, 1970; Bhushan, 1995; Deb et al., 2001; Van Lente et al., 2009; Just et al., 2011; Zhao et al., 2018; Singh et al., 2021; De Wall et al., 2022). Geochemically, it falls into the granite to granodiorite range and displays calc-alkaline composition. Enriched in SiO_2, MgO, FeO_t, CaO, and metaluminous to peraluminous (AICNK ratio > 1.15), Erinpura granite belongs to the 'I'-type collisional granite and collision granite (COLG) categories as classified by Bhushan (1995).

The NE-SW trending Phulad Shear Zone marks the western boundary of the mid-Proterozoic South Delhi Fold Belt within the Indian craton. The PSZ is recognized on the basis of extensive development of mylonites (Golani et al., 1998; Ghosh et al., 1999) in a transpressional regime of ductile shear zone (Ghosh et al., 1999, 2003; Sengupta and Ghosh, 2004, 2007), where the strain is mainly concentrated along bands of interlayered calcareous and quartzofeldspathic

mylonites. The age of this shear zone was considered as Grenvillian, based on the emplacement age of granitic rocks from the area (Deb et al., 2001; Singh et al., 2010, Dharma Rao et al., 2013; Meert et al., 2013). Recent work of Chatterjee et al. (2017), based on textural controlled in situ monazite age dating, showed that the reverse shearing in PSZ occurred during 810-820 Ma.

1.3 Definition of the Problem:

In the northwestern Indian shield, the South Delhi Fold Belt (SDFB) is a NE-SW trending long mountain chain consisting of multiple folded and poly-metamorphosed rocks of proterozoic age. The Phulad Shear Zone (PSZ) is a transpressive shear zone with a top-to-the-NNW reverse sense of movement. There are also several reports of intrusive bodies, particularly porphyritic granite of ~800 Ma close to this PSZ (Van Lente et al., 2009; Dharma Rao et al., 2013; Zhao et al., 2018; Singh et al., 2021), but there is a dearth of information about the emplacement process of the granitic rocks in relation to the shear zone deformation. Therefore, detailed field structures of the granites and their relationship with the development of PSZ are crucial to understanding the process of granite emplacement in this region and the tectonics of the area.

The present work aims to reconstruct the detailed field relations, mesoscopic and microscopic structures of the ~800 Ma granites and their relationship with the PSZ; its geochemistry and geochronology to understand the process of granite emplacement and discuss the implications of the outcomes for the tectonics of the region.

1.4 Objective of the Present Work:

To fulfill the above objective the research work will be carried out on the following aspects.

1. Study of mesoscopic structural elements to understand the deformation pattern of the Phulad Shear Zone.
2. Detailed structural mapping of some critical areas to reconstruct the field structure of granitic rocks in relation to the tectonic deformation of the Shear Zone structures.
3. The study of fabric and microstructure of the granites with special emphasis on understanding intracrystalline deformation and static recovery. Grain-size analysis.
4. Geochemical study (major, trace and REE patterns) of the granites.
5. Geochronological study of the granite using conventional zircon dating and

   EPMA monazite age dating technique.
6. Integrating all the above mentioned data to characterize the structural development and evolution of the rocks across the PSZ.

1.5 Location, Climate, and Physiography:

1.5.1 Location and accessibility:

Phulad is a village located in Pali district in Rajasthan state of India. The present study is carried out along and across the PSZ. The area falls in Survey of India toposheet no. 45D/13, 45G/4, 45G/8, 45G/10, 45G/11, 45G/12, 45G/13, 45G/14, 45G/15, 45H/1 sequentially from north to south of the Rajasthan and bounded by latitudes 24°45'N to 26°N and longitudes 72°45'E to 74°E. The field area is well connected by the Jaipur Railway Junction in the northern part and Ajmer Railway Junction-Udaipur section on the Western Railway, which passes through the southern part of the area. Marwar junction and Beawar Railway station are located in this section. The whole field area is accessible by various roads from Sojat-Sirohi-Mount Abu Road, such as National Highway no: NH-62 and NH-27, State Highway, and some

of the village roads. The area forms part of the main NE-SW trending Aravalli Mountains and the geologically western part of SDFB.

1.5.2 Climate:

The study area comes under a tropical, warm climate zone and moreover it is in close proximity to the Thar Desert in North-West Rajasthan. As a result, the area experiences a wide diurnal fluctuation in temperature. During daytime, the temperature goes up to 50 ˚C during summer. Even during winter, the temperature remains nearly 30 ˚C during daytime but at night it may fall to 10 ˚C. The average annual rainfall is very low, about 5-10 cm. Generally, the best time for fieldwork is September to February. However, in recent time (last five years), the climate of Rajasthan has been changed. The average temperature gap between summer and winter has been minimized because of the massive increase in the plantation.

1.5.3 Physiography of the study area:

The area can be grouped into three domains namely (i) the western sandy plains, (ii) the hill ranges and (iii) the eastern plains. These divisions are based on the existing relief-features and provide a basis for the study of the geomorphic evolution of the terrane, which has been sculptured through a number of erosional cycles represented by various surfaces. The region is characterized by mature topography with more or less flat-topped mountain ridges, escarpments, inselberg surfaces, river valleys, intermontane valleys and vast stretches of plains. The whole area is undulating in nature and dominated by hilly terrane.

Chapter 2

Field Relations and Deformation Patterns

2.1 Introduction:

The Phulad Shear Zone (PSZ) demarcates the boundary between the Marwar craton to the west and the South Delhi Fold Belt (SDFB) to the east. The shear zone is northeast-southwest trending that runs for several kilometers and has a width of ~30 meters (Ghosh et al., 1999). The PSZ is described as a terrane boundary shear zone (Sinha-Roy, 1988) that developed during ~810Ma (Chatterjee et al., 2017). In this work, PSZ, i.e., the contact between the Marwar cratonic rocks and the rocks of SDFB has been mapped for ~200 km. The new map shows that the porphyritic Phulad granite (Gangopadhyay and Lahiri, 1986) occurs parallel to the PSZ and intrudes rocks of the Marwar craton and SDFB. In this chapter, a detailed structural study of the PSZ and the Phulad granite has been included.

2.2 Phulad Shear Zone:

The PSZ is identified by the strong development of mylonitic foliation in the intercalated calcareous quartzo-feldspathic layer and the mylonitic foliation dips steeply towards the southeast with a prominent set of steep oblique striping (Figures 2.1, 2.2) and stretching

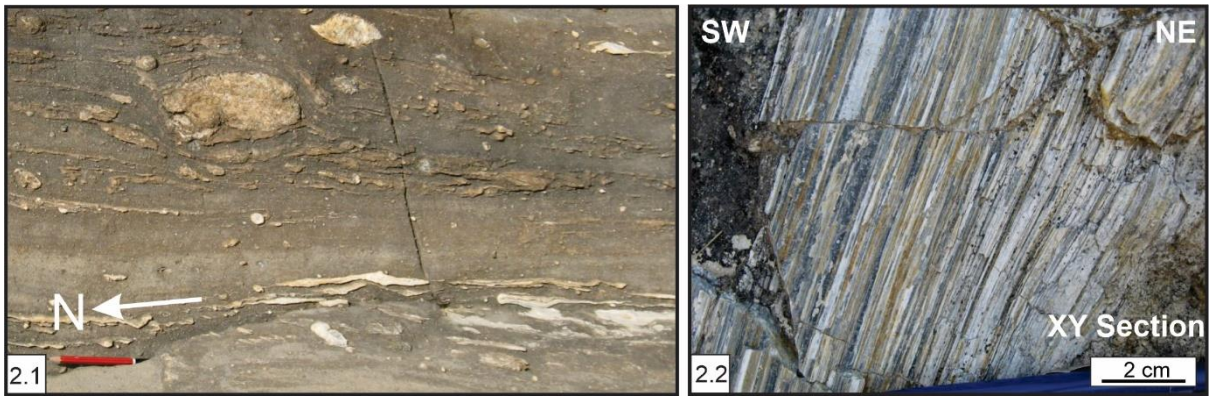

Figure 2.1-2.2: Field photographs showing (2.1) mylonitic foliation in intercalated calcareous quartzo-feldspathic layers, (2.2) striping lineation on foliation plane (XY section). The length of the pencil in (2.1) is 10 cm.

lineations (Figure 2.3). Stereoplot showing both the foliation and steep plunging lineation of PSZ (Figure 2.4). Stretching lineation is defined by stretched quartz grains and occurs parallel

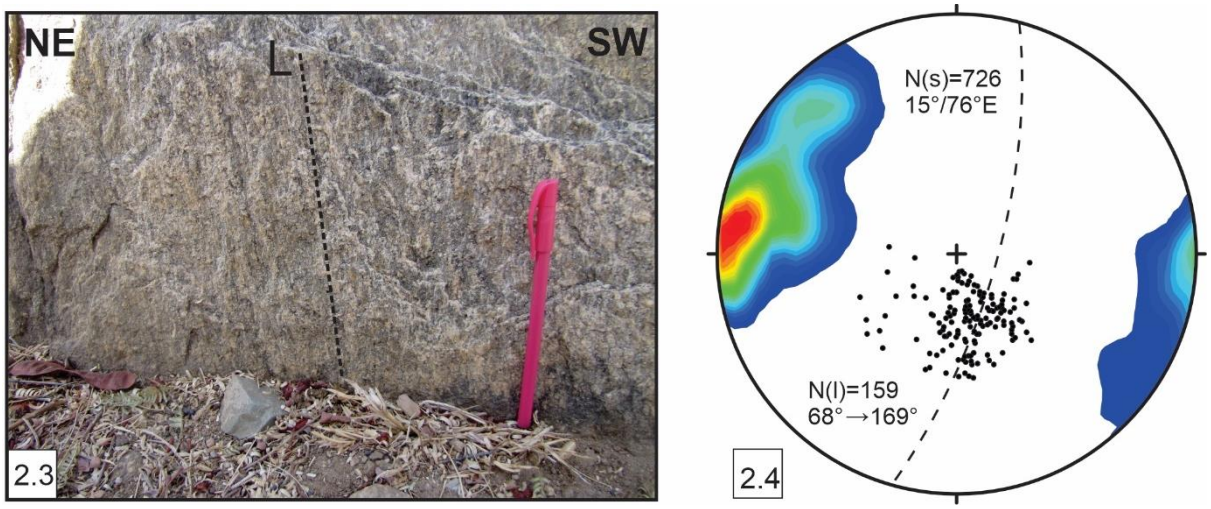

Figure 2.3-2.4: Field photograph showing (2.3) stretching lineation on foliation plane (XY section) and (2.4) stereogram shows mylonitic foliation, mean principal orientation is 15°/76°E and steep plunging lineation of the PSZ. The length of the pen in (2.3) is 14 cm. N (s) = number of foliation and N (l) = number of lineation data for the stereogram.

to this striping lineation (Sengupta and Ghosh, 2007). Maximum rotation of structural elements is observed in the XZ section (sub-vertical section perpendicular to foliation and parallel to lineation). Hence the vorticity axis is perpendicular to this XZ plane. Asymmetric mesoscopic structures in the XZ section suggest a top-to-the-NNW reverse sense of movement (Figure 2.5). This movement direction in PSZ is parallel to the stretching lineation and perpendicular to the vorticity axis (Figure 2.6) (Sengupta and Ghosh, 2004, 2007; Chatterjee et al., 2017). Because of this oblique reverse slip movement in the shear zone, there is a component of sinistral slip movement on the sub-horizontal section (Figures 2.6, 2.7). In both XZ and YZ (section perpendicular to foliation and lineation) sections, the feldspar porphyroclasts in quartzo-feldspathic mylonites show evidence of stretching. However, the stretching along the x-axis is considerably large compared to the y-axis. This suggests a

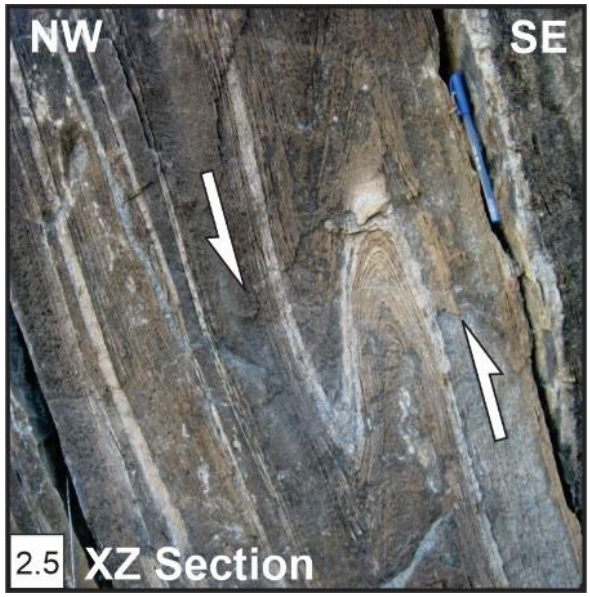

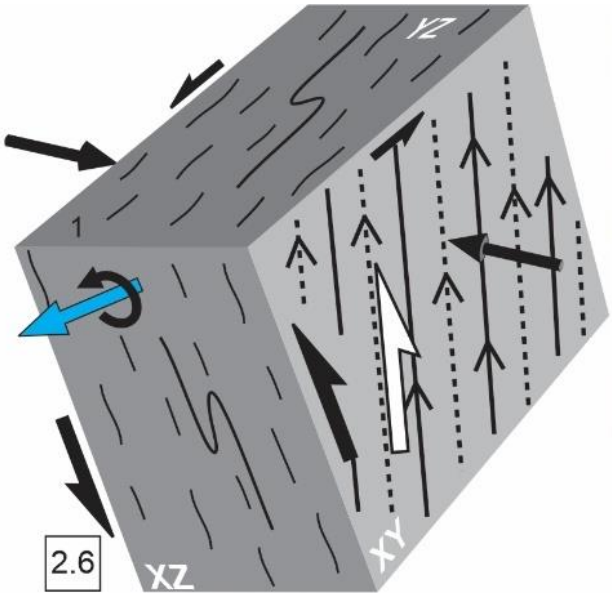

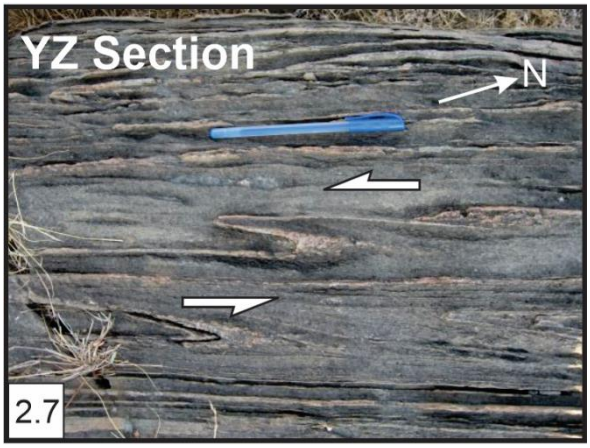

Figure 2.5-2.7: Field photograph showing (2.5) asymmetric fold showing top-to-the-NNW reverse sense of movement on XZ section. (2.6) Schematic diagram showing the formation of sinistral slip movement on the horizontal section because of the oblique reverse movement on the shear plane, white arrow shows the direction of movement parallel to the stretching and striping lineation, blue arrow shows the vorticity axis, field photograph showing (2.7) the sinistral slip movement on horizontal section (YZ section). The length of the pen in (2.5) and (2.7) is 14 cm.

general flattening type of deformation (X>Y>1>Z) across the shear zone (Sengupta and Ghosh, 2004; Sengupta and Chatterjee, 2016). Mapping of PSZ along its strike length of about 200 km reveals that at some places the orientation of the shear zone deviates from its regional NE-SW trend. At regular intervals, the shear zone shows small bends of N-S orientations (Figure 2.8). The length of this N-S orientation of PSZ in map scale varies from 2 to 4 km. This situation is also observed in a small scale. For example, meter scale N-S bends occur within the NE-SW segments of PSZ. This N-S bend occurs at all scales, i.e., from kilometers to centimeters, where

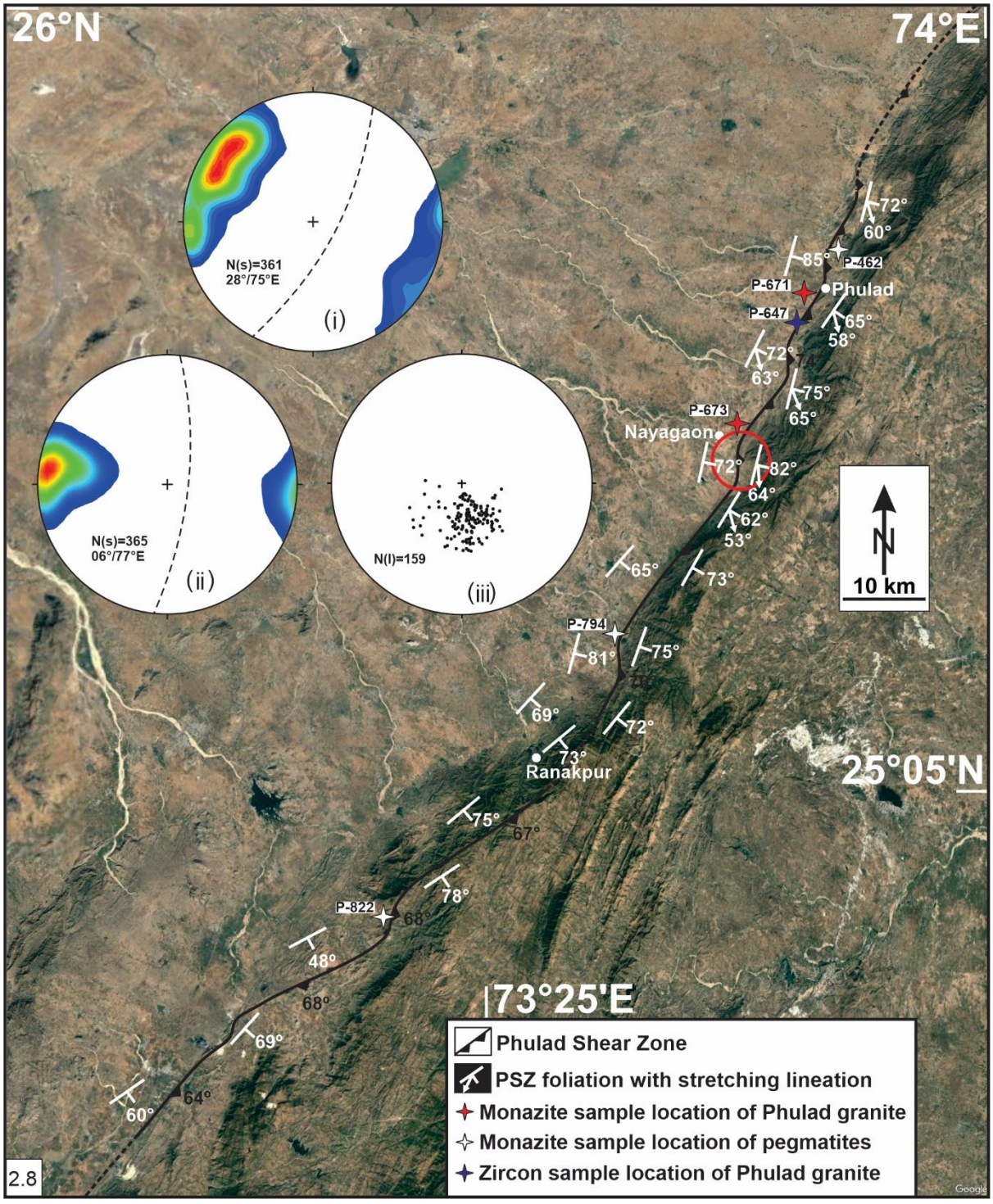

Figure 2.8: Satellite image of Google Earth showing the disposition and orientation of PSZ in the studied area. Stereograms show structural fabrics collected from (i) the regional NE-SW trend and (ii) small bends of N-S trend. (i) Mylonitic foliation, mean principal orientation is 28°/75°E. (ii) Mylonitic foliation, mean principal orientation is 06°/77°E. (iii) Steep oblique stretching lineation (mean orientation 68°→169°). N (s) = number of foliation and N (I) = number of lineation. Red circle shows one of the NS bends of PSZ.

the same patterns occur repeatedly at different scales and sizes, i.e., the repetition is fractal in nature. Data were plotted separately for mylonitic foliations that were collected from the regional NE-SW and N-S orientation of PSZ (Figure 2.8). Stereoplots show the presence of N-S data in the NE-SW segment of the PSZ, and the absence of NE-SW foliations in the N-S segments of the PSZ. The lineation data show steep plunging towards SSE (mean orientation 68˚→169˚) for both NE-SW and N-S orientation of PSZ (Figure 2.8).

The hangingwall portion of PSZ belongs to SDFB and contains a variety of rock types, viz.; mica schists interlayered with metamarls, meta-gabbro, amphibolites and deformed granites. Two phases of deformations have been reported from SDFB (Gupta et al; 1995, Roy and Sharma, 1999; Roy and Jakhar, 2002; Chatterjee et al., 2017). Close to the PSZ (~2 km), all the rocks show strong development of foliation and steep oblique stretching lineation, similar to that of mylonitic foliation and lineation of PSZ.

The footwall portion of PSZ belongs to the Marwar craton that contains variably deformed granitoids rocks. The deformation in these granitoids, neighbouring the PSZ, varies from weakly foliated through gneissose to mylonite and ultramylonite (Roy Choudhury et al., 2016). The mean orientation of the foliation in these granitoids broadly overlaps with that of the mylonites of PSZ. In strongly deformed granitoid, the rock shows prominent development of gentle plunging stretching lineation in the footwall rocks. However, this stretching lineation shows a steep plunge in the domains close to PSZ (<1 km). Spatially there is a sharp change in the plunge of the lineation from gentle to steep in the footwall rocks.

2.3 Phulad Granite:

The Phulad granite is grey coloured and porphyritic in nature, with feldspar phenocrysts in a matrix of quartz, feldspar, and mica. This granite is present all along the PSZ and in the wall rocks. The granite shows interdigited contacts with the host rocks of PSZ, SDFB and Marwar craton (Figures 2.9-2.11). The Phulad granite and its country rocks show prominent foliation.

Figure 2.9: Field photograph showing the contact relation of Phulad granite with SDFB rocks.

The foliation within the Phulad granite is secant to the pluton boundaries and is in continuity with the regional foliation (Figures 2.10-2.11). The width of Phulad granite across PSZ is

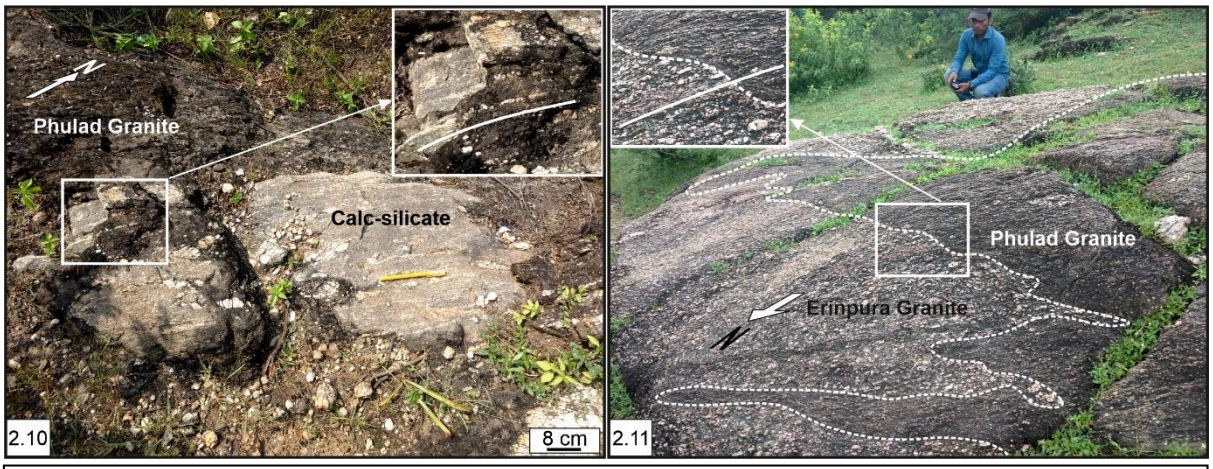

Figure 2.10-2.11: Field photographs showing the contact relation of Phulad granite with (2.10) shear zone rocks, and (2.11) Erinpura granite of Marwar craton. Zoomed portions in (2.10) and (2.11) show the continuation of Phulad granite foliation with the regional foliation of host rocks.

variable with a maximum of ~9 km. Lithological mapping of Phulad granite depicts wider width in the N-S orientation of PSZ compared to the regional NE-SW trend. This Phulad granite was mapped along with the PSZ near about ~200 km (Figure 2.12). A detailed geological map of

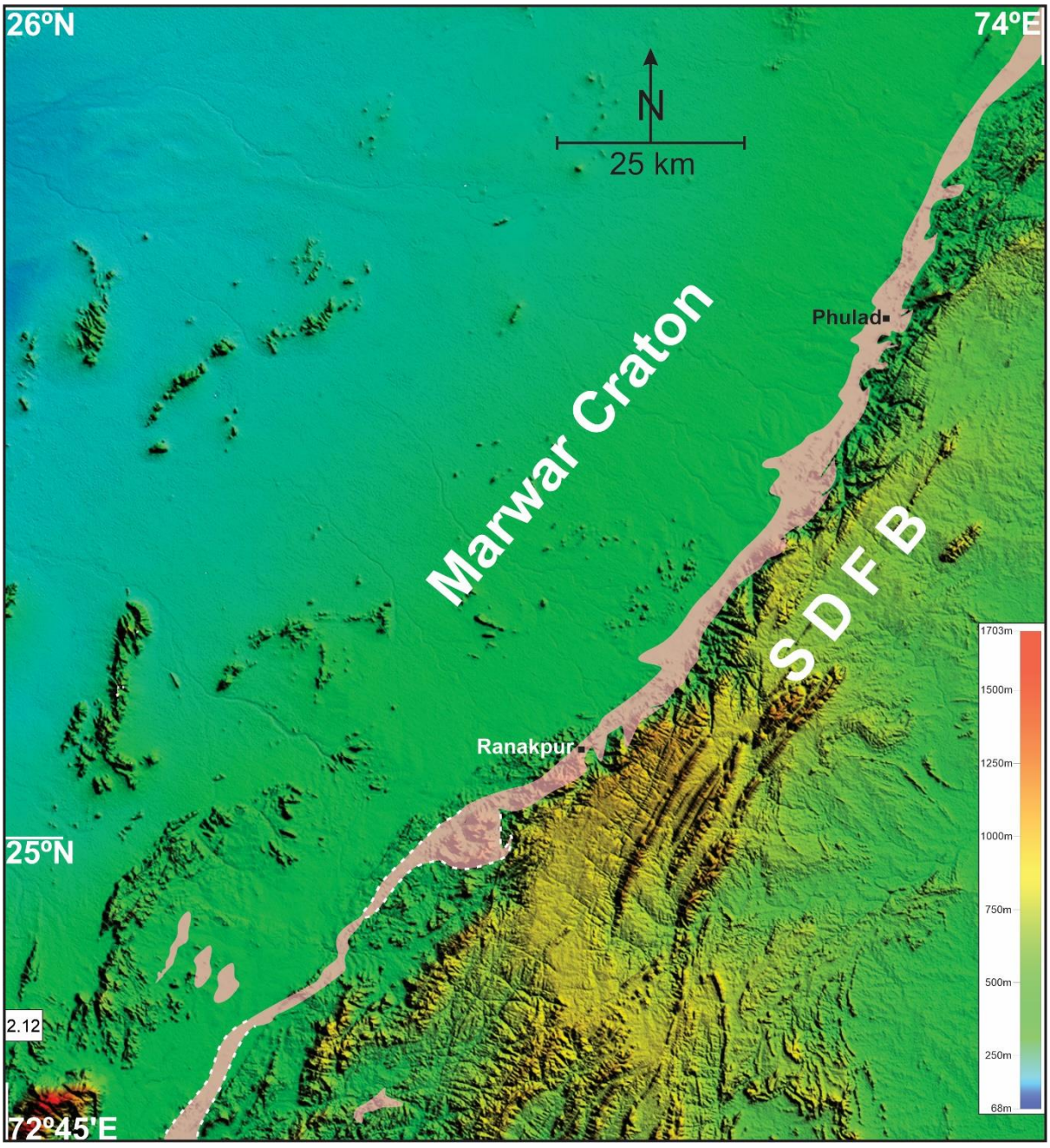

Figure 2.12: Digital Elevation Model (DEM) map with the outline of Phulad granite along the contact of Marwar craton and SDFB. Granite boundaries marked with white dotted line are inaccessible areas. DEM is prepared from the SRTM data of USGS Earth explorer.

the Phulad granite body was done in a portion of the shear zone (Figures 2.13-2.14). The map depicts that the granite body is continuous in the N-S orientation of PSZ. In the regional NE-

SW orientation of PSZ, the granite boundary is composed of many coalesced granite sheets striking parallel to the shear zone. Occurrences of pegmatite body are ubiquitously associated with Phulad granite in N-S orientation, whereas in the regional NE-SW segment of PSZ, there is rare/no presence of any pegmatite body.

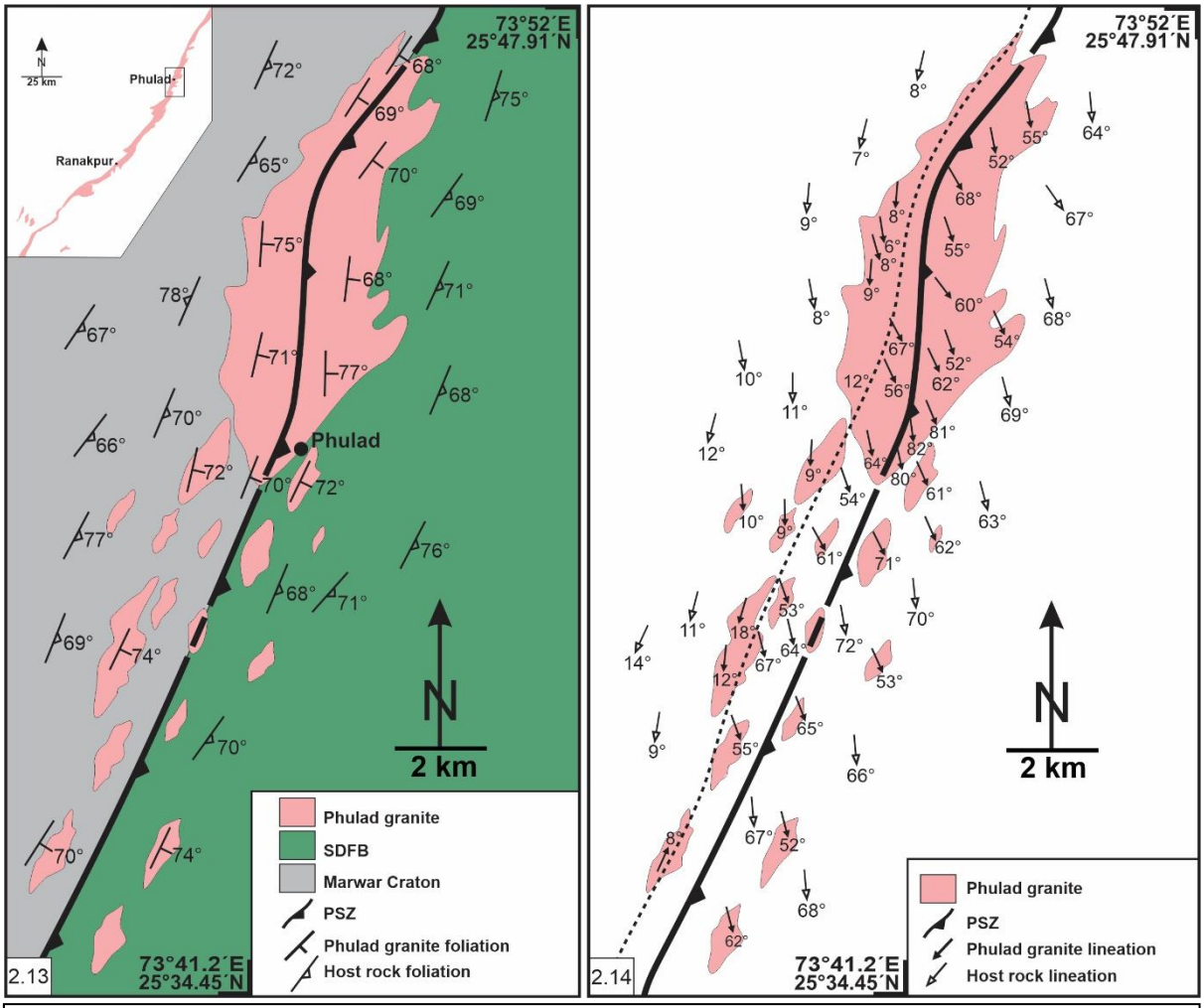

Figure 2.13-2.14: Detailed lithological map of Phulad granite with (2.13) foliation and (2.14) lineation. Inset in (2.13) shows the position of detailed map. Black dashed line in (2.14) separates the steep plunging lineation to the east and gentle plunging lineation to the west.

At mesoscopic scale, the Phulad granite shows an alignment of euhedral feldspar phenocrysts with simple twin interfaces parallel to the direction of elongation on the horizontal section (YZ section) (Figure 2.15). Feldspar phenocrysts are also prominent on sub-vertical section (XZ section) (Figure 2.16). The granite also shows an alignment of elongated microgranitoid enclaves both on horizontal (YZ section) and vertical (XZ section) sections

(Figures 2.17-2.18). The orientation and length of the long and short axis were measured for

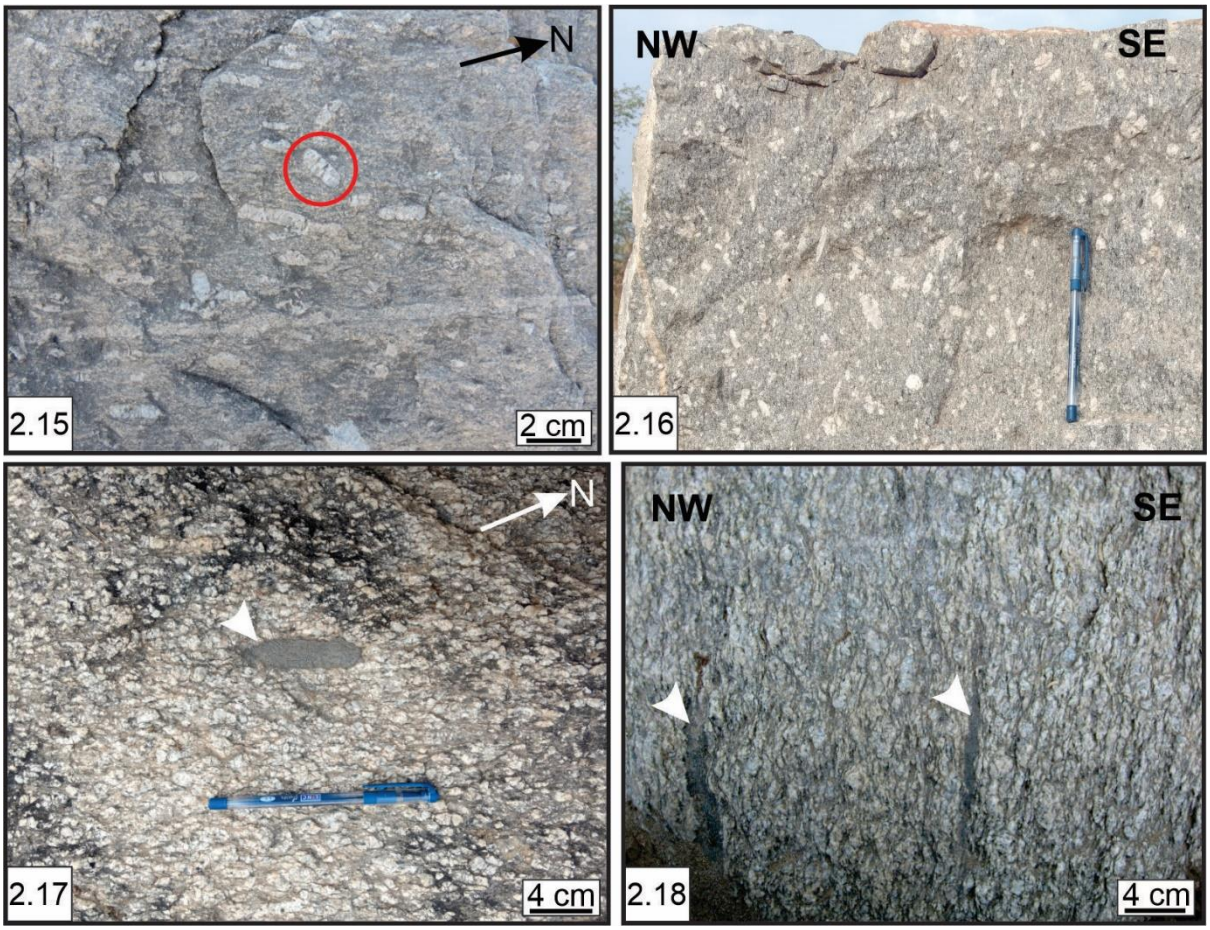

Figure 2.15-2.18: Field photographs showing (2.15) preferred alignment of euhedral feldspar phenocrysts with simple twin interfaces parallel to the direction of elongation (marked by red circle) on horizontal section. Feldspar phenocrysts are also shown on vertical section (2.16). Microgranitoid enclave (shown by white arrow head) parallel to foliation on (2.17) horizontal and (2.18) vertical section. The length of the pen in (2.16) and (2.17) is 14 cm.

feldspar phenocrysts of the granite on the sub-horizontal section (YZ). The length of the long and short axis was measured for feldspar phenocrysts on the sub-vertical section (XZ). Data were taken separately for both euhedral and deformed varieties of feldspar phenocrysts (Figures 2.19-2.24). The dominant orientation of long axes of both euhedral and deformed variety feldspar phenocrysts shows strong preferred orientation in the NNE-SSW direction with rare or no orientation in the ESE-WNW direction (Figures 2.19, 2.22). Microgranitoid enclaves are generally less frequent. Data were taken for microgranitoid enclaves both from euhedral and deformed feldspar phenocryst variety of granite in a similar way as mentioned above (Figures 2.25-2.30). The orientation of the microgranitoid enclaves is dominantly in

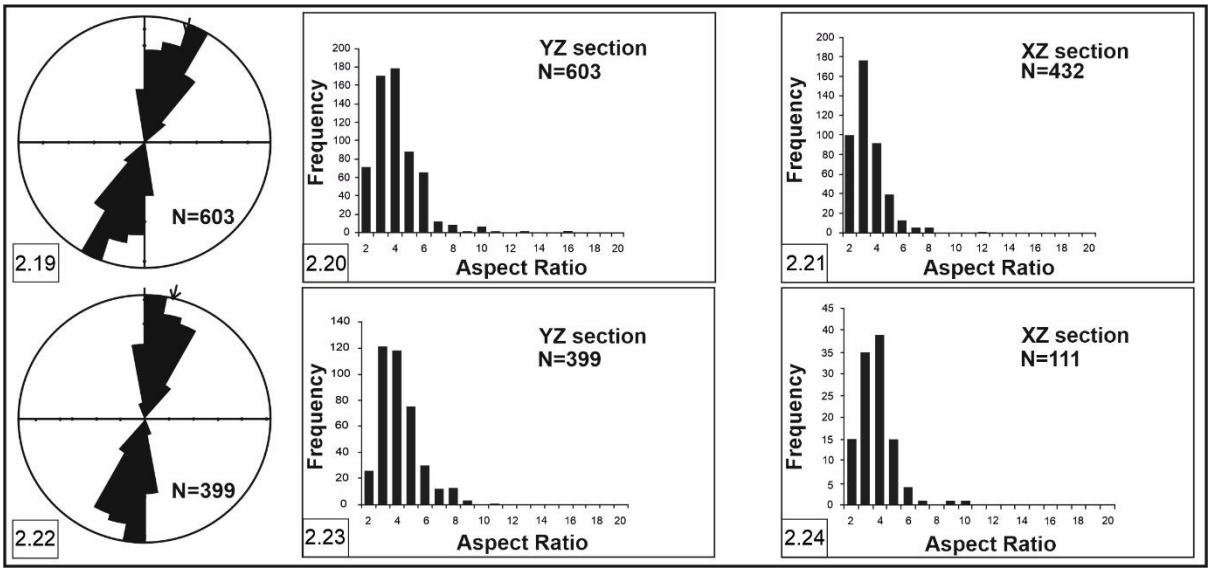

Figure 2.19-2.24: Rose diagrams showing the orientation of (2.19) euhedral and (2.22) deformed variety of feldspar phenocrysts. Histogram plots showing aspect ratio of euhedral feldspar phenocrysts on (2.20) sub-horizontal section and (2.21) sub-vertical section. Histogram plots showing aspect ratio of deformed feldspar phenocrysts on (2.23) sub-horizontal section and (2.24) sub-vertical section. N = number of data.

NNE-SSW directions with rare or no orientation in ESE-WNW directions (Figures 2.25, 2.28).

The aligned euhedral feldspar phenocrysts, deformed feldspar phenocrysts and

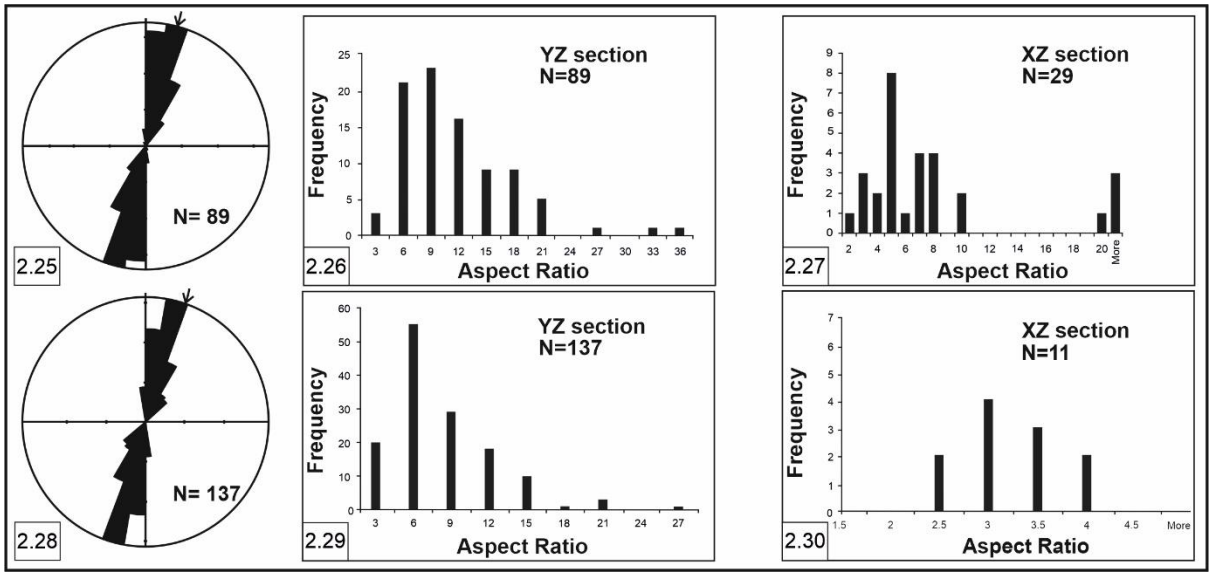

Figure 2.25-2.30: Rose diagrams showing the orientation of microgranitoid enclaves in (2.25) least deformed and (2.28) deformed variety of Phulad granite. Histogram plots showing aspect ratio of microgranitoid enclaves on (2.26) sub-horizontal section, (2.27) sub-vertical section in least deformed variety and (2.29) sub-horizontal section and (2.30) sub-vertical section in deformed variety of Phulad granite. N = number of data.

microgranitoid enclaves occur parallel to each other. The Phulad granite is variably deformed with prominent development of foliation parallel to the alignment of phenocrysts and microgranitoid enclaves. In the least deformed variety, the granites preserve the euhedral

feldspar with weak development of foliation. In a more deformed variety, the granite varies from strongly deformed to mylonite/ ultramylonite (Figures 2.31, 2.32). In all these varieties,

Figure 2.31-2.32: Field photographs showing (2.31) deformed feldspar phenocryst with development of tail and (2.32) ultramylonite variety of Phulad granite. The length of the pen in (2.31) and (2.32) is 14 cm.

the orientation of the solid-state foliation varies from N-S to NE-SW. Data were plotted separately for the foliations that were collected from the regional NE-SW shear zone and from small bends of N-S orientation of PSZ (Figures 2.33, 2.34). In strongly deformed variety, the

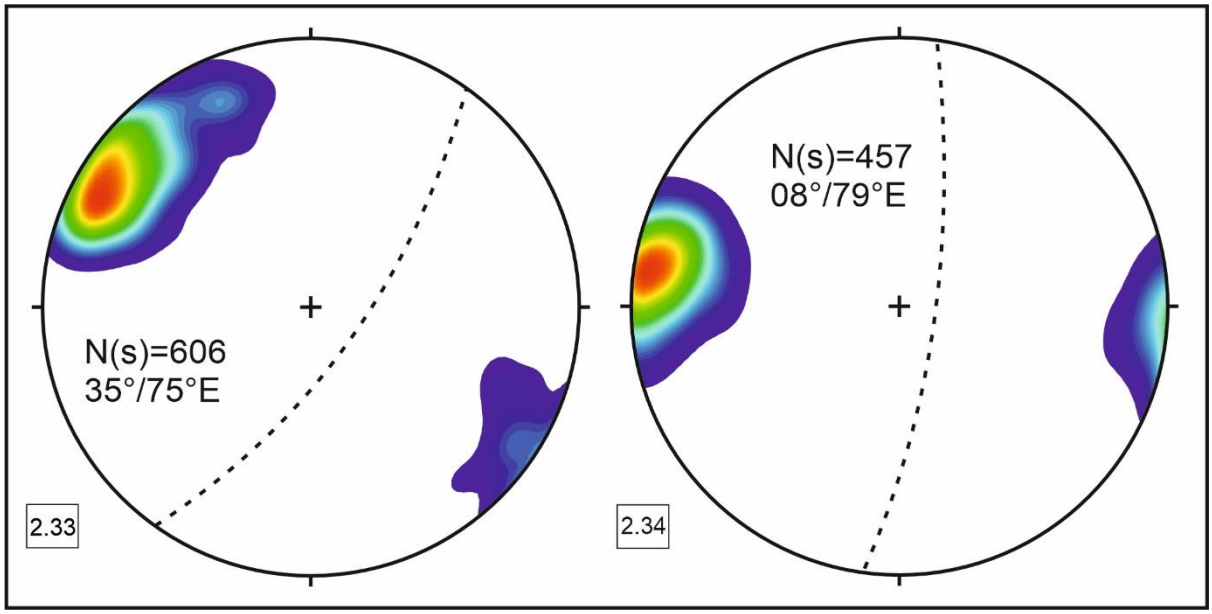

Figure 2.33-2.34: Stereograms showing analysis of structural fabrics of Phulad granite collected from (2.33) the regional NE-SW trend (2.34) small bends of N-S trend, (2.33), (2.34) Stereograms shows mylonitic foliation of Phulad granite, mean principal orientation is 35°/75°E and 08°/79°E respectively. N(s) = number of foliation data for the stereograms.

granite shows prominent development of stretching lineations, both gentle and steep plunging, defined by stretched quartz and feldspar grains (Figures 2.35, 2.36). Stereographic plots of lineation data show two-point maxima with mean orientations of 03°→193° and 65°→ 170° (Figures 2.37, 2.38). This variation in the plunge of the lineation varies spatially

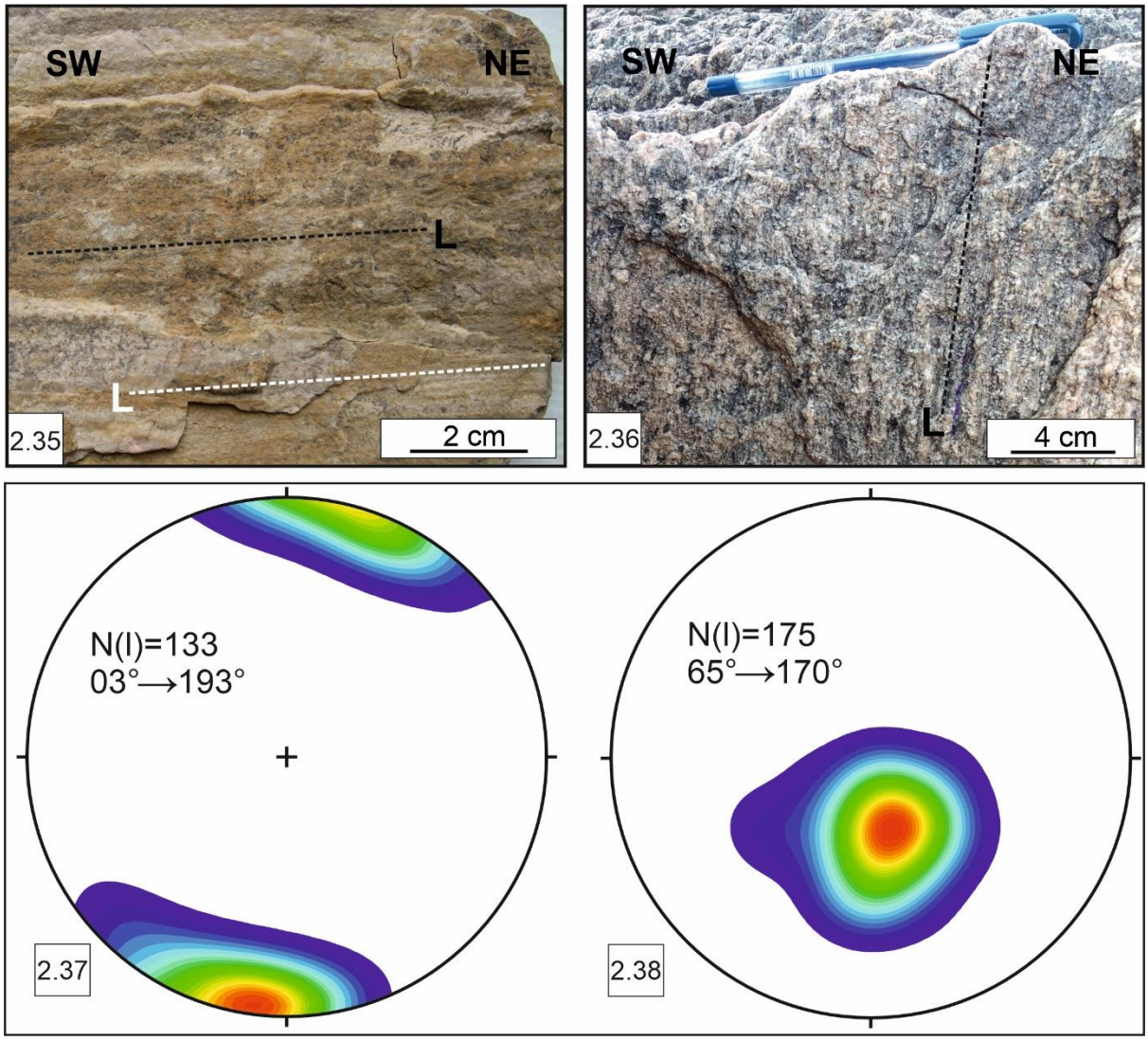

Figure 2.35-2.38: Field photographs showing (2.35) gentle plunging stretching lineation and (2.36) steep oblique stretching lineation on Phulad granite foliation. Stereograms showing (2.37) gentle and (2.38) steep plunging stretching lineation of Phulad granite respectively. The length of the pen in (2.36) is 14 cm. N (l) = number of lineation data for the stereograms.

(Figure 2.14). The Phulad granite shows steep plunging lineation in the shear zone, in the hangingwall portions and in the domain of the footwall that is close to the PSZ (Figure 2.14). The stretching lineation is gently plunging in the footwall that is distant from the PSZ. Matrix quartz grains were used to estimate the finite strain ellipse using the Fry method (Fry, 1979) and were plotted in the Flinn diagram (Flinn, 1962). The strain analysis plot shows a flattening type of deformation (Figure 2.39) in Phulad granite. Asymmetric tails of feldspar porphyro-clasts indicate a top-to- the-NNW reverse sense of movement (Figure 2.40).

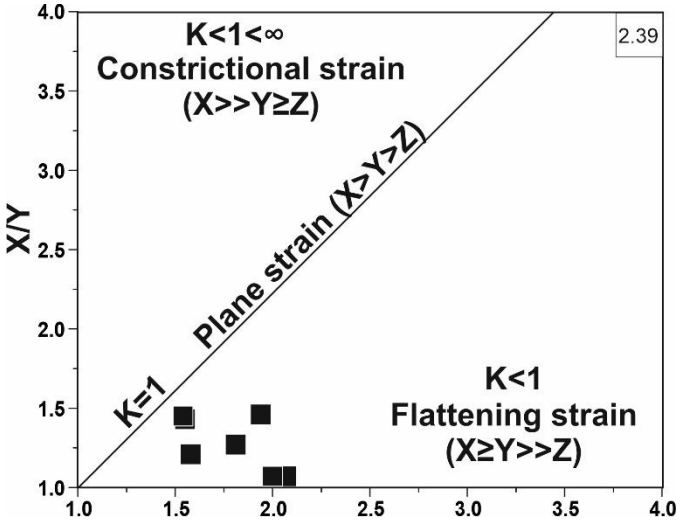

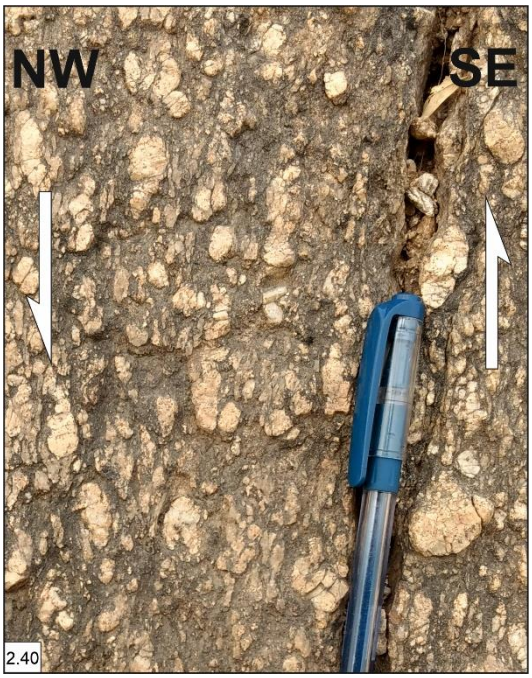

Figure 2.39-2.40: Flinn diagram (Flinn, 1962) shows a flattening type of deformation (2.39) in Phulad granite. Asymmetric tails of feldspar porphyroclasts indicate a top-to-the-NNW reverse sense of movement (2.40).

2.4 Kinematic Vorticity Analysis:

Analysis of kinematic vorticity is essential for the understanding of flow in ductile shear zones (McKenzie, 1979; Means et al., 1980; Ghosh, 1987; Weijermars, 1991; Simpson and De Paor, 1993; Robin and Cruden, 1994; Tikoff and Fossen, 1995; Xypolias and Koukouvelas, 2001; Forte and Bailey, 2007; Xypolias, 2009; Xypolias et al., 2010; Michels et al., 2015). There are several methods to obtain the kinematic vorticity number. Amongst them, Porphyroclast Hyperbolic Distribution (PHD) method is mainly used to calculate the kinematic vorticity of deformed rocks having porphyroclasts (Ghosh and Ramberg, 1976; Simpson and De Paor, 1993, 1997). Due to deformation the rigid ellipsoidal grains may rotate either forward with the sense of shear or backward which is counter to the shear sense. The plot of orientation and aspect ratio of differently oriented porphyroclasts in the polar coordinates gives the result of kinematic vorticity. The PHD method is used to estimate the kinematic vorticity number (W_n), measuring the acute angle (α) between the flow eigenvectors determined from the orientations of back-rotated σ (sigma) porphyroclasts. This PHD method is applied to

calculate the sectional kinematic vorticity number, W_n value in the deformed variety of Phulad granite (Figure 2.41). Calculations are done on mesoscopic scale as PHD method can be

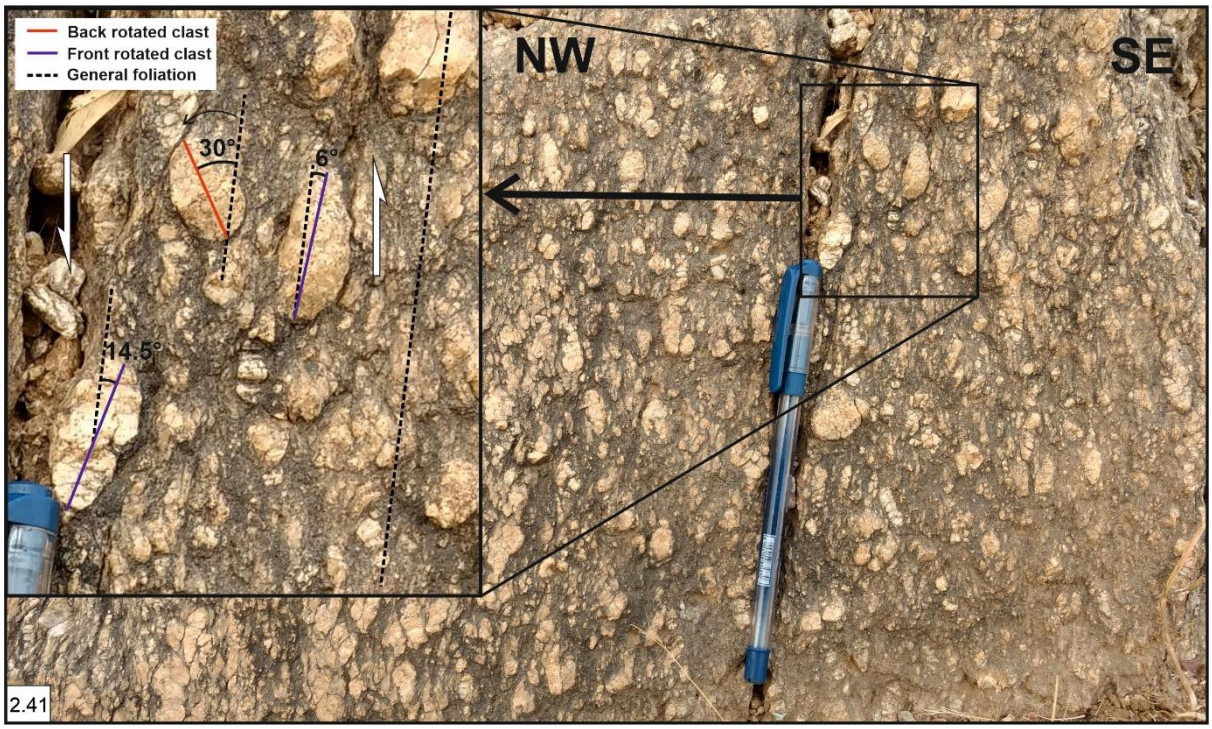

Figure 2.41: Field photograph showing back rotated and front rotated clasts along with general foliation in Phulad granite.

misleading on a microscopic scale (Sengupta and Chatterjee, 2016). W_n is calculated on the PHD net by plotting the aspect ratio (R=long/short axis) and angle ϕ (ϕ = angle between the long axis of the clast and trace of foliation on the XZ section). W_n values of deformed Phulad granite from the shear zone and hangingwall portions are calculated, and the respective values are W_n=0.91 and W_n=0.86 (Figures 2.42, 2.43). The W_n values of Phulad granite are calculated separately for steep and gentle plunging lineations from the footwall unit, and the values are W_n=0.82 and W_n=0.47, respectively (Figures 2.44, 2.45).

The sectional kinematic vorticity numbers are calculated for the country rocks of PSZ and its wall rocks using oblique grain shape foliation (Law et al., 1984, 1990; Lister and Snoke, 1984; Trullenque et al., 2006). The measured values show W_n = 0.90 to 0.96, W_n = 0.81 to 0.92 for PSZ and hangingwall rocks, respectively (Figure 2.46). The W_n values of footwall host rocks

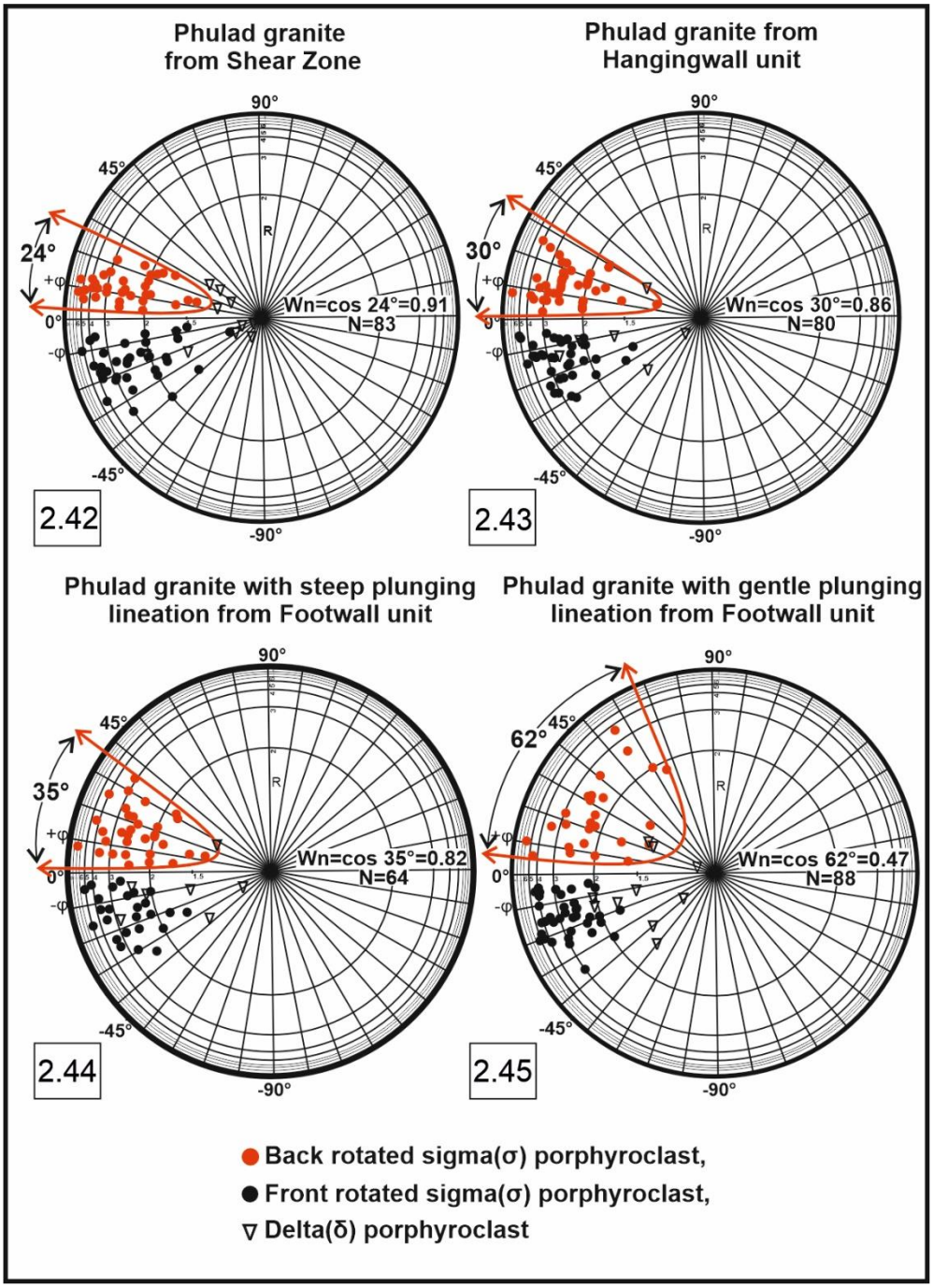

Figure 2.42-2.45: Hyperbolic stereonet plots of both front and back rotated porphyroclasts of Phulad granites from shear zone (2.42), hangingwall portions (2.43), footwall with steep plunging (2.44) and footwall with low plunging (2.45) respectively.

showing gentle plunging lineation and steep plunging lineation are W_n = 0.32 to 0.51 and W_n = 0.79 to 0.91, respectively (Figure 2.46).

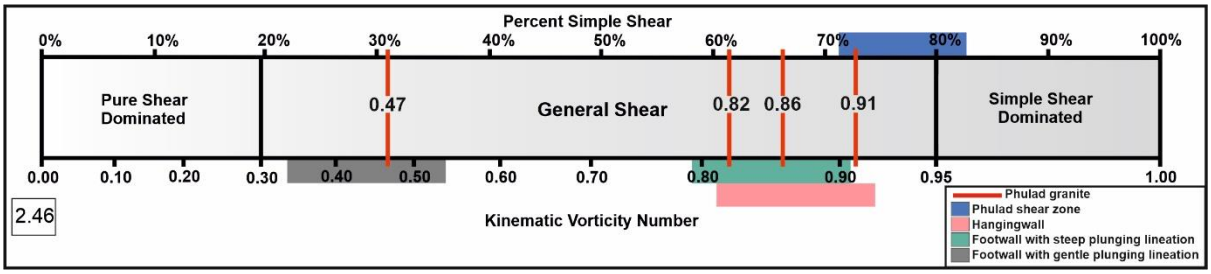

Figure 2.46: Range of measured W_n values of Phulad granite and the country rocks from shear zone, hanging wall, and footwall portions are shown in kinematic vorticity number and percent simple shear relation diagram (after Forte and Bailey, 2007).

2.5 Summary:

The PSZ has a regional NE-SW trend with small bends of N-S orientations at regular intervals. This shear zone is characterized by steep southeasterly dipping mylonitic foliation and steep oblique stretching lineation. The PSZ has been developed in a ductile transpression with a top-to-the-NNW reverse sense of movement. The Phulad granite intrudes the PSZ and its wall rocks and is variably deformed with well-developed solid-state fabric. The Phulad granite is variably deformed. In the strongly deformed variety, the granite shows strong NE-SW foliation development and prominent lineation development. The asymmetric structures in Phulad granite show a top-to-the-NNW reverse sense of movement. The detailed structural study demonstrates that the deformation in the PSZ and Phulad granite is the same, suggesting that they are broadly synchronous.

At the mesoscopic scale, the Phulad granite shows the preferred alignment of euhedral feldspar phenocrysts with simple twin interfaces parallel to the direction of elongation (Figure 2.15). To explain the rotation of these euhedral feldspar grains to a particular alignment, without interference with neighbouring minerals, enough melt must be present during deformation (Paterson et al., 1989). The elongated microgranitoid enclaves are aligned parallel to the direction of feldspar alignment (Figure 2.17). All these features suggest

evidence of magmatic flow (Paterson et al., 1989) and the foliation defined by these aligned euhedral feldspar phenocrysts and microgranitoid enclaves are considered to represent magmatic foliation. Parallel to this magmatic foliation, Phulad granite exhibits the development of solid-state foliation, indicating that they formed under the same deformation. This further explains that the deformation was there before the complete crystallization of the granite magma.

2.5.1 Relation of vorticity with stretching lineation in Phulad granite:

Both the Phulad granite and the associated host rocks show steep plunging stretching lineation in the shear zone, hangingwall, and a small portion of footwall that is close to the shear zone (Domain A in Figure 2.47). In this domain, the stretching lineation is perpendicular

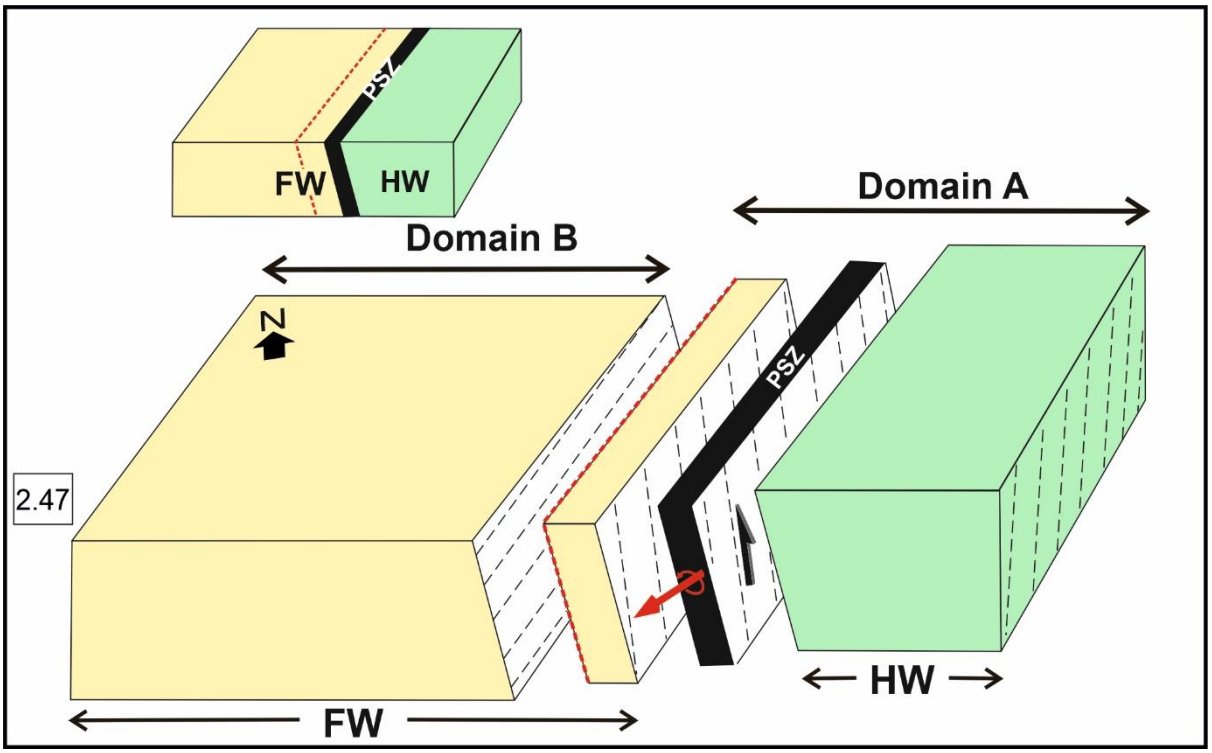

Figure 2.47: Schematic diagram showing the steep plunging lineation in footwall close to PSZ, at PSZ and in hangingwall rocks (marked as domain A) and gentle plunging lineation in the footwall distant from PSZ (marked as domain B).

to the vorticity axis and the measured W_n value is >0.81 demonstrating a large component of simple shear. In contrast, Phulad granite and the associated host rocks show gentle plunging stretching lineation in the footwall unit that is away from the shear zone (marked as Domain

B in Figure 2.47). In this domain, the stretching lineation is parallel to the vorticity axis and is characterized by the low value of W_n (<0.51) signifying a large component of pure shear. In three-dimensional transpression shear, the footwall (Domain B) acted as a competent buttress and accommodates the coaxial component, whereas Domain A accommodates the noncoaxial deformation of flow with stretching lineation parallel to the movement direction (Fossen et al., 1994; Tikoff and Greene, 1997; Goodwin and Tikoff, 2002; Sengupta and Ghosh, 2004). Thus, for the present study, this switching of stretching lineation from steep to gentle lineation in Phulad granite and its country rocks across the PSZ is mainly controlled by the ratio of pure and simple shear strain rates.

Chapter 3

Microstructure and Grain-size Analysis

3.1 Introduction:

A detailed microstructural study was carried out for the Phulad granite based on transmitted light microscopy of more than 100 orientated thin sections. The following sections cover the sample preparation, detailed microstructure and grain size analysis. And finally, a discussion is done at the end of this chapter.

3.2 Sampling and Data Processing:

For laboratory studies, more than 100 thin sections were prepared. Thin sections are made by cutting perpendicular to the foliation, parallel to the lineation (i.e., XZ section), and perpendicular to the foliation, lineation (i.e., YZ section). First, microstructural observations were carried out of the thin sections under a high-resolution optical microscope (Leica DM750P). The photomicrographs were captured for data processing using a standard image analyzer software (LAS Image analyzer, V4.13.0, 2017). For grain-size analysis, granitic rocks were preferentially collected from different locations of the western and eastern parts of PSZ (Figures 3.1-3.2) in a way that the rocks were sufficiently rich in quartz. For grain size analysis, 'Image J' software (V1.53t, 2022) was used. It was possible to distinguish recrystallized quartz grains from the other feldspar porphyroclasts and large quartz grains visually by their contrasting size distributions.

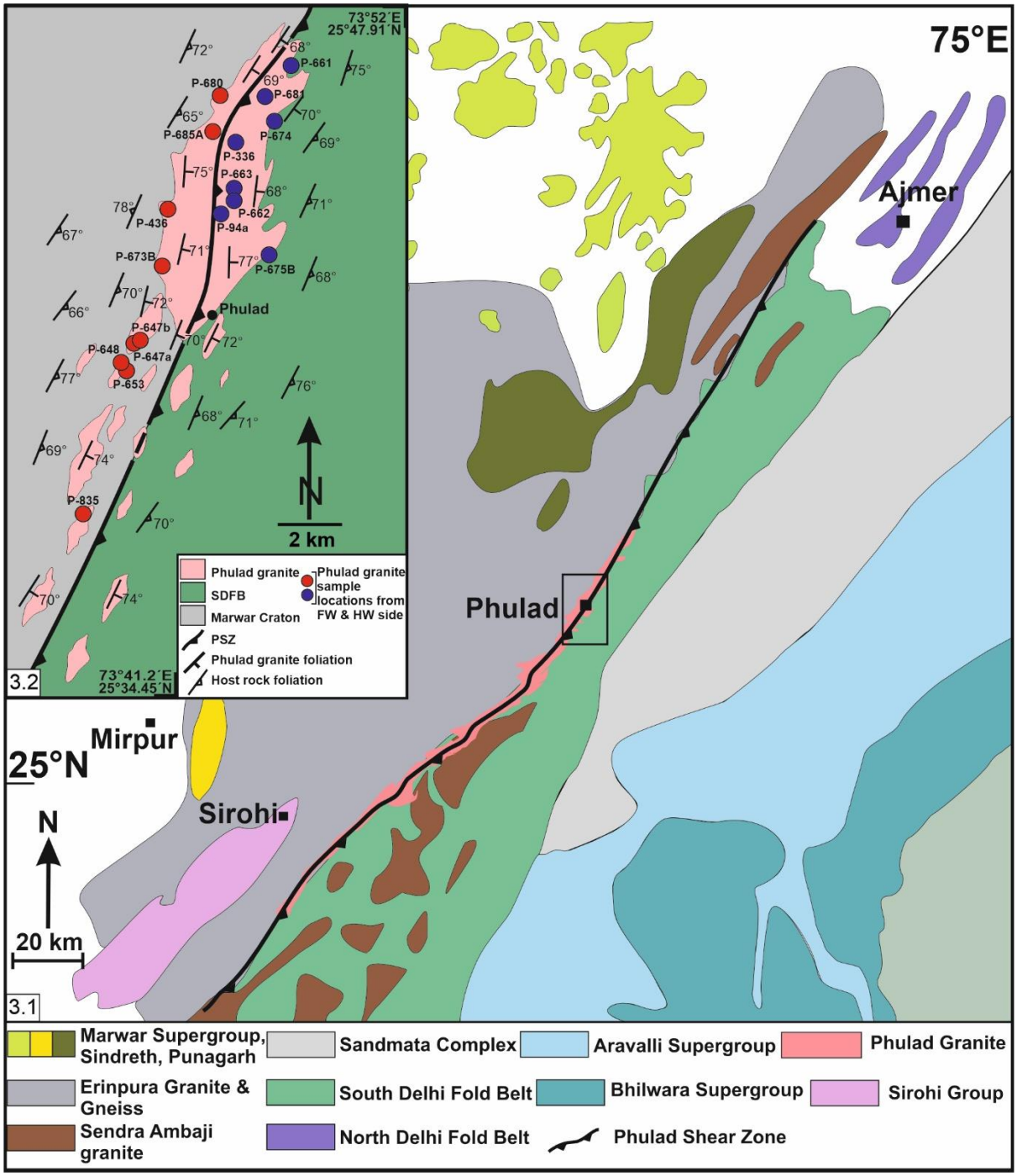

Figure 3.1-3.2: (3.1) Geological map depicting the different crustal domains in northwestern India, modified after Heron (1953); Gupta et al. (1980) and Roy and Jakhar (2002). (3.2) Detailed lithological map of Phulad granite with foliation marked with black box in (3.1).

3.3 Microstructure:

The Phulad granites are medium to coarse grained rock and contain quartz, feldspar (both K-feldspar and plagioclase), biotite, and muscovite. The granite is characterized by bi-modal

grain size population with prominent euhedral phenocrysts of K-feldspar (2–6 cm long) in a fine-grained (<3 mm) mosaic of recrystallized feldspar and quartz aggregates.

Microstructural study shows interlocking texture formed by magmatic feldspar, quartz, and biotite (Figure 3.3). Alkali feldspar shows simple twin interfaces parallel to the foliation (Figure 3.4). Fine grained aggregates of late magmatic minerals (quartz and feldspar) occur between fragmented primary feldspar grains (Figure 3.5).

Solid-state deformation features are also there, such as large quartz grain shows chessboard twinning (Figure 3.6). This feature is very common in this granite. Recrystallized

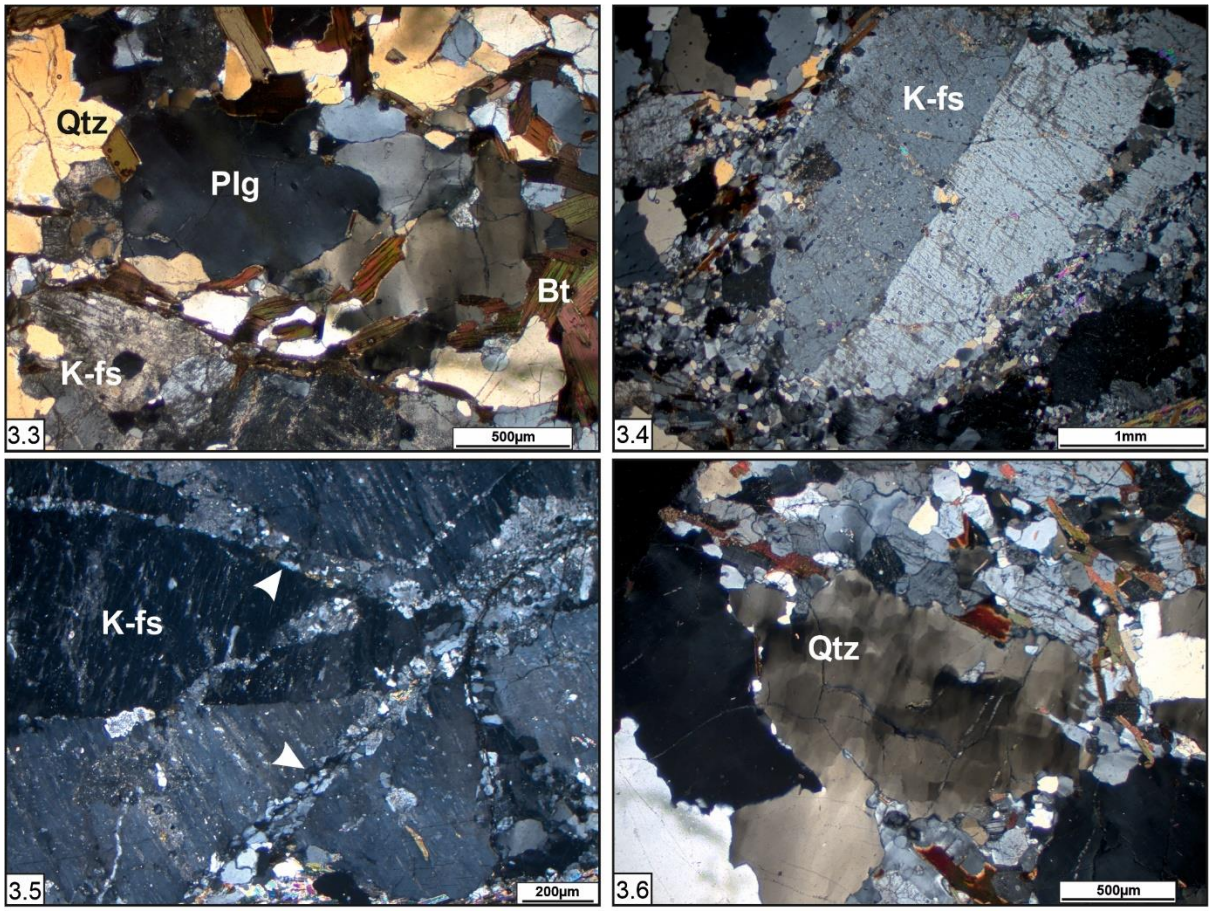

Figure 3.3-3.6: Photomicrographs of Phulad granite in cross polarized light showing interlocking texture in between K-feldspar, plagioclase, quartz, and biotite (3.3), elongated alkali feldspar phenocryst that is sub-parallel to the foliation shows simple twinning (3.4), submagmatic fractures in K-feldspar phenocryst has been filled by fine-aggregates of quartz and feldspar marked with arrow head (3.5), chessboard sub-grain is prominent in large quartz grain (3.6). Plg-Plagioclase, Qtz- Quartz, K-fs- K-feldspar, Bt-Biotite.

quartz and oblique quartz grain as shown in figure 3.7. Prominent subgrain boundary with localization of deformation band is common in feldspar (Figure 3.8). Bulging and irregular

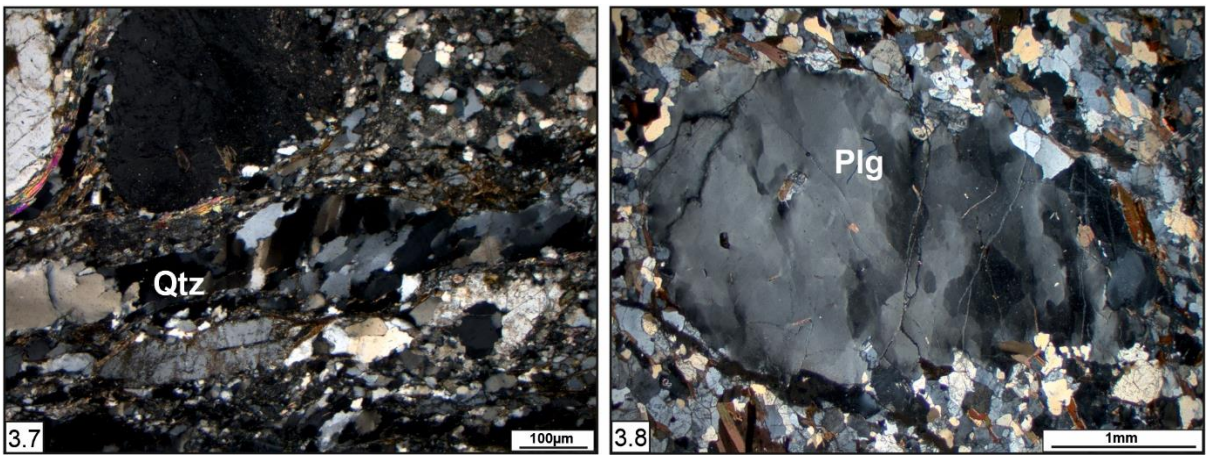

Figure 3.7-3.8: Photomicrographs of Phulad granite in cross polarized light showing recrystallized oblique quartz grains show top to right shear sense (3.7), prominent subgrain boundary in plagioclase (3.8), Plg- Plagioclase, Qtz- Quartz.

grain boundaries (Figures 3.9, 3.10) and nucleation of dislocation free cores of new grains surrounding the old crystal (Figure 3.11) are there. Feldspar grains show the effect of

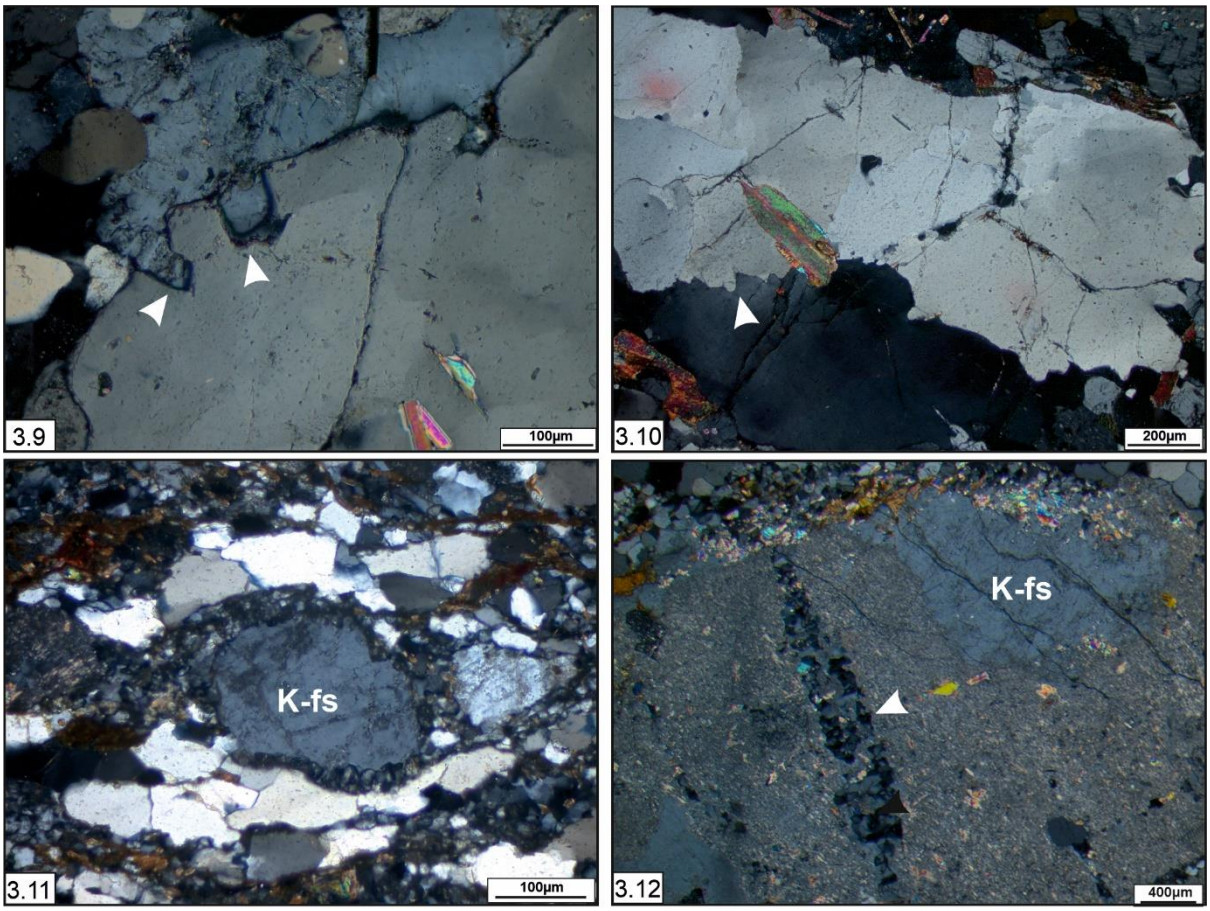

Figure 3.9-3.12: Photomicrographs of Phulad granite in cross polarized light showing bulging (BLG) in feldspar (3.9), grain boundary migration (GBM) in quartz (3.10) marked with arrow head, core-mantle structure in feldspar (3.11), sericitization, and some brittle fractures in K-fs (3.12). K-fs- K-feldspar.

sericitization, and some brittle fractures are there (Figure 3.12). The Inclusion of biotite and muscovite is common within K-feldspar phenocrysts; at some places needle-shaped inclusion of muscovite is arranged in an angular manner (60° to each other) (Figure 3.13). Lobes of myrmekites and flame perthite within feldspar grains are common (Figure 3.14). Development of polycrystalline quartz-feldspar aggregate with relict of deformed old grains is there. Polygonized quartz grains with triple point junctions are common in the matrix quartz (Figure 3.15). Biotite flakes show kinking and bending structures (Figure 3.16).

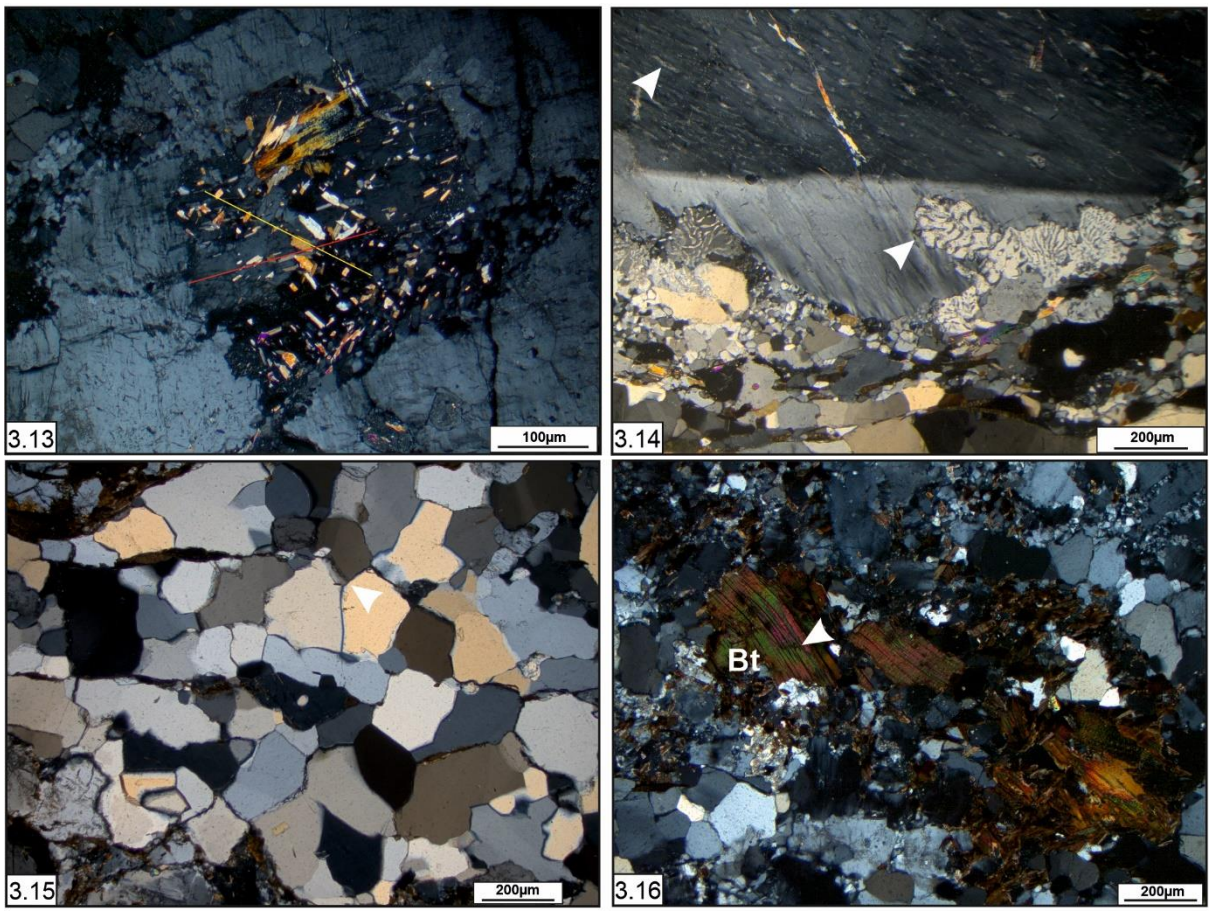

Figure 3.13-3.16: Photomicrographs of Phulad granite in cross polarized light showing inclusions of micas in K-feldspar (3.13), myrmekites and flame perthite within feldspar (3.14), polygonised quartz shows triple junction (3.15), biotite flakes show kinking and bending structure, micro fracture showing with arrow head (3.16). Bt-Biotite.

The Phulad granites are variably deformed. The granitic rocks away from the shear zone are coarse grained and characterized by large porphyroclasts of feldspar (mainly K-feldspar)

within a groundmass of fine to medium grained assemblage of quartz, feldspar, biotite, and muscovite. These porphyroclasts show a very well-defined tail geometry.

Towards the shear zone, granites show more evidence of deformation, the size of porphyroclasts decreases and the percentage of matrix increasess here. Feldspar porphyroclasts show irregular grain boundaries with strong undulose extinction. Quartz ribbon also warps large feldspar clasts (Figure 3.17). The grain boundaries within the

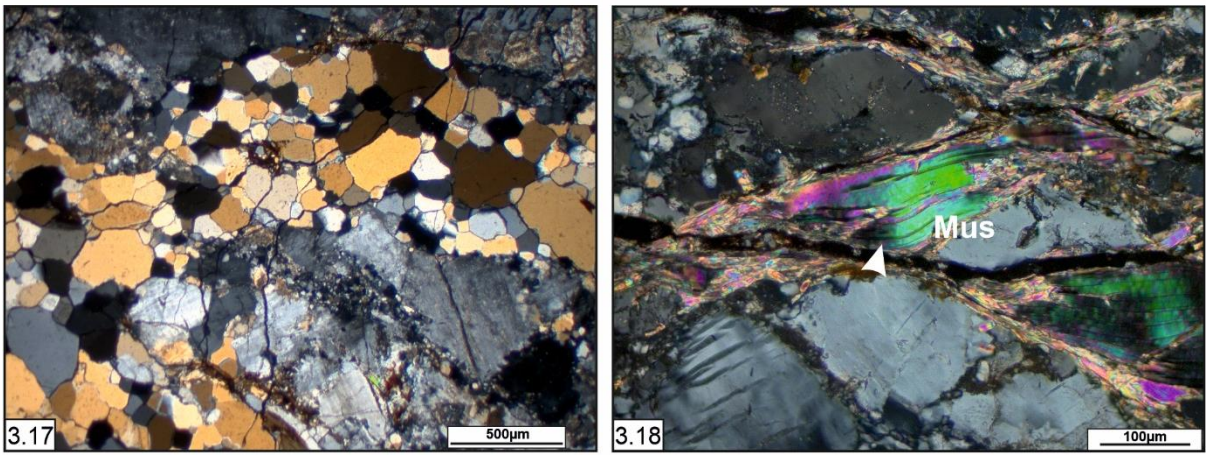

Figure 3.17-3.18: Photomicrographs of Phulad granite in cross polarized light showing quartz ribbon warps feldspar clast (3.17), kinematic indicator mica fish (3.18). Mus- Muscovite.

polycrystalline aggregate of quartz-feldspar show strongly curved and lobate-cuspate structures (seriate-interlobate fabric). Kinking and folding in muscovite are common. At some places, isolated mica-fish have their long axis with the extensional quadrant of the deformation, the foliation plane (Figure 3.18). Whereas biotite grains show undulose extinction and micro-fracturing (Figure 3.16).

Farther towards the shear zone, the rock becomes mylonite with few remnants of porphyroclasts and finally transforms to ultramylonite. These mylonites and ultramylonites show a strong foliation. Most of the feldspar clasts are stretched parallel to the mylonitic foliation. These flattened clasts are stretched along the foliation plane (XY section).

Few feldspar grains show strong undulose extinction with irregular grain boundaries. Mantled porphyroclasts of feldspar with proper tail geometry are present within shear bands consisting of very fine grain aggregate of quartz-feldspar and mica (Figure 3.19). Quartz mainly occurs as bands forming ribbon structures with curved grain boundaries. The formation of quartz subgrain within the ribbon structure is also common (Figure 3.20).

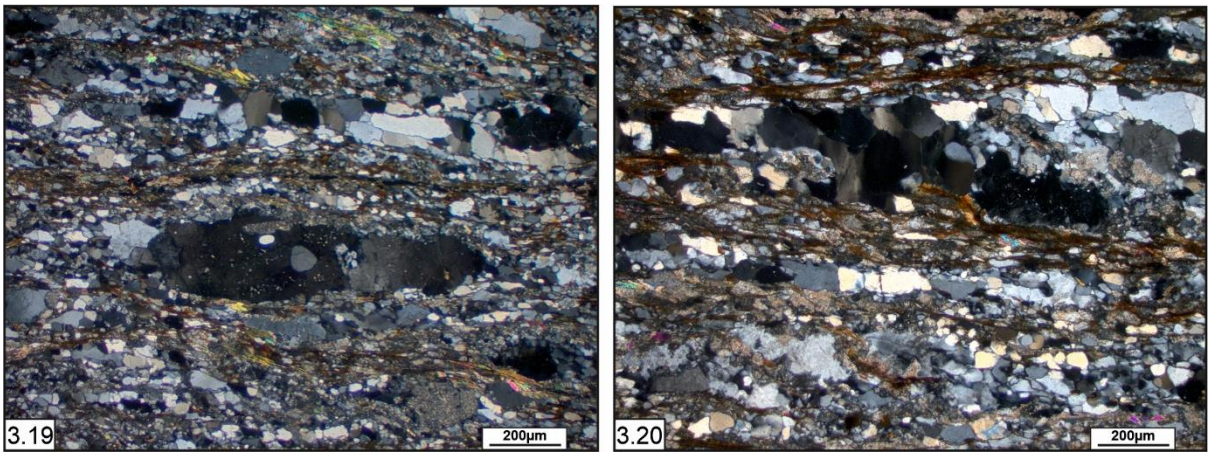

Figure 3.19-3.20: Photomicrographs of Phulad granite in cross polarized light showing mantled feldspar porphyroclast (3.19), quartz subgrain within ribbon structure (3.20).

At the PSZ, the Phulad granite changes to strongly deformed mylonite and ultramylonites. Occurrences of S-C fabric are common (Figures 3.21-3.22). Feldspar phenocrysts in the deformed variety show major development of asymmetric tail patterns. On the horizontal section (perpendicular to foliation and lineation), the asymmetric tail (Sigma and Delta clasts) shows a sinistral sense of movement (Figures 3.21-3.23). The asymmetric tail pattern of feldspar phenocrysts on the vertical section (perpendicular to foliation and parallel to lineation) shows a top-to-the-NNW reverse sense of movement (Figure 3.24). There is a gradational change towards the shear zone as the grain size is reduced from porphyritic granite to ultramylonite.

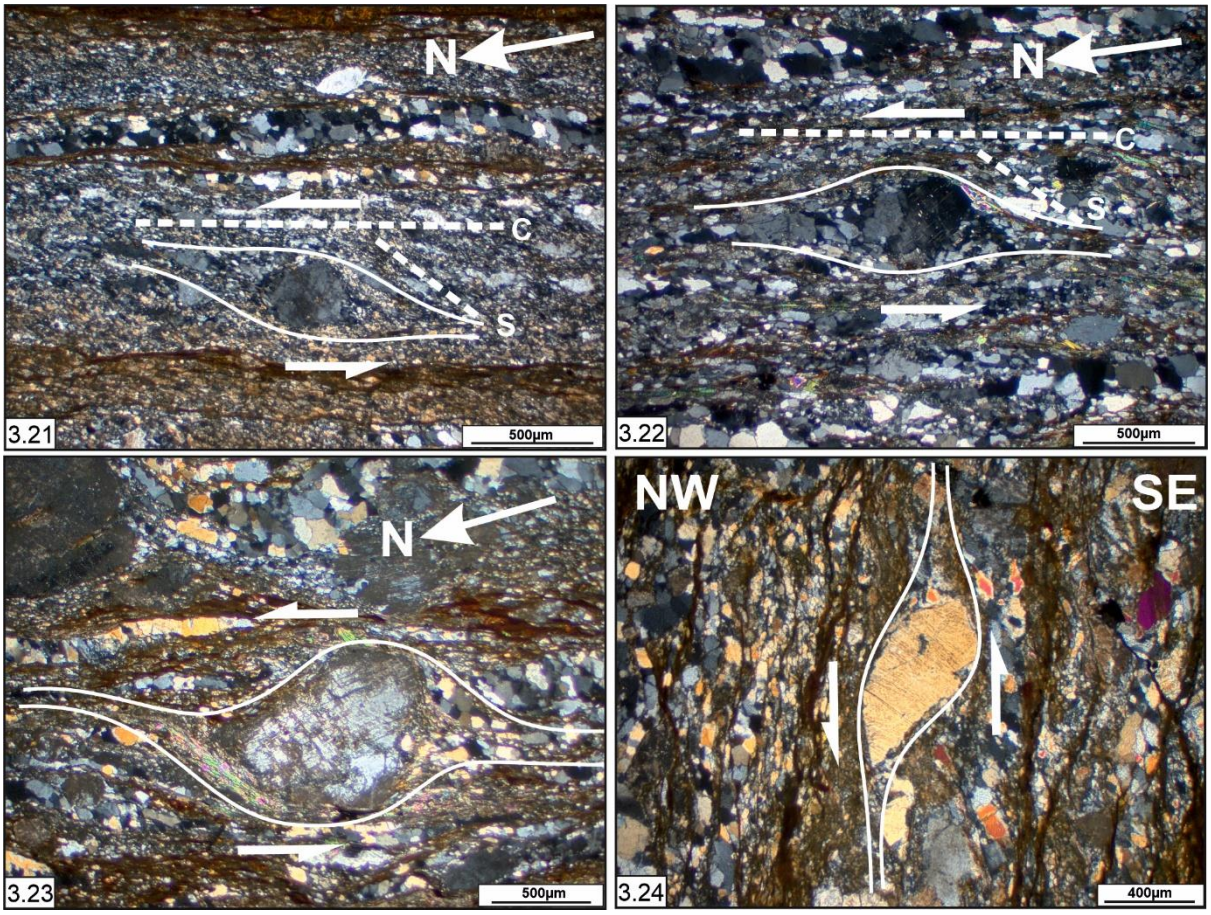

Figure 3.21-3.24: Photomicrographs of Phulad granite in cross polarized light showing asymmetric tail pattern shows the sense of shearing.

3.4 Grain-size Analysis:

The microstructural characterizations have a good relationship with the recrystallization or deformation mechanisms commonly occur in quartz and feldspar mineral grains which can estimate the deformation temperature (Louis et al., 1986; Hirth and Tullis, 1992; Stipp et al., 2002a). New techniques of microstructural characterization and textural parameter calculation, such as fractal dimension study, piezometric study etc., are helpful in investigating the thermal history and the stress-strain condition of granitic rocks.

Quartz grains were analyzed as they are mostly affected by deformation. Feldspar grains have an aspect ratio that varies from 1.08 to 2.7, whereas quartz has 1.20 to 5.17 (Figure 3.25). The matrix quartz grains are more stretched than the feldspar grains. In the plot, the

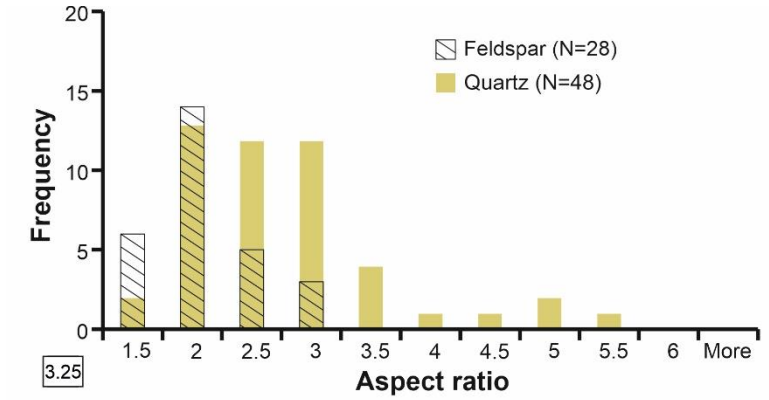

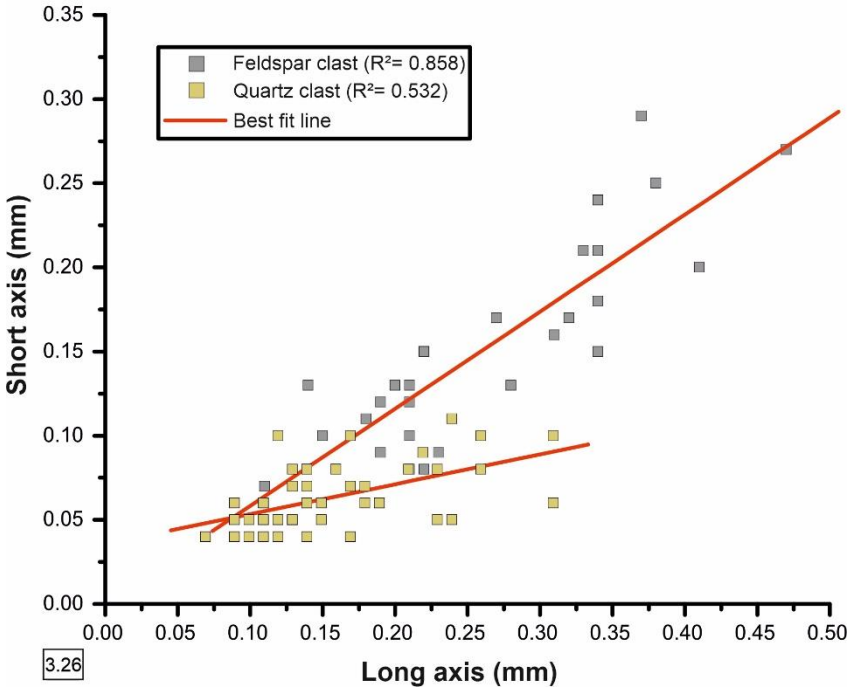

short axis vs. long axis, positive best-fit lines are there in the case of both feldspar and quartz grains having R^2 (correlation coefficient) = 0.858 and 0.532, respectively (Figure 3.26). Only recrystallized quartz grains are used for grain size analysis.

Figure 3.25-3.26: (3.25) Histogram showing higher aspect ratio of recrystallized quartz grains than feldspar grains. (3.26) Plot of long axes vs. short axes of quartz and feldspar showing overall small size of recrystallized quartz grains than feldspar.

3.4.1 Fractal analysis:

The area-perimeter fractal dimension analysis of quartz grain is a suitable method to calculate fractal dimension value related to the deformation temperature and strain rate (Takahashi et al., 1998).

The 2D size of each recrystallized grain was approximated using the method of Stipp et al. (2006), where a circle (diameter, d) was considered with an equivalent area of the grain under consideration, as demonstrated in figures 3.27-3.28 (Cross et al., 2015a, b). The grain

diameter (d) of a circle having the same area (A) and perimeter (P) of a quartz grain was also measured. d and P of quartz grains (at least 70) were measured from each thin section. Takahashi et al. (1998) demonstrated that d and P of quartz have a relation, $P \propto d^D$, where D is the fractal dimension. The d and P values from the quartz grains are plotted on a log-log graph to obtain a least-square linear best fit to the data. This slope of the best-fit line provided the

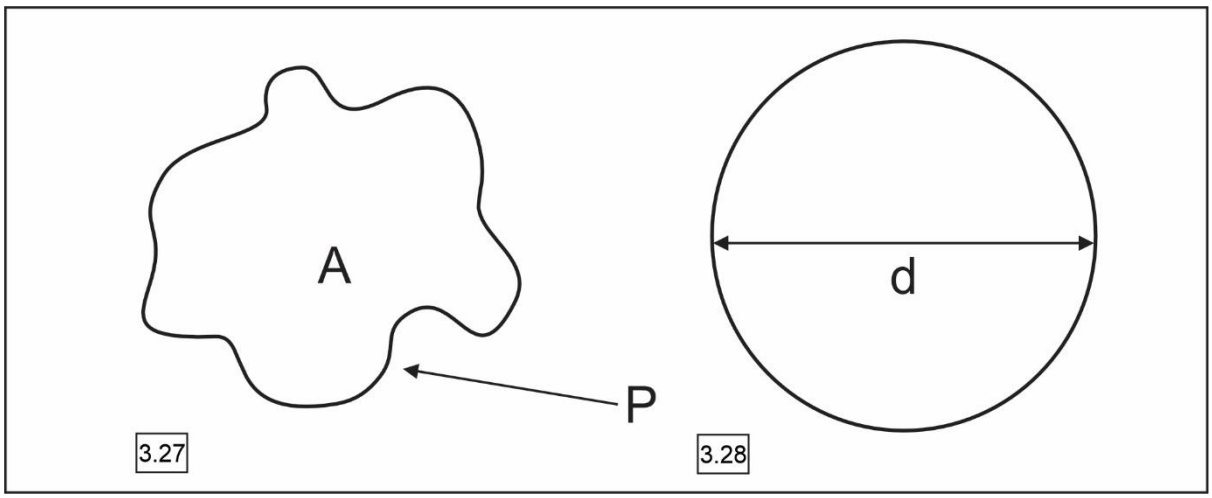

Figure 3.27-3.28: (3.27) Schematic diagram of a grain having area 'A' and perimeter 'P' equivalent to (3.28) circle having diameter 'd'. Geometrical considerations for the analysis of grain size (d) and fractal dimension (D).

fractal dimension (D) for the given sample. Since measurements are made from two-dimensional images (photomicrographs), according to Takahashi et al. (1998), D value should be $1 \leq D \leq 2$.

The Phulad granite 1800-3000 meters away from the PSZ with D= 1.007 ± 0.017 having correlation coefficient (R^2) = 0.988. At 800-1000 meters away from the PSZ, the same granites have D values 1.017 ± 0.015 and 1.018 ± 0.034 with correlation coefficient (R^2) = 0.987 and 0.962, respectively. At 500 meters from the shear zone, the granites have a D value 1.031 ± 0.022 with a correlation coefficient (R^2) = 0.985. All plots are shown in figures 3.29-3.32. So, the granites denote a relation between the D value and distance from the shear zone. As the

D value is inversely proportional to temperature, it can be said that the granitic samples close

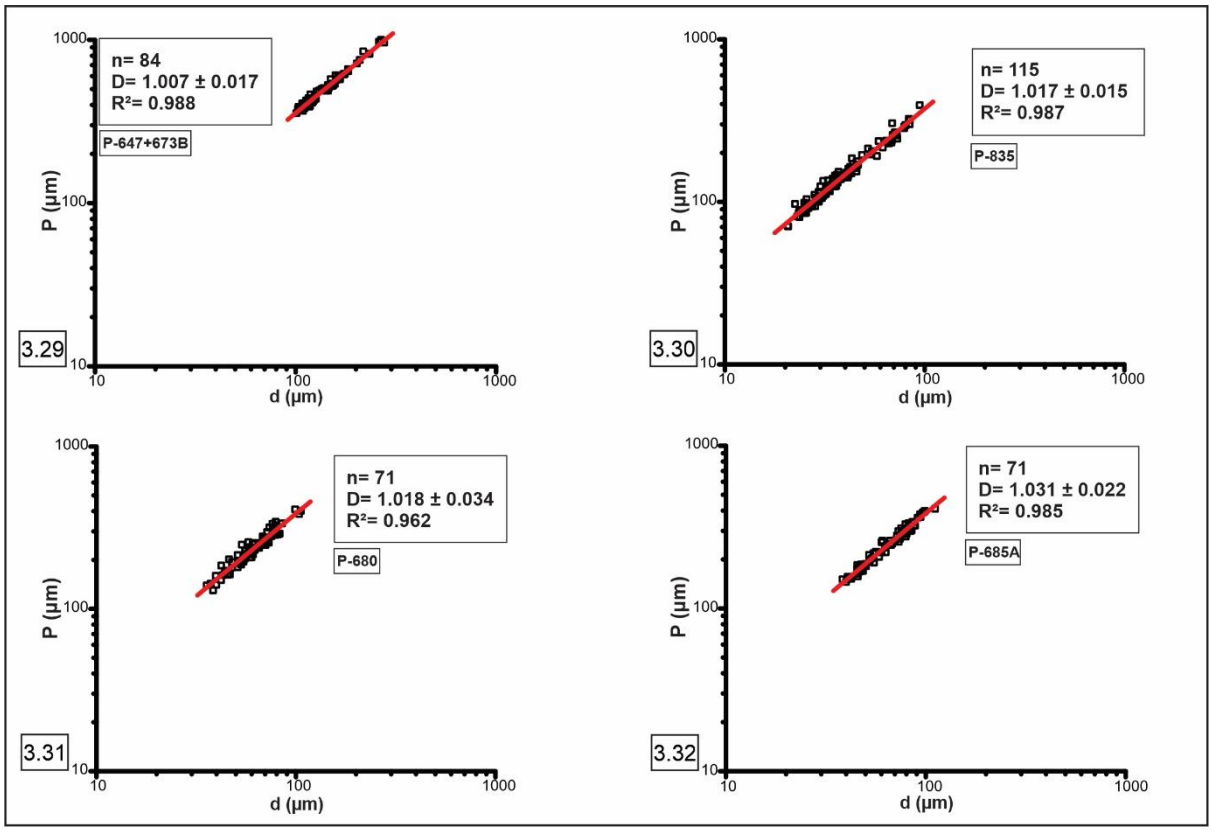

Figure 3.29-3.32: Log-log plots of perimeter (P) versus grain size (d) data of recrystallized quartz grains. The slope of the least-square linear fit gives the area-perimeter fractal dimension (D), which is given on each plot along with their grain numbers (n), linear regression (R^2) and sample number mentioned in Figure 3.1.

to the shear zone have lower temperatures (250 ˚C- 300 ˚C) than the granites, which are at a higher distance from the shear zone. Though all granitic samples are from the same source, the deformed granites, close to the shear zone (sample no.-685A), show slightly lower temperatures. But the shearing effect is not that much to give rise to the temperature of the associated rocks.

3.4.2 Strain rate measurement:

Kruhl and Nega (1996) demonstrated the fractal behaviour of quartz grain-boundary and investigated fractal dimension (D_r) with the ruler method and found that as the fractal (ruler) dimension decreases, temperature increases with less serration and vice versa. So, based on this research, they have proposed that the strain rate can be estimated from the D value and

temperature of the dynamically recrystallized quartz grains. However, these methods have been used in limited areas (Mamtani and Greiling, 2010; Ghosh et al., 2016; Kalita et al., 2022) to determine the temperature or strain rate in naturally deformed rocks.

Takahashi et al. (1998) analyzed the fractal dimension of quartz grain boundaries in experimentally deformed samples using the area-perimeter method and suggested its application as a strain-rate gauge. The relation between area–perimeter fractal dimensions (D in the present study) and strain rate (ἐ) is

$D= \Phi \log \dot{\varepsilon} + \rho/T+1.08$, (1)

where $\Phi= 9.34*10^{-2}\{[\log(s^{-1})]^{-1}\}$ and $\rho = 6.44 * 10^2$ (K) (Takahashi et al., 1998). The equation shows that D increases with strain rate, ἐ and decreases with temperature, T. Thus, fractal dimension changes with changing conditions; if D and T (in K) are known, ἐ (s^{-1}) can be calculated using equation (1).

For D values 1.017 ± 0.015 and 1.018 ± 0.034 with temperature 727 ˚C, strain rates are $\dot{\varepsilon}= 10^{-7.57}$ s^{-1} and $10^{-7.56}$ s^{-1} respectively. With D value 1.007 ± 0.017 and temperature 750˚C, strain rate $\dot{\varepsilon}= 10^{-7.52}$ s^{-1}. With D value 1.031 ± 0.022 and temperature 650 ˚C, strain rate $\dot{\varepsilon}= 10^{-7.99}$ s^{-1}.

D= 1.031(for deformed granite, Figure 3.32) and different T (600, 500, 400, 300 ˚C) were used to calculate ἐ using equation (1) and got $10^{-8.46}$ s^{-1} at 600 ˚C, $10^{-9.42}$ s^{-1} at 500 ˚C, $10^{-10.77}$ s^{-1} at 400 ˚C and $10^{-12.53}$ s^{-1} at 300 ˚C. To compare, even D= 1.007 (for magmatic granite, Figure 3.29) and different T (600, 500, 400, 300 ˚C) were used for the same and got $10^{-8.67}$ s^{-1} at 600 ˚C, $10^{-9.74}$ s^{-1} at 500 ˚C, $10^{-11.03}$ s^{-1} at 400 ˚C and $10^{-12.85}$ s^{-1} at 300 ˚C. On the other hand, samples with D value 1.017 show $10^{-8.57}$ s^{-1} at 600 ˚C, $10^{-9.64}$ s^{-1} at 500 ˚C, $10^{-10.92}$ s^{-1} at 400 ˚C and $10^{-12.74}$ s^{-1} at 300 ˚C.

3.4.3 Differential flow stress measurement:

Differential flow stresses of the Phulad granite were estimated using the quartz piezometer of Stipp and Tullis (2003). This calculation considers the "Griggs apparatus correction" provided by Holyoke and Kronenberg (2010). Differential flow stress (σ) is related to the grain size (d) as,

$\sigma = Bd^{-p}$, (2)

where d is the grain size (μm), and B=668.95, p=0.7936 are experimentally derived empirical constants (Twiss, 1977; Stipp and Tullis, 2003) that depend on the microscale dynamic recrystallisation mechanism. All these samples (P-680, P-685A, P-436, P-673B, P-647a, P-647b, P-648, P-653, P-835) are from the footwall side (Figure 3.2, red dots) and with variations in lineation such as sub-vertical to sub-horizontal lineation. The Phulad granites show different differential flow stress (σ) with distance (meter) from the PSZ. In figure 3.33, it is

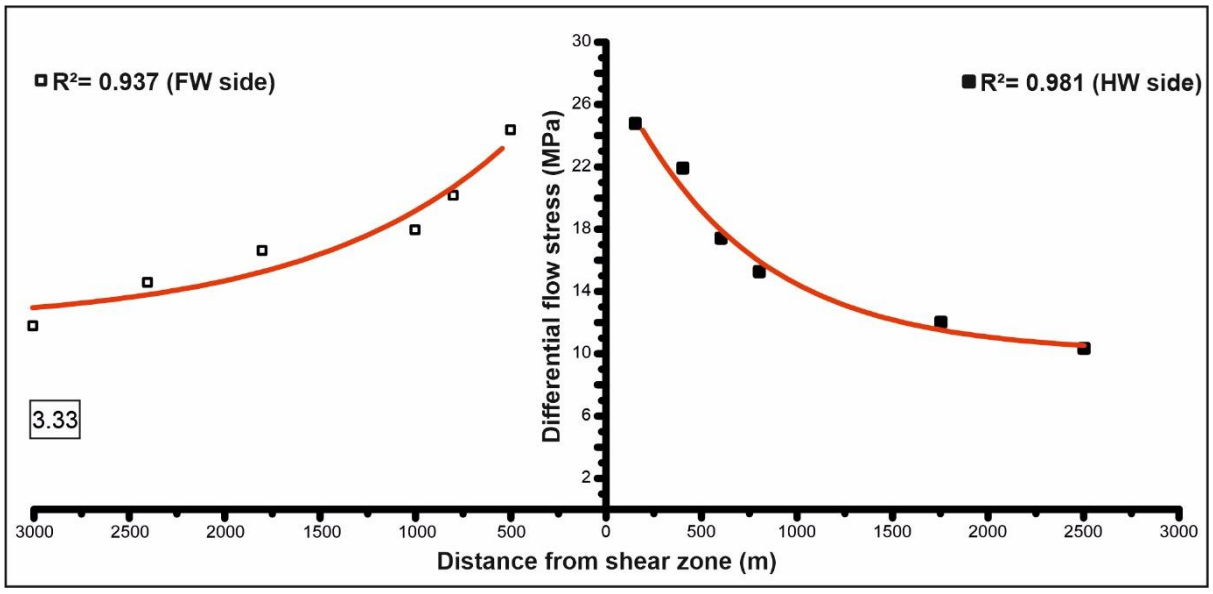

Figure 3.33: Differential flow stress (σ) exponentially varying with structural distance from Phulad shear zone (in meter).

shown that very close to the shear zone, about 500-800 meters, the granites (P-685a and P-835) have differential flow stress (σ) 24.35 MPa and 20.15 MPa, respectively. Grain size refining is also observed here as quartz grains vary from 46.55 to 83.61 μm and 58.93 to

112.31 µm, respectively. At ~1000 meters distance from the shear zone, the granite (P-680) shows σ =17.93 MPa and grains varying from 64.19 to 127.25 µm. Samples P-647 and P-436 at a distance ~1800-2400 meters from the shear zone show differential flow stress (σ) 16.60 MPa and 14.56 MPa, respectively and grain size varies from 71.97 to 162.08 µm and 112.76 to 146.08 µm respectively. P-673B sample is at ~3000 meters and shows differential flow stress (σ) 11.78 MPa with grain size variation from 123.91 to 261.26 µm. The entire flow stress data calculation is presented in table 3.1. All the granitic samples show variation in differential flow stress with varying distances from the shear zone.

Table 3.1: Estimated values of different parameters (deformation temperature, grain size and differential flow stress) from Phulad granite from footwall side.

Sample no.	Distance from PSZ (meter)	Microstructural evidence	Deformation temperature (˚C)	Grain size (d) (µm)			Differential flow stress (σ) on footwall side		
				Min.	Ave.	Max.	Min.	Ave.	Max.
P-685A	500	BLG	<650	20.64	30.94	45.53	19.95	24.35	31.75
P-835	800	BLG	650	29.36	54.31	94.52	15.78	20.15	26.33
P-680	1000	BLG-SGR	750-650	35.72	62.51	105.99	14.29	17.93	24.6
P-647	1800	SGR-GBM	~750	37.41	80.74	149.54	11.8	16.6	22.47
P-436	2400	SGR-GBM	>750	73.33	120.48	208.95	12.81	14.56	15.73
P-673B	3000	GBM	>750	103.68	167.59	276.54	8.08	11.78	14.6

At the shear zone, the granitic samples having sub-vertical lineation, the differential flow stress (σ) is slightly higher on the vertical section (perpendicular to foliation and parallel to lineation) as there is a reduction of grain size compared to the horizontal section (perpendicular to foliation and lineation). Towards the footwall side, granitic rocks having sub-horizontal lineation, the differential flow stress (σ) is slightly lower with higher diameter grains.

In case of the hangingwall side (Figure 3.2, blue dots), all granitic samples with sub-vertical lineation also show decreasing differential flow stress (σ) from close to the shear zone to distant from the shear zone i.e., 24.42 MPa for 150 meters to 10.34 MPa for 2500 meters, respectively. Data are presented in table 3.2. There is no change in lineation (throughout sub-vertical lineation) in the hangingwall side of the shear zone. The best-fit curve plotted against stress vs. distance and shows that the flow stress drops exponentially with increasing distance from PSZ (Figure 3.33). In comparison to the flow stresses of both the footwall and the hangingwall side granitic rocks, the rocks in the footwall side show slightly higher flow stress.

Table 3.2: Estimated values of different parameters (deformation temperature, grain size and differential flow stress) from Phulad granite from hangingwall side.

Sample no.	Distance from PSZ (meter)	Microstructural evidence	Deformation temperature (˚C)	Grain size (d) (μm)			Differential flow stress (σ) on hangingwall side		
				Min.	Ave.	Max.	Min.	Ave.	Max.
P-94a	150	BLG	<650	44.18	67.64	112.86	15.72	24.42	33.08
P-336	400	BLG	650	55.83	76.41	133.89	13.72	21.91	27.48
P-663	600	BLG-SGR	750-650	72.94	101.17	140.39	13.22	17.4	22.23
P-681	800	SGR-GBM	~750	91.44	119.53	186.61	10.55	15.27	18.58
P-674	1750	SGR-GBM	>750	104.05	161.71	223.53	9.14	12.02	16.77
P-675B	2500	GBM	>750	153.93	194.41	269.86	7.87	10.34	12.28

3.5 Summary:

3.5.1 Interpretation of microstructural features/ evidence of high temperature solid state deformation:

Microstructural study reveals several textural features that denote magmatic to sub-magmatic, high temperature, solid-state deformation. Interlocking texture, foliation parallel elongated alkali feldspar and fractured K-feldspar phenocryst healed by quartz aggregates imply the igneous texture and suggest that melt was there during the deformation (Figure

3.5). Quartz grains show a prominent chessboard subgrain boundary pattern (Figure 3.6) suggesting the temperature was relatively high during crystallization. Chessboard subgrains in quartz (Kruhl, 1996) are a distinctive deformation microstructure used as an indicator of high-temperature (>550–600 °C) deformation. Prominent subgrain boundary with localization of deformation band is common in feldspar (Figure 3.8), which suggests a recovery process. Further, the subgrain boundary rotation axes are parallel to the main grain boundary indicating a recovery process (Trépied et al., 1980). Bulging and irregular grain boundaries (Figure 3.9) and nucleation of dislocation free cores of new grains surrounding the old crystal suggest Grain Boundary Migration (GBM) (Figure 3.10) recrystallization (Passchier and Trouw, 1996). Therefore, it can be interpreted that both high temperature GBM (500–700 ˚C) as well as SGR (400–500 ˚C) recrystallization mechanism simultaneously took place in this granite. According to Stipp et al. (2002a), GBM recrystallization takes place at the highest temperature range, between 500 ˚C and 700 ˚C. Polycrystalline quartz-feldspar aggregate with relict of deformed old grains suggests predominant recrystallization. Lobes of myrmekites and flame perthite within feldspar grains are common (Figure 3.14), which are reported to develop between 450-670 ˚C (Vernon, 2004). Polygonized quartz grains with triple point junction are common in the matrix (Figure 3.15), suggesting GBAR that reduces internal energy polycrystalline materials migrate their grain boundaries to become straight (Vernon, 1976; Poirier, 1985). Biotite and muscovite grains are kinked/bent (Figures 3.16, 3.18), which develop at <300 ˚C are common. The amount of polycrystalline quartz-feldspar aggregate is higher, and relicts of deformed old grains are also present, suggesting SR recrystallization. Deformation twins in plagioclase are also abundant in deformed granites at the shear zone and these require a low temperature (400-500 ˚C: Passchier and Trouw, 2005) down to below 300 ˚C for kink bends in biotite and high strain rate (Vernon, 2004).

These microstructures suggest that Phulad granite preserves magmatic to sub-magmatic, high and low-temperature solid-state deformation structures. The microscopic features mentioned above show strong criteria that the deformation was there prior to complete crystallization (Paterson et al., 1989; Saint-Blanquat and Tikoff, 1997; Vernon et al., 2004) of the Phulad granite. As there are some evidences of intracrystalline deformation and static recovery in all the variably deformed granites, it can be said that the temperature was quite high after the cessation of the deformation. The estimated temperature of regional metamorphism during PSZ shearing, calculated from a closely spaced associated pelitic rock, shows a temperature of ~600 ˚ to 630 ˚C (Chatterjee et al., 2017). In a shear zone, additional heat can be generated because of shearing and the temperature can be sufficient enough to form a chessboard in a granitic rock (Büttner, 1999; Greiling et al., 2014; Mukherjee, 2017; Parsons et al., 2018). In such a case, the high-temperature deformation features should be restricted to the areas close to the shear zone. However, the quartz chessboard texture (Vegas et al., 2011; Martins et al., 2013; Fazio et al., 2020) is ubiquitous in the Phulad granite, irrespective of their occurrences to PSZ (Figure 3.34). So, shear heating (Mulchrone and

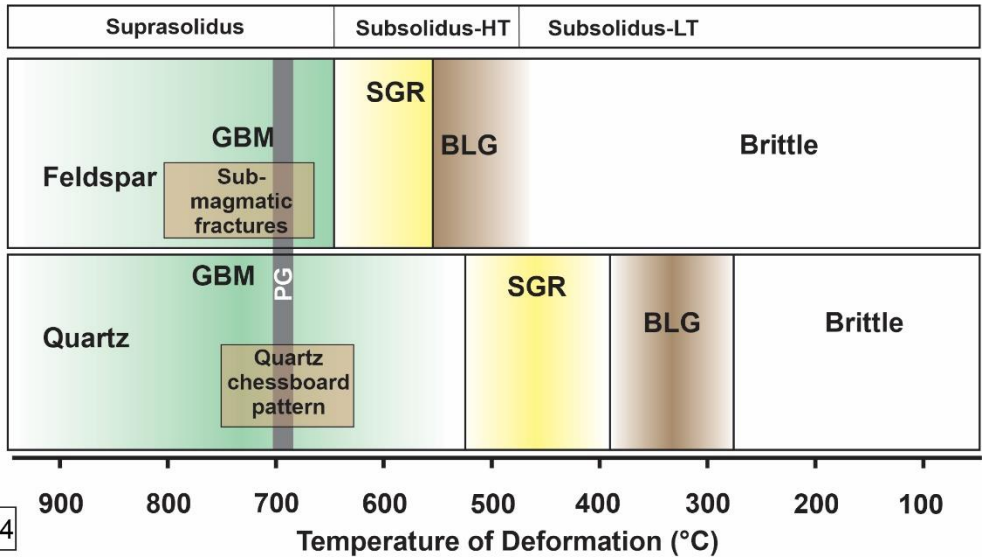

3.34

Figure 3.34: Temperature range estimated graph (after Guillope and Poirier, 1979; Tullis and Yund, 1991; Fitz Gerald and Harrison, 1993; Altenberger, 2000; Rosenberg and Stünitz, 2003; Passchier and Trouw, 2005; Urai et al., 2011; Fazio et al., 2020) based on deformation mechanisms and microstructures for feldspar and quartz of Phulad granite (PG; marked with grey band). BLG= bulging recrystallization; SGR= subgrain rotation recrystallization; GBM= grain boundary migration recrystallization.

Mukherjee, 2016) cannot be the appropriate source for the formation of quartz chessboard in the Phulad granite. The Phulad granite itself was hot during deformation, which could be the reason for chessboard formation in quartz.

3.5.2 Interpretation of fractal dimension calculation and associated deformation mechanism:

Fractal dimension (D) of recrystallized quartz grains was measured with the area-perimeter method and varies with BLG-SGR transition to GBM with variation in distance from the PSZ. Kruhl and Nega (1996) have shown that quartz's fractal geometry of sutured grain boundaries is a potential geo-thermometer. The present study of the naturally deformed granite shows that recrystallized quartz grain shapes are characterized by self-similar geometry of their boundaries. The corresponding fractal dimension (D), an indicator of complexity in grain boundary geometry, varies systematically with the deformation mechanism, laterally changing from the BLG to SGR. At low temperatures and high strain-rate, the BLG becomes the most dominant mechanism, leading to the recrystallization of quartz grains with strongly irregular grain boundaries. This mechanism eventually leads to microstructures with relatively greater fractal dimensions.

Estimated D values (1.007 ± 0.017 to 1.031 ± 0.022) from this study are lower than that of (1.14 ± 0.06 to 1.30 ± 0.07) reported from rock deformation experiments (Takahashi et al., 1998). However, these experiments were performed at temperatures <900 ˚C and strain rates 10^{-5} to 10^{-6} s^{-1}, which far exceed natural strain rates (10^{-13} to 10^{-15} s^{-1}, Bose and Mukherjee, 2020). Very close to the shear zone BLG recrystallization is dominant with the D value 1.031 ± 0.022. Further moving away from the shear zone, the granites having SGR is overprinted upon BLG with the D value 1.018 ± 0.034 and 1.017 ± 0.015. And the granites distant from the shear zone show GBR along with SGR having a D value 1.007 ± 0.017.

A recent study by Stipp et al. (2010) has recognized the grain size population plays an important role in recrystallization. With this approach, our present study shows changes in fractal dimension (D) value. BLG is the most active deformation mechanism in the grain size range from 20-95 µm. SGR is dominated in the grain size range from 60-120 µm and GBR is dominated from 100-270 µm. So, in the Phulad granite, almost all the recrystallization mechanisms played an important part, but on the basis of grain size and fractal dimension, recrystallization mechanisms can be distinguished space wise.

3.5.3 Interpretation of strain and differential stress:

Strain rate calculation from naturally deformed rocks is a challenging matter. Bose and Mukherjee (2020) used finite strain analysis and suggested that the geological strain rate varies from 10^{-13} s^{-1} to 10^{-15} s^{-1}. Passchier and Trouw (2005); Twiss and Moores (2007) suggested that in natural geological systems, strain rates vary between 10^{-12} s^{-1} to 10^{-15} s^{-1}. However, strain rates calculated for higher temperatures for both the magmatic and mylonitic Phulad granites are incredibly high ($10^{-7.52}$ s^{-1} to $10^{-7.99}$ s^{-1}). The latter is closer to the experimental strain rate (Hirth and Tullis, 1992) and it is difficult to believe that this could be possible in nature. But for deformed granite a realistic strain rate of the order of $10^{-12.53}$ s^{-1} at 300˚C is obtained. Recent calculations by Vigneresse (2006) reveal that 10^{-10} s^{-1} values of the order of $10^{-12.56}$ s^{-1} are possible during emplacement. Therefore, the method to calculate strain rate using the area-perimeter fractal dimension of quartz grains could be erroneous for a high temperature syn-tectonic granite such as the Phulad granite. While at BLG recrystallization temperature range of 280-400 ˚C (Stipp et al., 2002a, b), mylonites to slightly deformed as well as the magmatic varieties show the strain rates in the range of natural systems such as $10^{-10.77}$ to $10^{-12.85}$ s^{-1}. In that case, the strain rates increase towards the shear zone at different temperatures for the deformed variety compared to the magmatic one.

Calculated differential flow stress (σ) from recrystallized quartz grains indicate that the flow stress varies from 24.35 MPa (very close to the PSZ) to 11.78 MPa (far from the PSZ) and this is quite low with respect to the naturally deformed rock (Bose and Mukherjee, 2020). As this flow stress depends on the grain size (Bose et al., 2018), very short distance variation from the shear zone could be the reason, and further study needs to be done.

Integrating the microstructures, deformation mechanism, grain size analysis, fractal analysis, and differential flow stress measurements suggest that there is temperature and stress-strain variation in the granite relative to the position of the proper shear zone and that depends upon the grain size of constituent minerals.

Chapter 4

Origin of K-feldspar Phenocrysts

4.1 Introduction:

Large euhedral shaped K-feldspar megacrysts are common in granitoid plutons (Vernon, 1986). The exact origin of K-feldspar phenocrysts can vary depending on the specific geological context. Different theories have been proposed by several authors (Vernon, 1986, 1990; Moore and Sisson, 2008; Johnson and Glazner, 2009; Glazner and Johnson, 2013) to justify the origin of K-feldspar megacrysts in granitic plutons.

Johnson and Glazner (2009) suggested that K-feldspar megacrysts in granite and granodiorite plutons are generally inferred to be early crystallizing phases that settled by magmatic sedimentation. Most of the microstructural, chemical, and mineralogical evidences support the igneous origin of the K-feldspar megacryst. And they have interpreted the megacrysts as phenocrysts (Gilbert, 1906; Bateman et al., 1963; Higgins and Kawachi, 1977; Mehnert and Buesch, 1981). The large size phenocryst is most likely related to K-feldspar nucleation difficulties in melts (Vernon, 1986). Though K-feldspar is usually the final mineral to begin crystallizing in granitic magmas, there is still plenty of melt present at that point, allowing the phenocrysts to grow (Vernon, 1986). According to Bowen's reaction series plagioclase feldspar should crystallize early before K-feldspar and therefore phenocrysts of plagioclase feldspar will be got rather than K-feldspars. But, when 50% of the crystallization has occurred and the remaining melt is potash rich and high fugacity of water can lead to the crystallization with higher growth rate of K-feldspar.

But some petrologists support metamorphic origin of the K-feldspar megacryst and they have interpreted the K-feldspar clasts as porphyroblasts (e.g., Anderson, 1937; Stone and Austin, 1961; Dickson, 1966) as the megacrysts are much larger than groundmass grains and they may occur in and across the boundary of enclaves and aplitic veins.

Two hypotheses have been suggested to explain the origin of the K-feldspar megacrysts in granite, namely (1) the megacrysts were porphyroblastic in nature that grew during the deformation event (Dickson, 1996) or, (2) the phenocrysts are porphyroclasts- residual phenocrysts that crystallized before the deformation event (Vernon and Paterson, 2002).

The Phulad granite is porphyritic in nature and contains K-feldspar clasts. However, the origin of these large K-feldspar grains has not been studied so far. So, there remain a question of whether the phenocrysts of K-feldspar are of igneous or metamorphic origin. This is important to understand the tectonics of NW India. Therefore, the present study focuses on the detailed microstructures of Phulad granite to understand the nature of the origin of K-feldspar megacrysts which is very crucial to infer whether these megacrysts are of magmatic or metamorphic in origin.

4.2 Mesoscopic Structures:

The Phulad granite is bi-modal in nature. The K-feldspar megacrysts are situated in the matrix of feldspar, quartz, and micaceous minerals. The megacrysts of K-feldspar present in Phulad granite are euhedral in shape and show planar crystal faces with simple twin interfaces. The majority of crystals are aligned parallelly to each other with the foliation. On average, the length of the megacrysts ranges from 2 to 6 cm. The large grains of K-feldspar are moreover aligned in a similar manner. Some of the K-feldspar megacrysts have rotated. The distribution of K-feldspar megacrysts in the Phulad granite differs, the granite not associated with pegmatite bodies containing the least clast aggregates and the megacrysts are not in contact (Figure 4.1) having proper euhedral shape. On the other hand, the granite which is associated with the pegmatite bodies shows closely spaced euhedral megacrysts of K-feldspar (Figure 4.2). But close to the shear zone, all the granites show very closely spaced clasts either

associated or not associated with pegmatite bodies. The Phulad granite associated with the pegmatite bodies is mainly present in the regional NS bends of the PSZ with greater width (sample locations with red dot in figure 3.2) compared to the regional NE-SW directions of the shear zone. The distribution of these megacrysts shows the magmatic foliation parallel to the tectonic foliation that has been preserved during the deformation event. Microgranitoid enclaves are also there in the preferred orientation parallel to the large K-feldspar grains (Figure 4.3). The orientation of the microgranitoid enclaves is dominantly in NNE-SSW directions. The aligned euhedral feldspar phenocrysts, deformed feldspar phenocrysts, and the microgranitoid enclaves occur parallel to each other. In some places, the K-feldspar megacrysts are present in both the Phulad granite and pegmatite body (Figure 4.4, marked with a white circle).

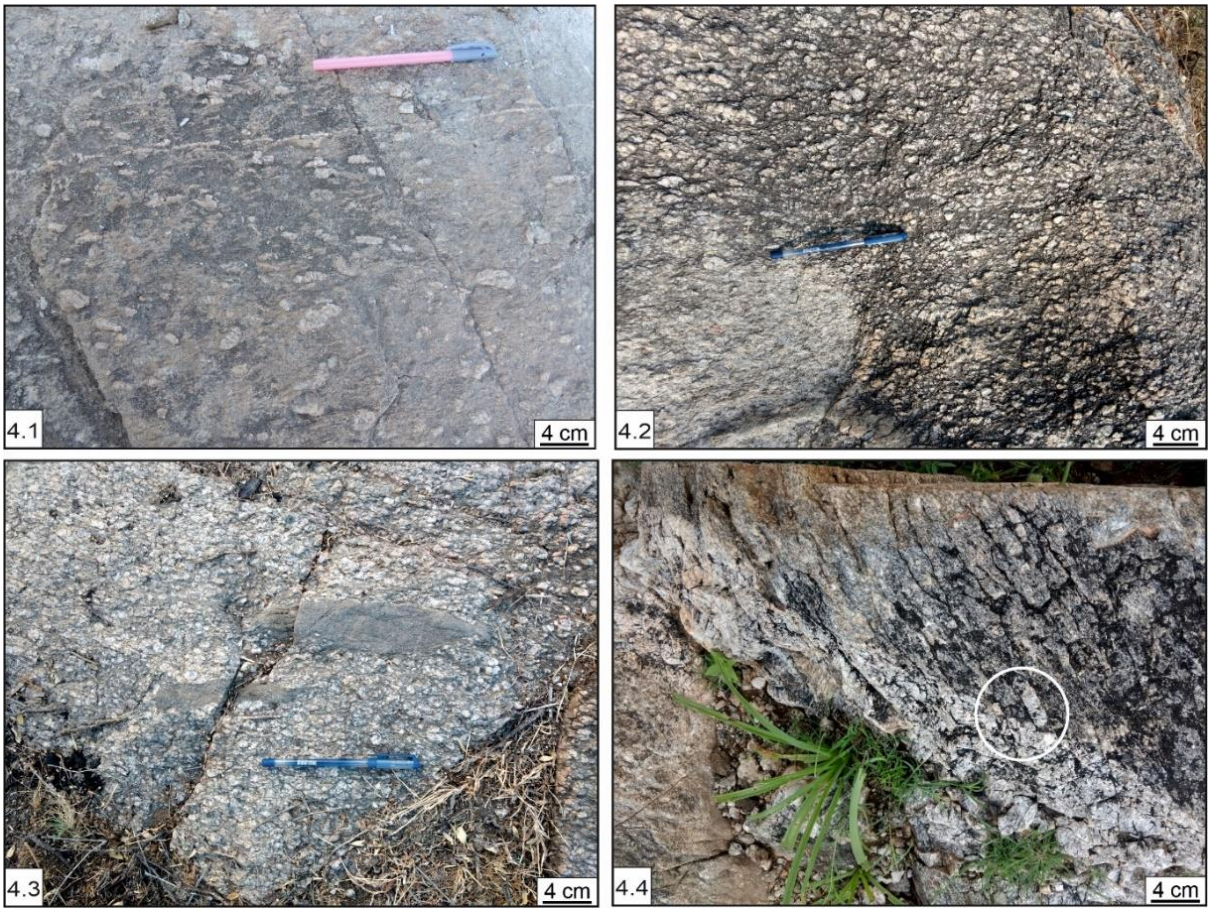

Figure 4.1-4.4: Field photographs showing (4.1) K-feldspar megacrysts (not in contact to each other) in the Phulad granite, (4.2) closely spaced euhedral megacrysts of K-feldspar, (4.3) microgranitoid enclaves are also there in preferred orientation parallel to the large K-feldspar grains, (4.4) K-feldspar megacrysts are present both in the Phulad granite and pegmatite.

4.3 Microscopic Structures:

For laboratory studies, more than 100 thin sections were prepared for this microstructural investigation. Crossed polar microphotographs are showing typical interlocking textures developed by feldspar, quartz, and mica (Figure 4.5). K-feldspar grains show simple twin interfaces parallel to the foliation (Figure 4.6). Fine-grained aggregates of later magmatic minerals of feldspar, quartz, and mica occurred in the fractures of the earlier large grains of K-feldspar showing with white arrowhead (Figure 4.7). In the Phulad granite, some of the K-feldspar crystals show undulatory extinction under a transmitted light microscope (Figure 4.8). Microcline twinning is mainly found in alkali feldspar, rich in potassium. It usually has a small proportion of sodium in its structure. Here the megacrysts show stronger intensity of

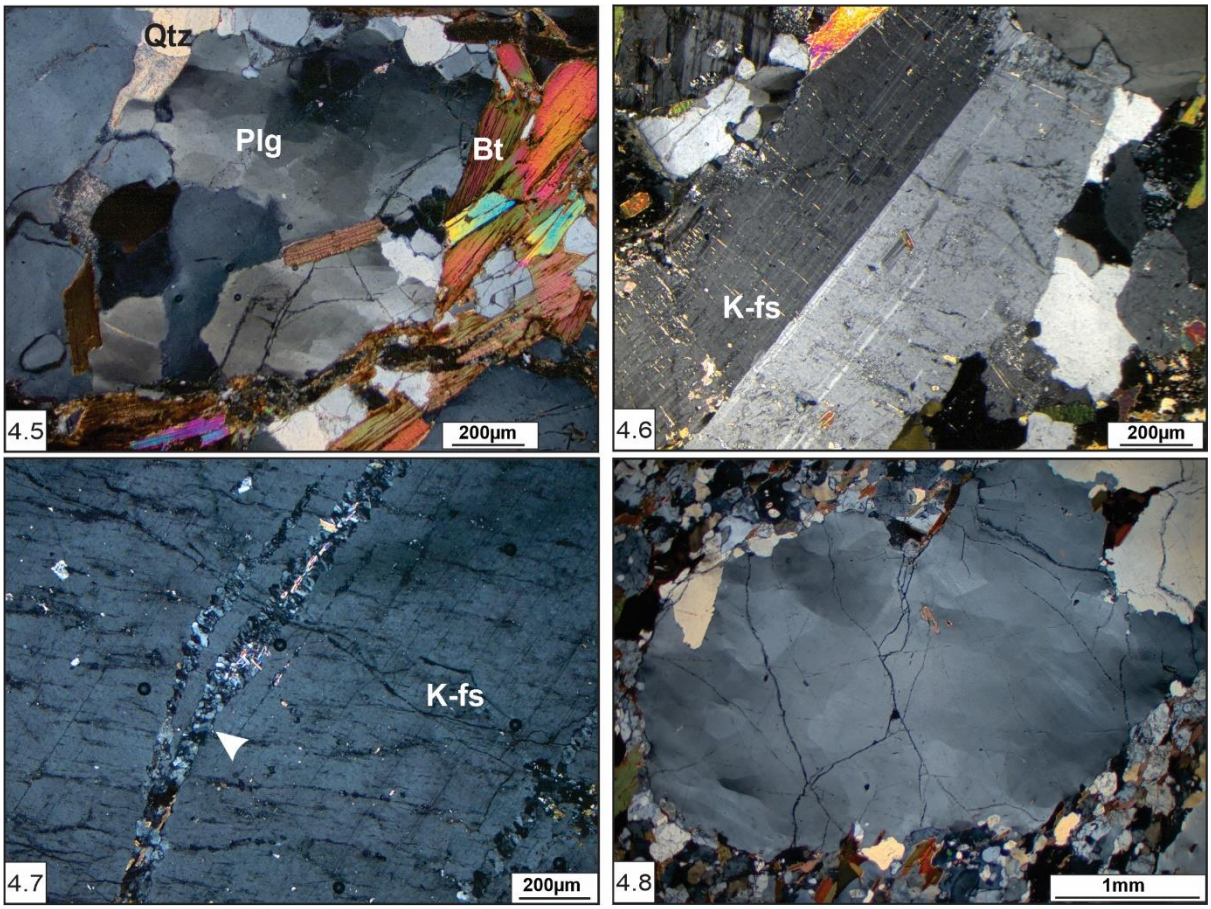

Figure 4.5-4.8: Photomicrographs of Phulad granite in cross polarized light showing (4.5) interlocking texture in between K-feldspar, plagioclase, quartz, and biotite, (4.6) elongated alkali feldspar phenocryst that is sub-parallel to the foliation shows simple twinning, (4.7) submagmatic fractures in K-feldspar phenocrysts has been filled by fine-aggregates of quartz and feldspar marked with arrow head, (4.8) undulatory extinction in large K-feldspar crystals. Plg- Plagioclase, Qtz- Quartz, K-fs- K-feldspar, Bt-Biotite.

microcline twinning in the more deformed rocks (Figure 4.9). Under transmitted light microscope, recrystallized quartz grains have been found (Figure 4.10). Flame perthite mostly

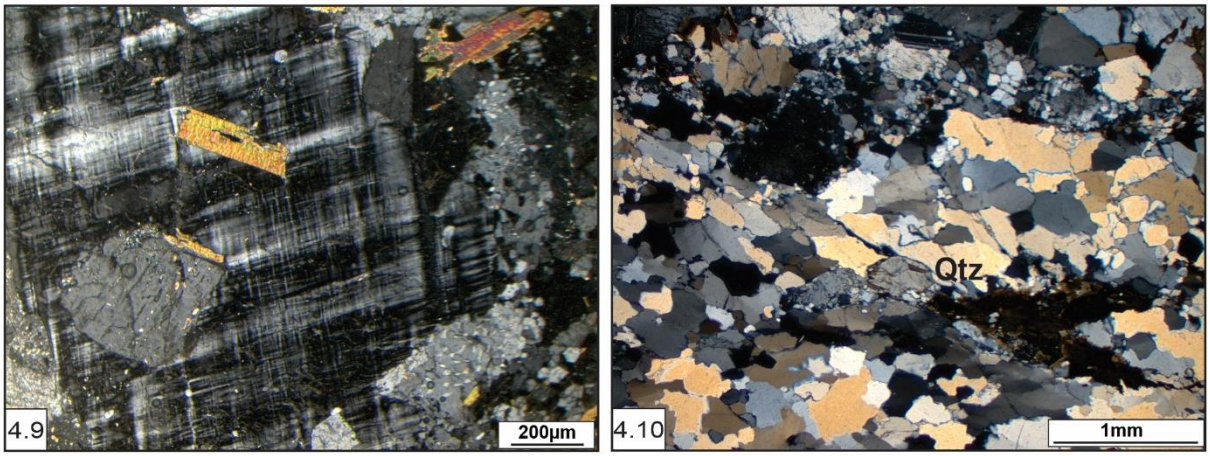

Figure 4.9-4.10: Photomicrographs of Phulad granite in cross polarized light showing (4.9) microcline twinning, (4.10) recrystallised quartz grains. Qtz- Quartz.

occurs in K-feldspar grains with a fine, lenticular shaped parallel lamallae and its orientation trends are nearly similar to the host lattice of K-feldspar grain (Figure 4.11). BSE (Back Scattered Electron) microscopic image is also showing flame perthite with a white arrowhead (Figure 4.12) in euhedral shaped K-feldspar megacrysts with a sharp boundary. Myrmekite is

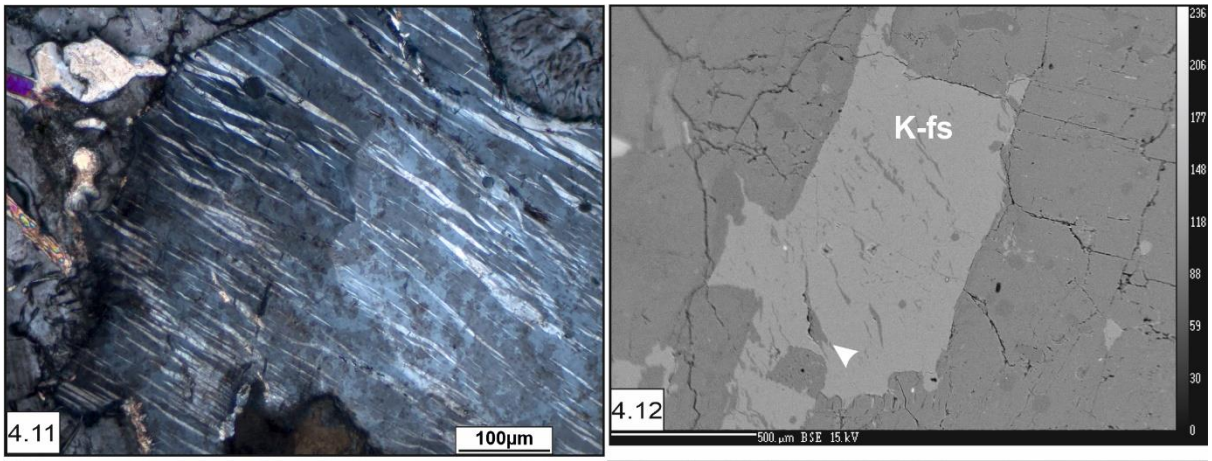

Figure 4.11-4.12: Photomicrograph of Phulad granite in cross polarized light showing (4.11) flame perthite in K-feldspar grains, (4.12) BSE image showing flame perthite with white arrow head. K-fs- K-feldspar.

commonly found in deformed felsic rock, where it replaces the margin of K-feldspar grain. Under a transmitted light microscope myrmekite was found at the boundary of the large K-feldspar grain (Figure 4.13). Inclusions in megacrysts are significantly smaller than grains of the same minerals found in the surrounding rocks. Small inclusions of euhedral shaped

plagioclase showing with white arrowhead (Figure 4.14), quartz and micaceous minerals (Figure 4.9) are present in K-feldspar megacrysts. And some of those minerals present as the

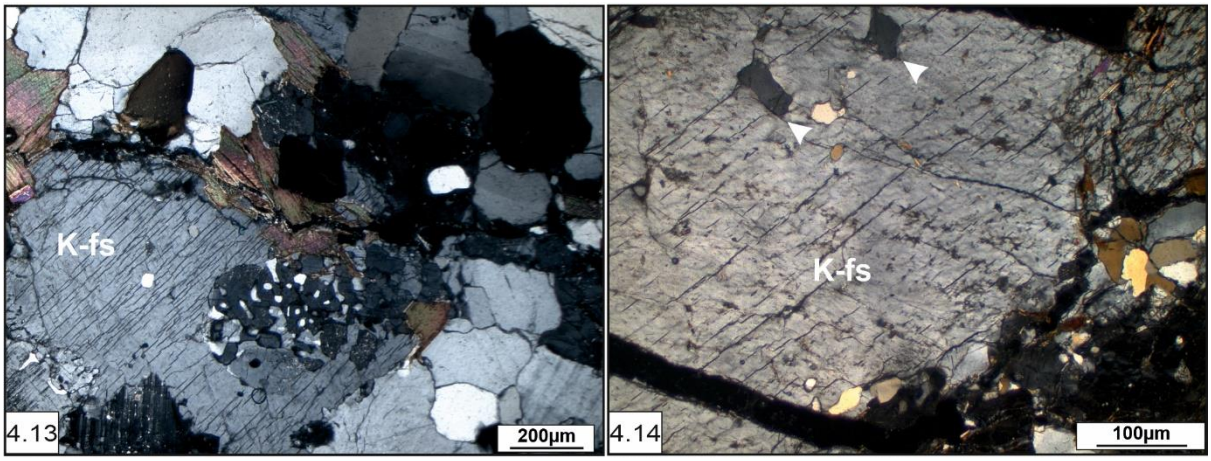

Figure 4.13-4.14: Photomicrographs of Phulad granite in cross polarized light showing (4.13) myrmekite at the boundary of the large K-feldspar grain, (4.14) inclusions of euhedral shaped plagioclase in K-feldspar. K-fs- K-feldspar.

inclusions are also associated with the K-feldspar grain boundary (Figure 4.15). Large augen shaped K-feldspar megacrysts were found with extensive marginal recrystallization/ neorecrystallization of quartz and feldspar aggregates (Figure 4.16). Large K-feldspar grain

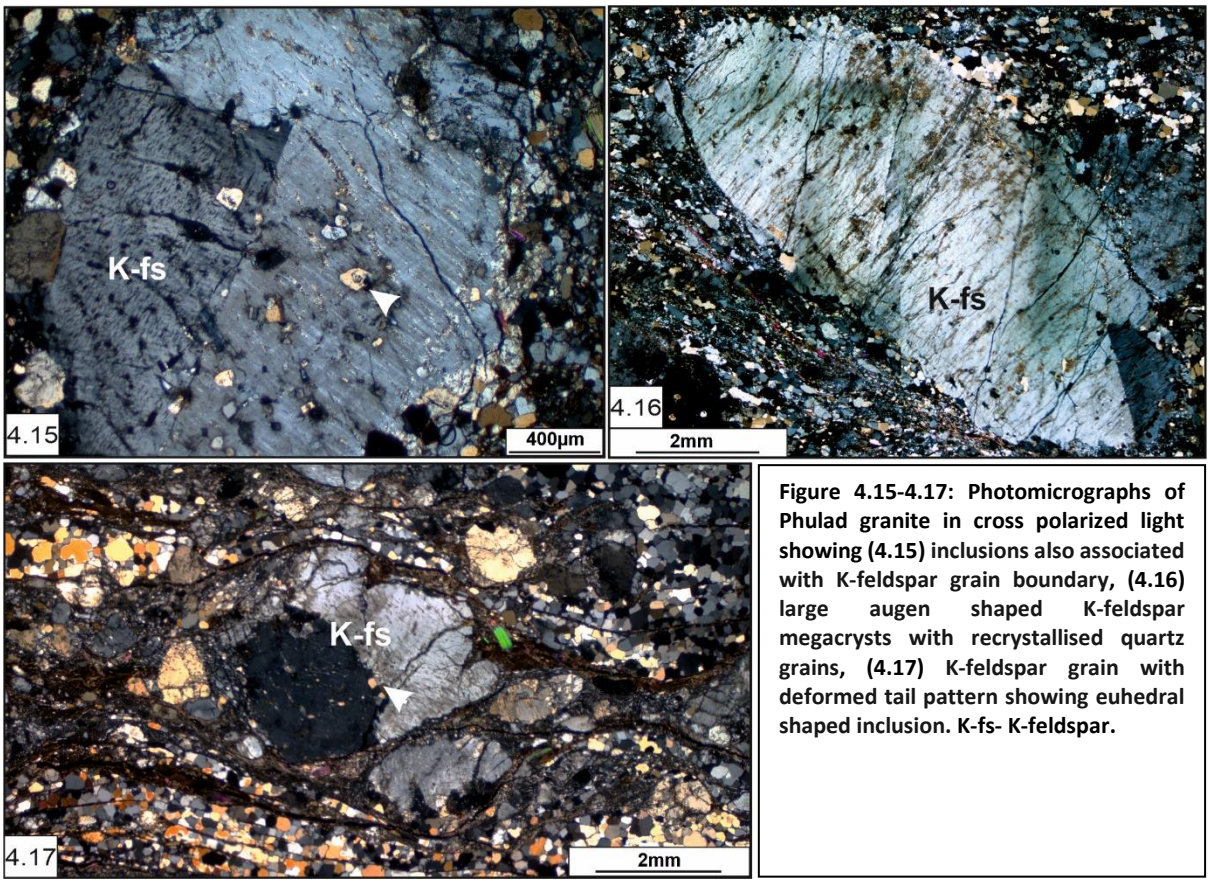

Figure 4.15-4.17: Photomicrographs of Phulad granite in cross polarized light showing (4.15) inclusions also associated with K-feldspar grain boundary, (4.16) large augen shaped K-feldspar megacrysts with recrystallised quartz grains, (4.17) K-feldspar grain with deformed tail pattern showing euhedral shaped inclusion. K-fs- K-feldspar.

with deformed tail pattern showing euhedral shaped inclusion (Figure 4.17).

4.4 BaO Content in K-feldspar Phenocrysts and Matrix K-feldspar:

The geochemical behaviour of barium is commonly allied to potassium because of the similarity of the Ba^{++} and K^{+} ionic radii. The K-group elements are notably enriched in alkaline igneous rocks, whether formed along plate margins or from intraplate magmatic activity (e.g., Baker et al. 1977; White, 1979; Whitford and Jezek, 1979). In some instances, such as recorded in granites, barium concentration in K-feldspar phenocrysts varies by more than an order of magnitude, from 0.15 wt.% BaO to 2.14 wt.% BaO (Němec, 1975; Kuryvial, 1976), although these K-feldspars have a rather constant composition for major elements (Long and Luth, 1979). Here in these K-feldspar megacrysts, BaO is not varying significantly from core to intermediate to rim. But there is a variation of BaO content between matrix K-feldspar and megacrysts. K-feldspar megacrysts show a higher value of BaO wt.% than the K-feldspars situated in the matrix. Data is provided in table 4.1. The Ba content of K-feldspar megacrysts is commonly higher than that of K-feldspar in the matrix (Emmermann, 1968; Kerrick, 1969; Kuryvial, 1976; Higgins and Kawachi, 1977; Kawachi and Sato, 1978) suggesting earlier crystallization of the megacrysts, on the basis of (1) theoretical considerations of atomic structure, (2) compositions of phenocryst and groundmass K-feldspars in volcanic and plutonic rocks (Heier and Taylor, 1959; Taylor et al., 1960; Berlin and Henderson, 1969), as discussed by Kawachi and Sato (1978), and (3) experimental determination of the partition coefficient for Ba between K-feldspar and silicate melt (Pierozynski and Henderson, 1978; Guo and Green, 1989).

Table 4.1: Electron microprobe data of K-feldspar phenocrysts and matrix K-feldspar.

Remarks	K-feldspar Phenocryst										Matrix K-feldspar							
oxides	wt.% of oxides										wt.% of oxides							
SiO_2	64.09	64.28	63.86	64.02	63.72	63.41	64.15	64.37	64.42	64.22	63.72	64.31	64.06	64.17	64.63	64.38	64.41	64.15
TiO_2	0.02	0.00	0.02	0.01	0.00	0.00	0.00	0.01	0.04	0.02	0.00	0.00	0.03	0.00	0.03	0.00	0.03	0.01
Al_2O_3	18.32	18.16	18.43	18.20	17.88	18.01	18.26	18.16	18.18	18.27	17.88	18.29	18.13	18.27	18.13	18.32	18.19	18.08
Cr_2O_3	0.00	0.01	0.00	0.02	0.06	0.01	0.00	0.00	0.00	0.02	0.00	0.02	0.00	0.00	0.06	0.00	0.00	0.03
FeO	0.05	0.00	0.03	0.05	0.02	0.03	0.00	0.00	0.02	0.02	0.01	0.02	0.02	0.00	0.02	0.00	0.00	0.10
MnO	0.01	0.00	0.01	0.00	0.01	0.00	0.01	0.03	0.00	0.00	0.01	0.00	0.00	0.00	0.01	0.00	0.03	0.00
NiO	0.00	0.00	0.00	0.03	0.01	0.00	0.04	0.01	0.00	0.07	0.02	0.00	0.01	0.03	0.02	0.02	0.02	0.01
MgO	0.00	0.00	0.00	0.00	0.00	0.00	0.00	0.00	0.00	0.00	0.00	0.00	0.00	0.00	0.00	0.00	0.00	0.00
CaO	0.04	0.01	0.02	0.03	0.01	0.06	0.00	0.00	0.02	0.01	0.00	0.00	0.00	0.00	0.02	0.02	0.00	0.04
BaO	0.14	0.17	0.24	0.12	0.09	0.15	0.26	0.12	0.13	0.13	0.06	0.07	0.07	0.08	0.02	0.03	0.08	0.06
Na_2O	0.60	1.06	0.63	0.52	0.37	0.47	0.45	0.47	0.68	0.94	0.41	0.63	0.55	0.61	0.47	0.65	0.63	0.73
K_2O	15.95	15.33	16.16	16.08	16.24	16.11	16.19	16.34	16.03	15.49	16.25	15.82	16.24	16.16	16.43	15.92	16.07	15.95
P_2O_5	0.00	0.00	0.00	0.00	0.00	0.00	0.00	0.00	0.00	0.00	0.00	0.00	0.00	0.00	0.00	0.00	0.00	0.00
Total	99.22	99.02	99.41	99.08	98.40	98.25	99.36	99.51	99.52	99.19	98.36	99.16	99.09	99.31	99.85	99.33	99.47	99.16
Oxygen basis	8	8	8	8	8	8	8	8	8	8	8	8	8	8	8	8	8	8
Cations	no. of cation on basis of oxygen										no. of cation on basis of oxygen							
Si^{4+}	2.989	2.997	2.980	2.992	3.000	2.991	2.992	2.997	2.996	2.992	3.001	2.996	2.994	2.992	2.998	2.995	2.996	2.995
Ti^{4+}	0.001	0.000	0.001	0.000	0.000	0.000	0.000	0.000	0.001	0.001	0.000	0.000	0.001	0.000	0.001	0.000	0.001	0.000
Al^{3+}	1.007	0.998	1.014	1.003	0.992	1.002	1.004	0.997	0.997	1.003	0.993	1.004	0.999	1.004	0.992	1.005	0.998	0.995
Cr^{3+}	0.000	0.000	0.000	0.001	0.002	0.000	0.000	0.000	0.000	0.001	0.000	0.001	0.000	0.000	0.002	0.000	0.000	0.001
Fe^{2+}	0.002	0.000	0.001	0.002	0.001	0.001	0.000	0.000	0.001	0.001	0.000	0.001	0.001	0.000	0.001	0.000	0.000	0.004
Mn^{2+}	0.000	0.000	0.001	0.000	0.000	0.000	0.000	0.001	0.000	0.000	0.001	0.000	0.000	0.000	0.000	0.000	0.001	0.000
Ni^{2+}	0.000	0.000	0.000	0.001	0.000	0.000	0.001	0.000	0.000	0.003	0.001	0.000	0.000	0.001	0.001	0.001	0.001	0.000
Mg^{2+}	0.000	0.000	0.000	0.000	0.000	0.000	0.000	0.000	0.000	0.000	0.000	0.000	0.000	0.000	0.000	0.000	0.000	0.000
Ca^{2+}	0.002	0.001	0.001	0.001	0.000	0.003	0.000	0.000	0.001	0.000	0.000	0.000	0.000	0.000	0.001	0.001	0.000	0.002
Ba^{2+}	0.002	0.003	0.004	0.002	0.002	0.003	0.005	0.002	0.002	0.002	0.001	0.001	0.001	0.001	0.000	0.001	0.001	0.001
Na^{+}	0.055	0.096	0.057	0.047	0.034	0.043	0.041	0.042	0.062	0.085	0.037	0.056	0.050	0.055	0.042	0.059	0.057	0.066
K^{+}	0.949	0.912	0.962	0.959	0.976	0.970	0.963	0.971	0.951	0.921	0.976	0.940	0.968	0.961	0.973	0.945	0.954	0.950
P^{5+}	0.000	0.000	0.000	0.000	0.000	0.000	0.000	0.000	0.000	0.000	0.000	0.000	0.000	0.000	0.000	0.000	0.000	0.000
Total	5.008	5.007	5.021	5.009	5.008	5.014	5.008	5.011	5.011	5.008	5.010	5.000	5.014	5.015	5.011	5.004	5.009	5.015
XAb	0.05	0.09	0.06	0.05	0.03	0.04	0.04	0.04	0.06	0.08	0.04	0.06	0.05	0.05	0.04	0.06	0.06	0.06
XOr	0.94	0.90	0.94	0.95	0.97	0.95	0.96	0.96	0.94	0.91	0.96	0.94	0.95	0.95	0.96	0.94	0.94	0.93
XAn	0.00	0.00	0.00	0.00	0.00	0.00	0.00	0.00	0.00	0.00	0.00	0.00	0.00	0.00	0.00	0.00	0.00	0.00

4.5 Summary:

4.5.1 Evidence related to the magmatic origin of the K-feldspar megacrysts in Phulad granite:

The following points of evidence indicate that the K-feldspar megacrysts are of igneous origin.

1) Presence of parallel to sub-parallel alignment of euhedral shaped K-feldspar megacrysts in Phulad granite indicates that the crystallization process occurred before the deformation event (Figures 4.1, 4.4). According to Paterson et al. (1989), aligned elongate crystals of K-feldspar indicate igneous precursor. Crystals may become aligned at any stage of magmatic evolution, but the system needs to be sufficiently viscous (Paterson et al., 1998), otherwise the alignment can easily be destroyed by the later deformation event(s) (Peterson et al., 1998). Also, the K-feldspar megacrysts show planar crystal faces (Figure 4.4), which indicate the porphyritic nature of the granite (Vernon and Paterson, 2002).

2) Some of the K-feldspar crystals exhibit simple twinning (Figure 4.6). Simple twinning is directly related to the magmatic origin of the K-feldspar megacrysts, as simple twinning is very common in K-feldspar megacrysts of granitoid rocks (Vernon, 1986). And the simple twinning of K-feldspar indicates an early crystallization process with the presence of enough melt in the surroundings (Vernon, 1986, 1999).

3) Small euhedral shaped inclusions of plagioclase, quartz and micaceous minerals have been observed in many megacrysts (Figures 4.9, 4.14, 4.15). The megacrystic inclusions are significantly smaller than the grains of the same minerals found in the surrounding megacrysts. This euhedral shaped plagioclase and biotite inclusions are common in K-feldspar phenocrysts (Vernon, 1986). Inclusions in the megacrysts are much smaller than grains of the same minerals in the surrounding rock (Kerrick, 1969; Higgins and Kawachi, 1977; Kawachi and Sato, 1978) suggesting they were incorporated relatively early in the magma's

crystallization history, whereas groundmass grains continued to grow (Higgins and Kawachi, 1977). In metamorphic minerals, inclusions of quartz and plagioclase tend to be spherical in nature or have a curved corner (Kretz, 1966; Vernon 1968, 1976). So, the K-feldspar megacrysts that are present here are of purely magmatic origin, not metamorphic.

4) Firstly, the Phulad granite in which K-feldspar megacrysts are not in contact with each other are weakly deformed and shows parallel alignment with the magmatic foliation (Figure 4.1). Secondly, the Phulad granites with closely spaced magmatic K-feldspar megacrysts show parallel alignment with the tectonic foliation (Figure 4.2). These two cases suggest that close to the shear zone, the granitic body gets more deformed and for the pre-existing stress, magmatic fluid squished out from the granite. And this deformational event occurred after the formation of large K-feldspar megacrysts in the system. Also, K-feldspar megacrysts do not grow into each other even when they are closely aggregated near the pegmatitic body, supporting the magmatic origin of the megacryst. As synchronous in situ growth of megacrysts would cause the megacrysts to grow into each other in the solidus stage.

5) Higher barium content in K-feldspar megacrysts than the K-feldspar in matrix suggests that the megacrysts are the product of early crystallization.

4.5.2 Evidence related to the solid-state deformation:

The following microstructural evidence indicate solid-state deformation after the formation of the K-feldspar megacrysts in Phulad granite.

1) Undulose extinction is common in feldspar (present in the groundmass) in Phulad granite (Figure 4.8). Such kind of extinction only happens when a crystal undergoes deformation (mainly crustal deformation) even after its formation. The deformation can lead to dislocation in the crystal lattice and sub-grain boundary formation.

2) Microcline twinning in K-feldspar megacrysts is associated with solid-state deformation and generally found in more deformed rocks (Eggleton et al., 1979; Eggleton and Buseck, 1980; Bell and Jhonson, 1989; Dickson, 1996). In Phulad granite, megacrysts show stronger intensity of microcline twinning (Figure 4.9). Gerald and McLaren (1982) experimentally observed that such kind of twinning can only occur under a specific stress condition. Microcline is abundant in the groundmass, it never occurs as inclusions in the megacrysts, which suggests a porphyroclasts origin for the megacrysts, according to Shand (1949). However, it is arguable that, even if their orientations were different, microcline inclusions would possibly be incorporated, without a trace, in the microcline megacryst.

3) Recrystallization of grains is a primary feature of solid-state deformation (Hobbs et al., 1976; Vernon, 1976; Paterson et al., 1989). An enormous amount of recrystallized quartz grains has been found in the studied rock samples (Figure 4.10). It is a process which is functioned by strain accumulation and rise in temperature and mainly occurs due to the recrystallization of mineral grains under solid-state deformation, which is a typical feature of coarse-grained rock like granite (Vernon et al., 1983).

4) Flame perthite is a typical feature of alkali feldspar that has experienced solid-state deformation (Pryer and Robin, 1995, 1996). In Phulad granite, flame perthite is present with a fine, lenticular shaped parallel lamellae and its orientation trend is nearly similar to the host lattice of K-feldspar grain (Figures 4.11, 4.12).

5) The formation of myrmekite is associated with complex reactions and also requires transport of chemical components in fluid from one part to another part of the rock (Simpsons and Wintsch, 1989). Here in Phulad granite, a sufficient amount of myrmekites is found to be projecting towards the K-feldspar crystals from the matrix (Figure 4.13), providing a means

for the solid-state deformation (Vernon et al., 1983; Paterson et al., 1989; Simpson and Wintsch, 1989; Vernon, 1990, 1991).

6) Fine grained recrystallized aggregates of quartz have been found and mainly occurred marginally along the augen shaped K-feldspar grain boundary (Figure 4.16) under solid state deformation, which is a typical feature of coarse-grained rock, like granite (Vernon et al., 1983).

7) Euhedral shaped mineral grain inclusion in deformed K-feldspar megacryst (with tail pattern) (Figure 4.17) signifying that solid state deformation imprinted over magmatic foliation and also suggesting the magmatic origin of the megacrysts.

These features are present in both the varieties of Phulad granites, i.e., large K-feldspar grains are not in contact and are closely spaced. There is no such difference under a microscope except in the mesoscopic scale.

The present study shows some evidence such as the large euhedral shape of K-feldspar having planar crystal faces and preferably aligned. Microstructural features such as simple twinning, inclusions in phenocrysts, marginal recrystallization and neocrystallization, recrystallization of quartz, microcline twinning, undulose extinction in K-feldspar, presence of myrmekite, flame perthite, formation of subgrains in K-feldspar are well indicator to suggest that the K-feldspar megacrysts in deformed Phulad granite are of igneous origin. Evidence of metamorphic origin, such as porphyroblastic growth and inclusion tails, was absent.

Chapter 5

Whole-rock Geochemistry

5.1 Introduction:

Phulad granite is a typical porphyritic granite associated with huge pegmatites in some places. In the present work the geochemical behaviour of this Phulad granite is described. 8(eight) rock samples were collected from the least deformed variety of Phulad granite and 4(four) samples from deformed variety. The eight samples were used for geochemical analysis and the other four were used to calculate volume change and mass balance calculation. Major elements, minor elements, trace elements and REE (Rare Earth Element) data were obtained from XRF and ICP-MS at the ACME Laboratory, Canada. The analytical data are presented in table 5.1. This geochemical data has been used to classify the rock and to constrain their possible tectonic settings. The data obtained were plotted using the geochemical data tool kit 3.15 (GCDKit).

5.2 Sample Preparation and Analytical Technique:

Twelve granitic samples (shown in the map, Figure 5.1) were collected from the outcrops of Phulad granite and analyzed for whole rock characterization. Fresh samples weighing more than 5 kg were crushed in a tungsten carbide jaw crusher. Rocks samples were dried in between 60°C – 100°C temperature. After cone and quartering, representative portions were powdered in an agate ball mill to less than 600µm. In ACME Laboratory, Canada, samples were prepared for XRF and ICP-MS analysis. Samples were digested by Lithium metaborate/tetraborate fusion and mixed with $LiBO_2/Li_2B_4O_7$ flux. After the partial digestion method, samples were frequently referred to as leaches. Partial digestions may be weak,

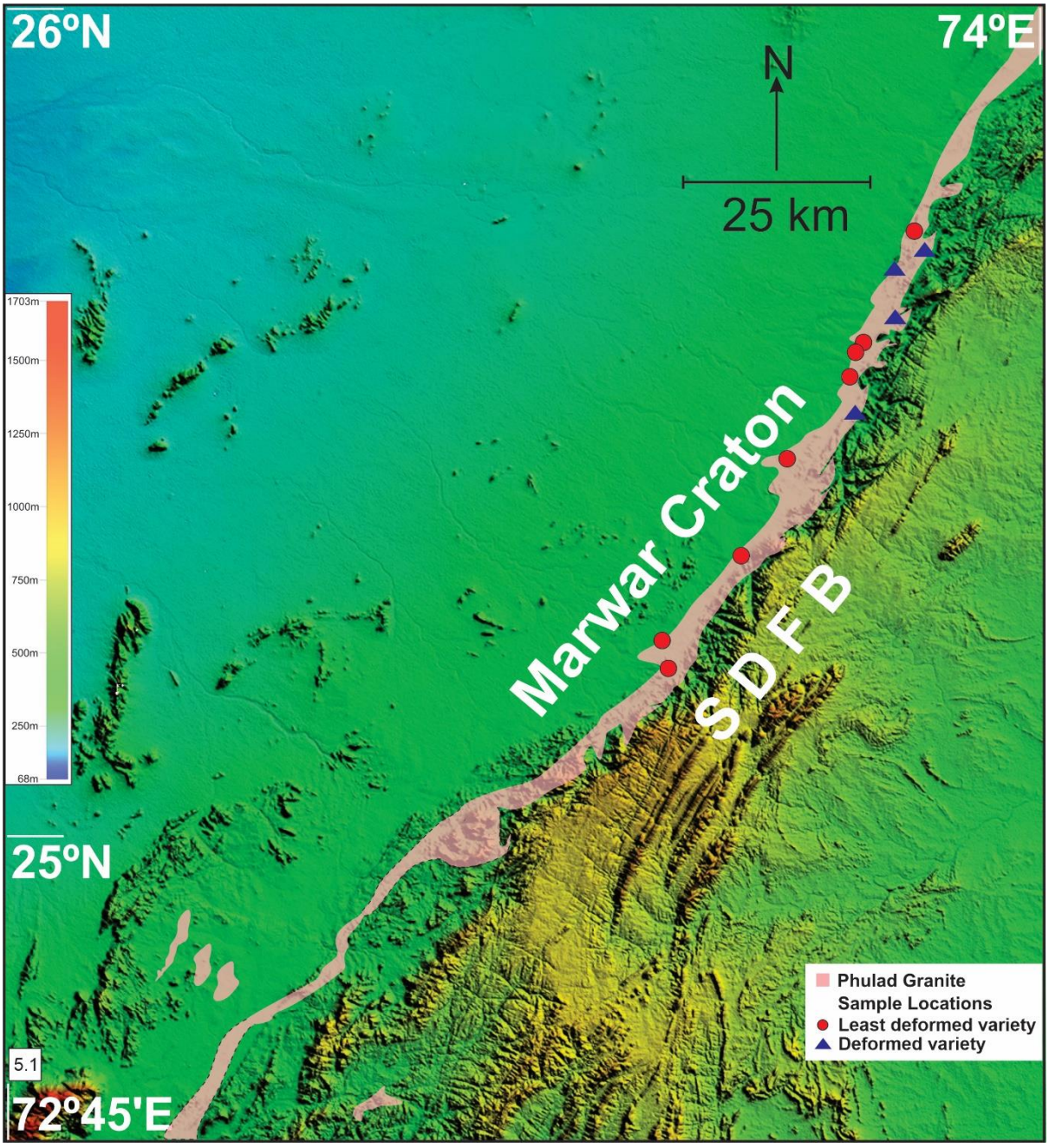

Figure 5.1: Digital Elevation Model (DEM) map with the outline of Phulad granite along the contact of Marwar Craton and SDFB. Red dots and blue triangles are the sample locations of least deformed and deformed variety of Phulad granite respectively. DEM is prepared from the SRTM data of USGS earth explorer.

moderate, or strong in their attack, and it may be selective (attacking only one mineral substrate) or non-selective (attacking all mineral substrates) in nature. Choosing the Partial Digestion because of knowing the mode of occurrence of an analyte can provide information on the source and the means of transport. Partial digestion can increase the contrast between anomalous and background values. For partial digestion generally used water and aqua regia.

Table 5.1: Major element (wt.%), trace and REE's (PPM) data for Phulad granite.

		Least deformed variety								Deformed variety			
Sample No.		P-647a	P-647b	P-648a	P-462	P-439	P-653	P-753	P-758	P-661	P-662	P-663b	P-659a
SiO_2	%	72.69	73.25	72.59	73.43	71.51	72.9	76.63	66.08	77.34	72.59	74.71	72.68
Al_2O_3	%	13.53	12.92	13.46	13.58	13.57	13.68	11.82	14.95	12.18	13.29	13.03	14.25
Fe_2O_3	%	2.4	2.48	3.6	1.56	3.67	2.29	2.58	4.91	0.82	3.96	2.74	2
MgO	%	0.42	0.5	0.65	0.33	0.9	0.37	0.39	1.2	0.07	0.55	0.31	0.51
CaO	%	1.41	1.74	1.38	0.97	2.07	0.89	0.63	3.17	0.74	1.97	1.68	1.95
Na_2O	%	2.96	2.94	3.41	2.42	2.47	2.88	2.01	3	3.9	4.41	4.4	3.72
K_2O	%	5.13	4.63	2.38	5.93	3.76	5.33	3.88	4.24	3.94	1.27	1.63	2.25
TiO_2	%	0.29	0.31	0.44	0.18	0.51	0.25	0.23	0.92	0.09	0.35	0.24	0.23
P_2O_5	%	0.08	0.1	0.14	0.08	0.12	0.11	0.15	0.24	<0.01	0.06	0.05	0.1
MnO	%	0.04	0.04	0.05	0.02	0.05	0.05	0.03	0.07	0.02	0.05	0.06	0.03
Cr_2O_3	%	<0.002	<0.002	0.003	0.002	0.003	<0.002	<0.002	<0.002	<0.002	<0.002	<0.002	<0.002
LOI	%	0.8	0.9	1.7	1.3	1.1	1	1.4	0.9	0.7	1.3	0.9	2.1
Sum	%	99.81	99.85	99.78	99.83	99.79	99.8	99.8	99.8	99.8	99.86	99.82	99.85
Ba	PPM	292	274	86	341	362	309	101	776	378	182	275	405
Ni	PPM	<20	<20	<20	<20	<20	<20	<20	<20	<20	<20	<20	<20
Sc	PPM	5	5	7	4	8	5	4	10	3	8	6	5
Be	PPM	<1	<1	3	<1	<1	1	2	2	4	<1	2	3
Co	PPM	72.9	53.2	75.3	92	86.9	89.9	92.6	57	86.5	55.8	91.4	79.4
Cs	PPM	25.6	16.4	39.4	7.6	13.1	27.4	13	7.1	2.2	2	3.2	8
Ga	PPM	16	15	18	15	14.9	15.7	16.6	18.8	22.4	17.7	19.6	13.9
Hf	PPM	5.4	4.6	6.5	3.3	5.9	4.5	5	7.2	9.4	7	7.7	3.3
Nb	PPM	10.6	12.1	12.8	8.4	11.8	10.4	13	16.3	27.7	4.8	6.1	7
Rb	PPM	293.5	267.2	243.4	231.3	203.3	315.8	277.9	199.4	171.9	54.2	64.8	103.1
Sn	PPM	9	9	11	5	4	9	13	3	4	4	3	3
Sr	PPM	51.6	46	34.6	45	72.4	43.6	23.3	201.7	105	62.9	56	112.6
Ta	PPM	1.5	1.4	1.4	2.3	2.4	2.6	4.7	1.7	3.6	0.6	2.1	2
Th	PPM	31.2	27.1	44.9	22.2	34	28.8	32.7	14.3	18.3	5	5.6	15.4
U	PPM	3.9	3.3	3.5	1.8	3.1	3.1	3.7	2.7	1.7	0.5	0.5	1.3
V	PPM	20	21	43	15	42	19	14	56	<8	22	8	30
W	PPM	528.4	382.8	694.1	702.3	655.9	775.6	740.3	400.9	669.4	407.4	726.8	560.5
Zr	PPM	180.9	148	197.3	99.7	199.9	143.3	150	273.9	185	201.8	221	117.3
Y	PPM	36.2	35.6	50.4	28	36.9	32.2	37.2	25.4	97	89	82.3	16.7
La	PPM	35.8	28.6	53.5	23.1	47.8	20.9	27.2	44.4	39.8	11.7	18.8	13.1
Ce	PPM	68.8	60.8	95	53.1	91.6	60.2	63.8	84	82.9	41	42.6	37.4
Pr	PPM	7.61	6.67	10.86	5.45	10.35	4.85	6.44	9.43	10.76	4.78	6.49	3.02
Nd	PPM	26.8	25.1	39.4	20.6	38.9	17.9	24	35.2	44.6	23	29.5	11.1
Sm	PPM	5.49	5.28	8.03	4.32	7.76	3.93	5.68	6.73	11.74	6.95	8.65	2.5
Eu	PPM	0.69	0.57	0.51	0.48	1.09	0.51	0.28	1.6	1.36	1.03	1.08	0.49
Gd	PPM	5.97	5.55	8.13	4.34	7.25	4.21	5.9	6.37	13.56	9.53	10.79	2.48
Tb	PPM	1.07	1	1.38	0.78	1.17	0.83	1.15	0.93	2.5	1.94	2.11	0.46
Dy	PPM	6.84	6.05	8.04	4.88	6.79	5.53	7.27	5.27	16.58	13.47	13.93	3
Ho	PPM	1.41	1.25	1.67	0.93	1.39	1.22	1.28	0.96	3.77	3.22	3.05	0.62
Er	PPM	3.87	3.8	4.83	2.76	3.92	3.72	3.22	2.69	11.47	10.79	9.82	1.92

Table 5.1: Continued

Sample No.		Least deformed variety								Deformed varity			
		P-647a	P-647b	P-648a	P-462	P-439	P-653	P-753	P-758	P-661	P-662	P-663b	P-659a
Tm	PPM	0.53	0.56	0.72	0.4	0.54	0.53	0.41	0.36	1.91	1.59	1.44	0.24
Yb	PPM	3.73	3.31	4.23	2.47	3.47	3.4	2.35	2.32	13.22	10.74	9.28	1.68
Lu	PPM	0.53	0.48	0.63	0.36	0.5	0.47	0.32	0.33	1.99	1.66	1.42	0.25
Mo	PPM	0.2	0.5	0.3	0.2	0.5	0.3	0.5	0.5	0.3	0.7	0.2	0.1
Cu	PPM	3.1	7.1	31.5	4.9	9.8	4.4	1.1	8.8	4.8	0.9	1.1	1.3
Pb	PPM	8.2	5.5	5	7.3	4.2	7.2	10.5	5.3	5.9	1.1	2.7	11.4
Zn	PPM	33	37	68	29	51	42	40	72	49	34	65	25
Ni	PPM	2.5	3.4	5.1	3.4	9.4	5.1	3.3	5.6	1.8	2.4	2	5.2
As	PPM	1.3	0.9	0.8	<0.5	<0.5	2.4	70.4	<0.5	<0.5	<0.5	<0.5	1.3
Cd	PPM	<0.1	<0.1	<0.1	<0.1	<0.1	<0.1	<0.1	<0.1	<0.1	<0.1	<0.1	<0.1
Sb	PPM	0.4	0.2	<0.1	<0.1	<0.1	<0.1	<0.1	<0.1	<0.1	<0.1	<0.1	<0.1
Bi	PPM	0.1	<0.1	2	0.2	0.4	0.3	5	0.2	<0.1	<0.1	<0.1	0.1
Ag	PPM	<0.1	<0.1	<0.1	<0.1	<0.1	<0.1	<0.1	<0.1	<0.1	<0.1	<0.1	<0.1
Au	PPB	<0.5	<0.5	<0.5	<0.5	<0.5	<0.5	0.6	<0.5	<0.5	<0.5	0.6	1.4
Hg	PPM	<0.01	<0.01	<0.01	<0.01	<0.01	<0.01	<0.01	<0.01	<0.01	<0.01	<0.01	<0.01
Tl	PPM	0.6	0.7	1	0.3	0.6	0.6	0.7	0.7	0.2	0.2	0.3	0.2
Se	PPM	<0.5	<0.5	<0.5	<0.5	<0.5	<0.5	<0.5	<0.5	<0.5	<0.5	0.5	<0.5

Water is a weak and selective leach conducted at room temperature to dissolve only water-soluble compounds like salts and aqua Regia is a strong mineral acid (HCl + HNO_3) leach conducted at 95°C liberating elements in salts, exchange sites, carbonates, oxides, hydroxides, sulphides, etc. Aqua Regia was added to 0.5 g sample aliquots in test tubes before being added to a hot-water bath to improve digestion. Furthermore, total decomposition chooses to report the absolute abundance of an element or compound within the sample. In total digestion, generally use 4-Acid digestion (Geochemical digestion) with nitric, perchloric and hydrofluoric acids heated until dryness to decompose most minerals (including silicates) to metal salts that are then back leached into either Aqua Regia or concentrated HCl. Lastly use the ICP-MS for measured the weight percent of major and minor element and trace element value. Loss on ignition (LOI) is determined by igniting a sample split then measuring the weight loss. Total Carbon and Sulphur may be included and is determined by the Leco method based on the detection of atoms striking a target the solutions aspirated into a plasma operating at 800°C create charged ions. Pure solutions of known concentrations of the analytes are aspirated into the instrument to calibrate the results. Sample Analysis is by an Elan 6000 ICP Mass Spec. For the Anglo Option, 51 elements are determined comprising: Au.

Ag, Al, As, Ba. Be, Bi, C, Ca, Cd, Co, Cr, Cs, Cu, Fe, Ga, Hf, Hg, Si, Sn, Sr, Ta, Th, Ti, Tl, U, V, W, Zn and Zr. Other optional K, Mg, Mn, Mo, Na, Nb, Ni, P, Pb, Rb, S, Sb and Sc, Y, La, Ce, Pr, Nd, Sm, Eu, Gd, Tb, Dy, Ho, Er, Tm, Yb, Lu elements include the REE suite. Sample volumes of other elements subject to the nugget effect are of importance.

5.3 Major Element Geochemistry:

All samples show similar abundances with high SiO_2 = 72.4 wt.%; Fe_2O_3t 2.9 wt.%; Al_2O_3= 13.4 wt.%; low MgO= 0.6 wt.%; Na_2O= 2.7 wt.%; K_2O = 4.4 wt.%; and CaO= 1.5 wt.%. The eight samples have overall a fairly uniform granitic composition. The total Alkali vs Silica (TAS) (Na_2O+K_2O vs SiO_2) plot of Middlemost (1994) (Figure 5.2) confirms this with one sample falls in granodiorite portion in the igneous rock classification. De la Roche et al. (1980) proposed a bivariate graph (Figure 5.3) based upon the cation proportions expressed in millications which is useful for both volcanic and plutonic rocks. In this bivariate plot, the x axis is defined by R_1= [4Si -11(Na+K)–2(Fe +Ti)] and the y axis is defined by R_2=(Al + 2Mg + 6Ca). The advantage of

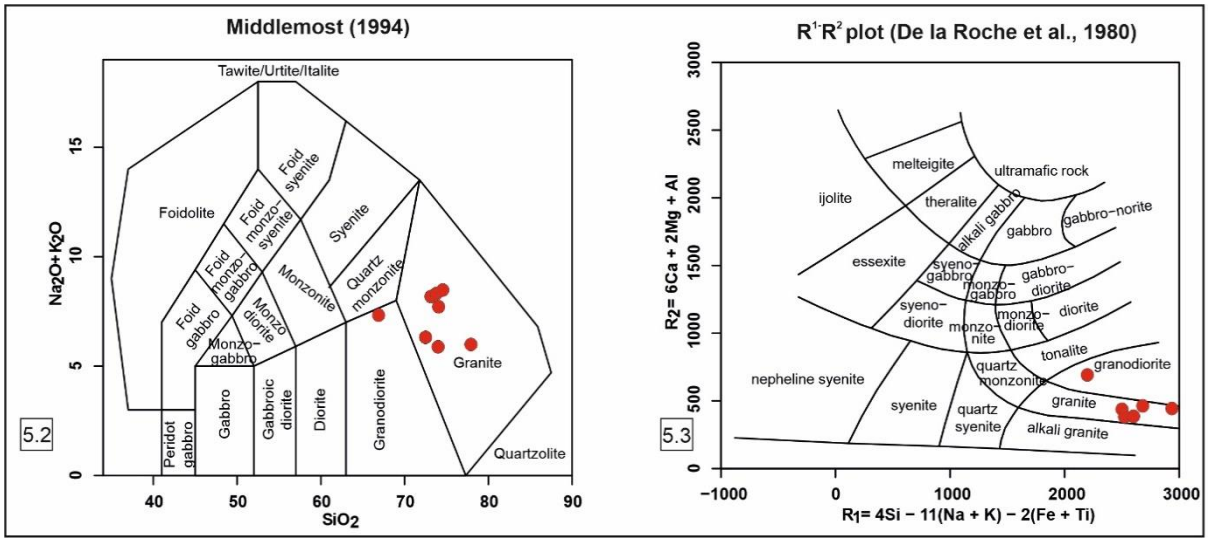

Figure 5.2-5.3: Total Alkali (Na_2O+K_2O) vs Silica (SiO_2) diagram (Middlemost, 1994) (5.2) for Phulad granite samples show dominantly granitic composition. Bivariate graph of De la Roche et al. (1980) (5.3) confirms the granitic composition.

this classification is that the entire major element chemistry of the rock is used and can be applied to all types of igneous rocks. The mineral composition can also be plotted in this diagram allowing a broad comparison between modal and chemical compositions. On plotting the rock in this graph, it falls in the granite field confirming the rock nomenclature. The Phulad granite shows characteristic high SiO_2 in the range of 66.08-76.63 wt.% and low to moderate concentration of Fe_2O_3 and MgO (1.56-4.91) and (0.33-1.2) wt.% respectively. The concentration of potash is higher than soda in the rock. The rock is acidic in composition. It characteristically includes high total alkali content, low CaO and a high FeO_{total}/ MgO content.

Irvine and Baragar (1971) suggested a triangular plot which is known as AFM diagram (proportion of total alkali (A) + FeO(F) + MgO(M)) on plotting the data; it suggests a calc-alkaline series (Figure 5.4). According to Shand (1943) the Phulad granite is peraluminous in nature but some fall in metaluminous portion (Figure 5.5). The geochemical nature of the

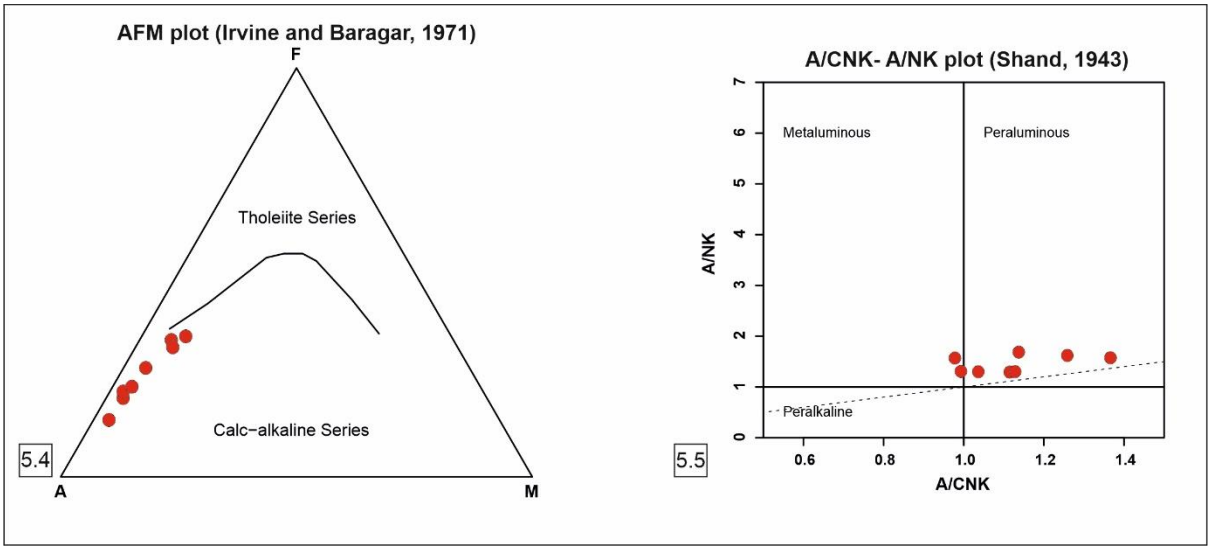

Figure 5.4-5.5: AFM diagram of Irvine and Baragar (1970) (5.4) suggests a calc- alkaline series for the Phulad granite. Geochemical classification of granitic rock samples shows peraluminous character on Alumina saturation index (ASI) diagram (Shand, 1943) (5.5).

studied granite is critically tested using the standard common schemes as well as the recently adopted three-tiered geochemical classification scheme of granitic rocks (Frost et al., 2001)

(Figure 5.6). Frost (2001) proposed a classified scheme depending upon the Fe, Mg number, trend and the MALI index.

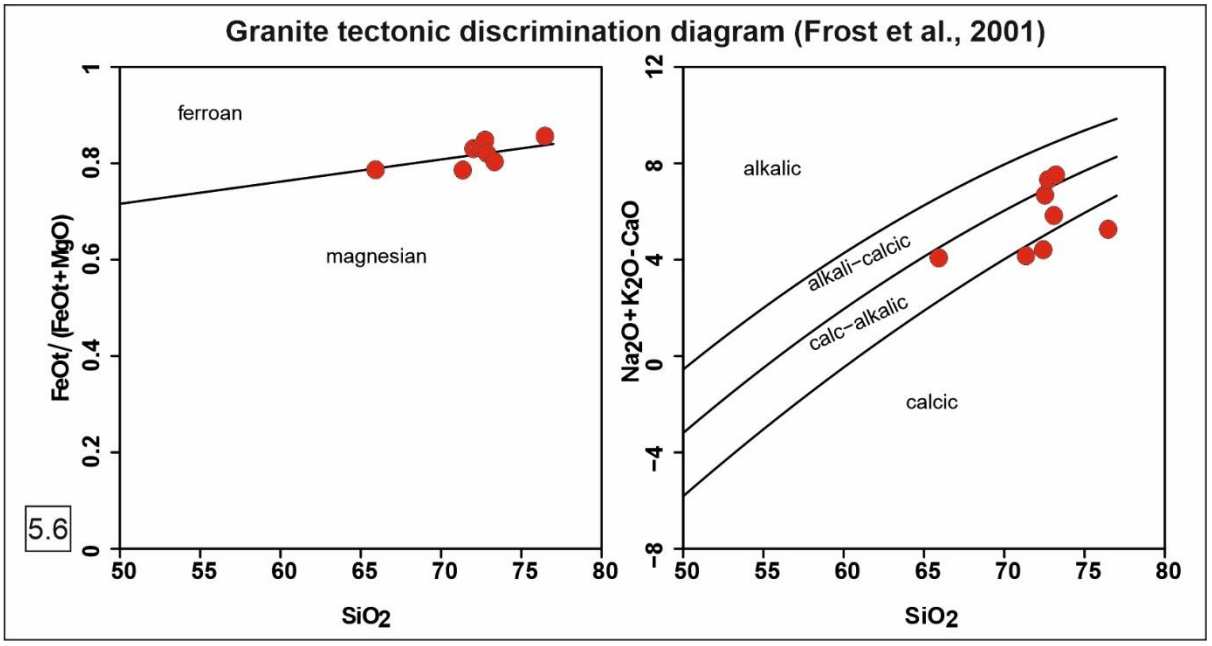

Figure 5.6: Studied Phulad granite sample's plot on Frost et al. (2001) granite tectonic discrimination diagram shows, both ferroan and magnesian [FeOt/ (FeOt + MgO) vs SiO2, wt.%] composition and calcic to alkali-calcic in nature [Na2O + K2O – CaO vs SiO2, wt.%].

5.4 Trace Element and REE Geochemistry:

The granite tectonic discrimination diagram of Pearce et al. (1984) shows syn-collisional behaviour along with some discrete positions (Figure 5.7). According to Pearce et al. (1984), Rb, Y and Nb are the most effective elements for tectonic discrimination of granites. Collectively, samples of Phulad granite show high average contents of Rb (~254 ppm), Ba (~318 ppm), high field strength elements (HFSE) (Nb~12 ppm, Zr~174 ppm, Y~35 ppm, Th~29 ppm and U~3 ppm) and depletion in Sr (~65 ppm). With the help of these elements, Pearce et al. (1984) generated a bivariate plot (Figure 5.7) which clearly distinguishes the Ocean Ridge (OR), Volcanic Arc (VA), Syn-Collisional (syn-COLG) and Within Plate (WP) granite groups. On plotting the recent data in these graphs, most of the samples fall in the syn-COLG field indicating it is syn-COLG Granite which again falls in the overlap zone indicating that it is

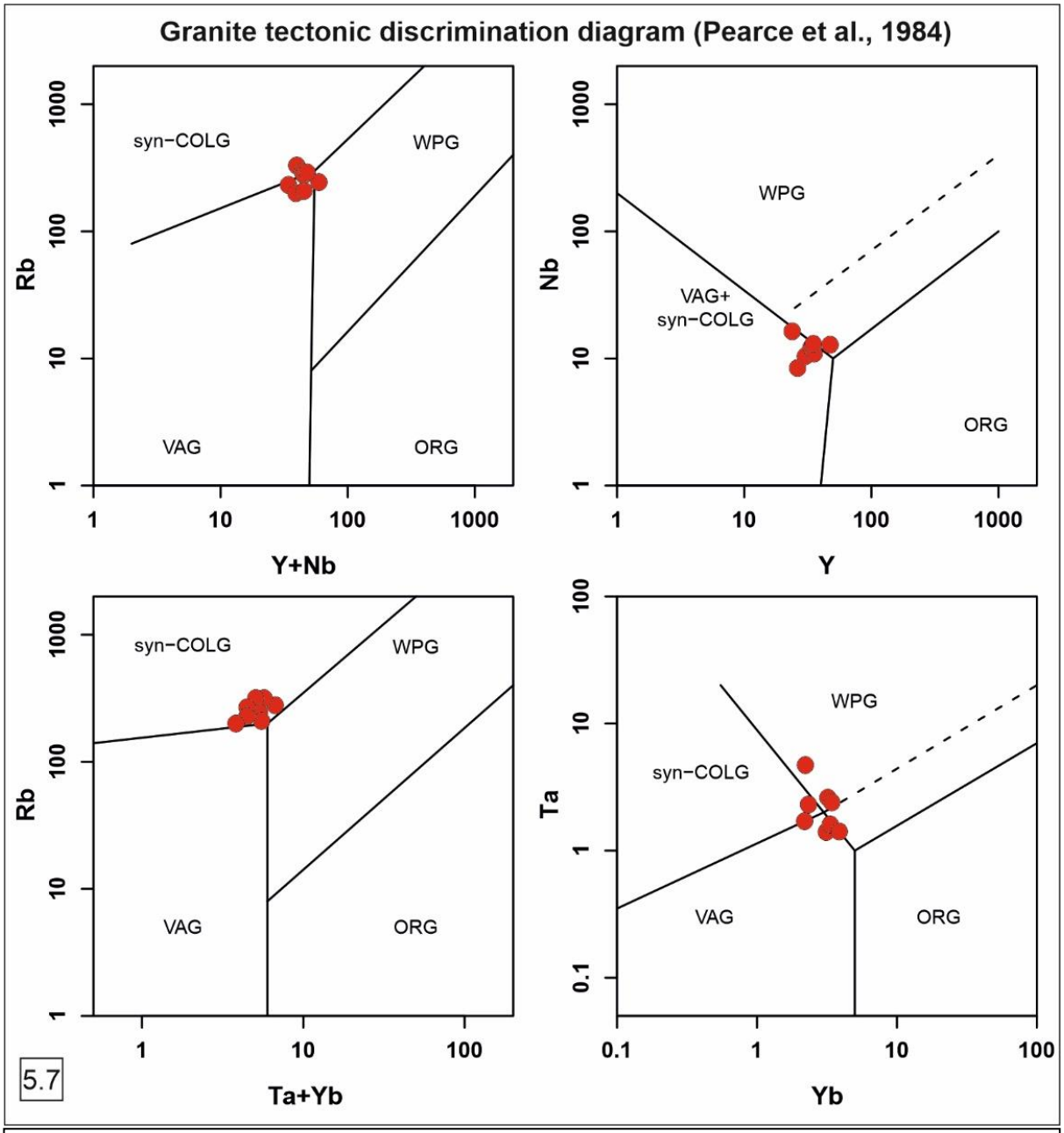

Figure 5.7: Granite tectonic discrimination diagrams of immobile trace element (Pearce et al., 1984) showing Syn-Collisional and Within Plate granitic field, VAG and Syn-COLG granitic field and Syn-COLG with few VAG and Within Plate granite field. Labels: WPG – within-plate granites, acc-WPG – attenuated continental crust within-plate granites, VAG – Volcanic Arc Granites, syn-COLG – syn-collision granites, ORG – ocean ridge granites, and an-ORG – anomalous ocean ridge granites.

syn-COLG granite from attenuated crust. Whalen et al. (1987) proposed a series of bivariant graph from which it can be suggested that whether the rock is A type granitoid or I&S type granitoids. The bivariate graph of Whalen et al. (1987) has 10000*Ga/Al in its x- axis and in its y axis, there is Na_2O+K_2O, $(Na_2O+K_2O)/CaO$, K_2O/MgO, FeOt/MgO, Zr, Nb, Y, Zn, Agpatic Index, shows all the samples of Phulad granite fall in I&S type granitoids (Figures 5.8-5.15).

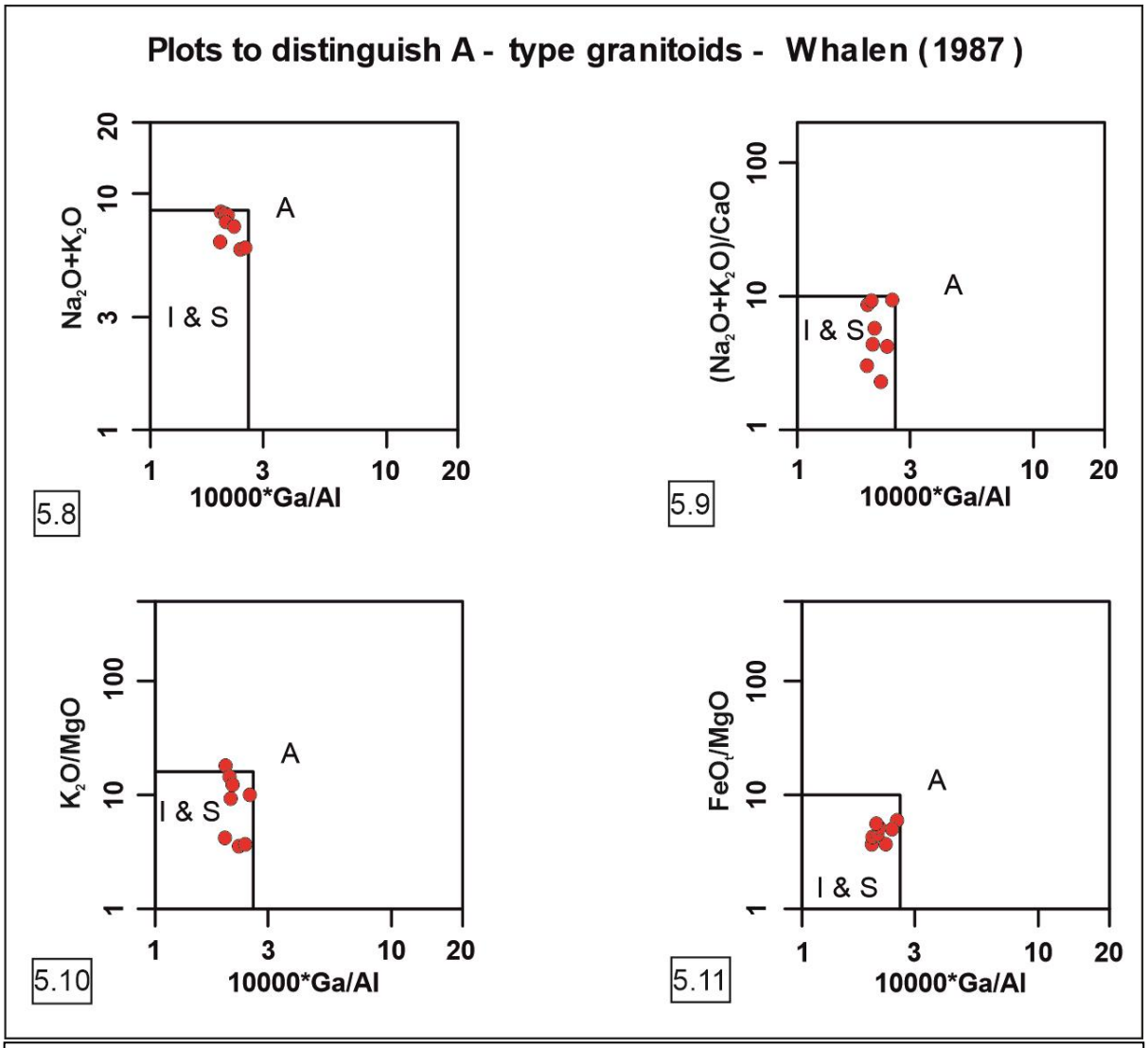

Figure 5.8-5.11: Tectonic discrimination diagram of Whalen (1987) showing I & S type granite.

The Phulad granite shows a moderate to high range of variation in transitional trace element compositions. They have a large range of REE concentrations and the total REE content range varies between 124-237 ppm. Trace elements vs. SiO_2 variation diagrams are shown in figures 5.16, 5.17. The variation patterns of most trace elements in the Phulad granite generally show simple fractionation trends. The Rb and Th contents increase, whereas the Sr, V, Zr and Sc contents decrease continuously as SiO_2 content increases.

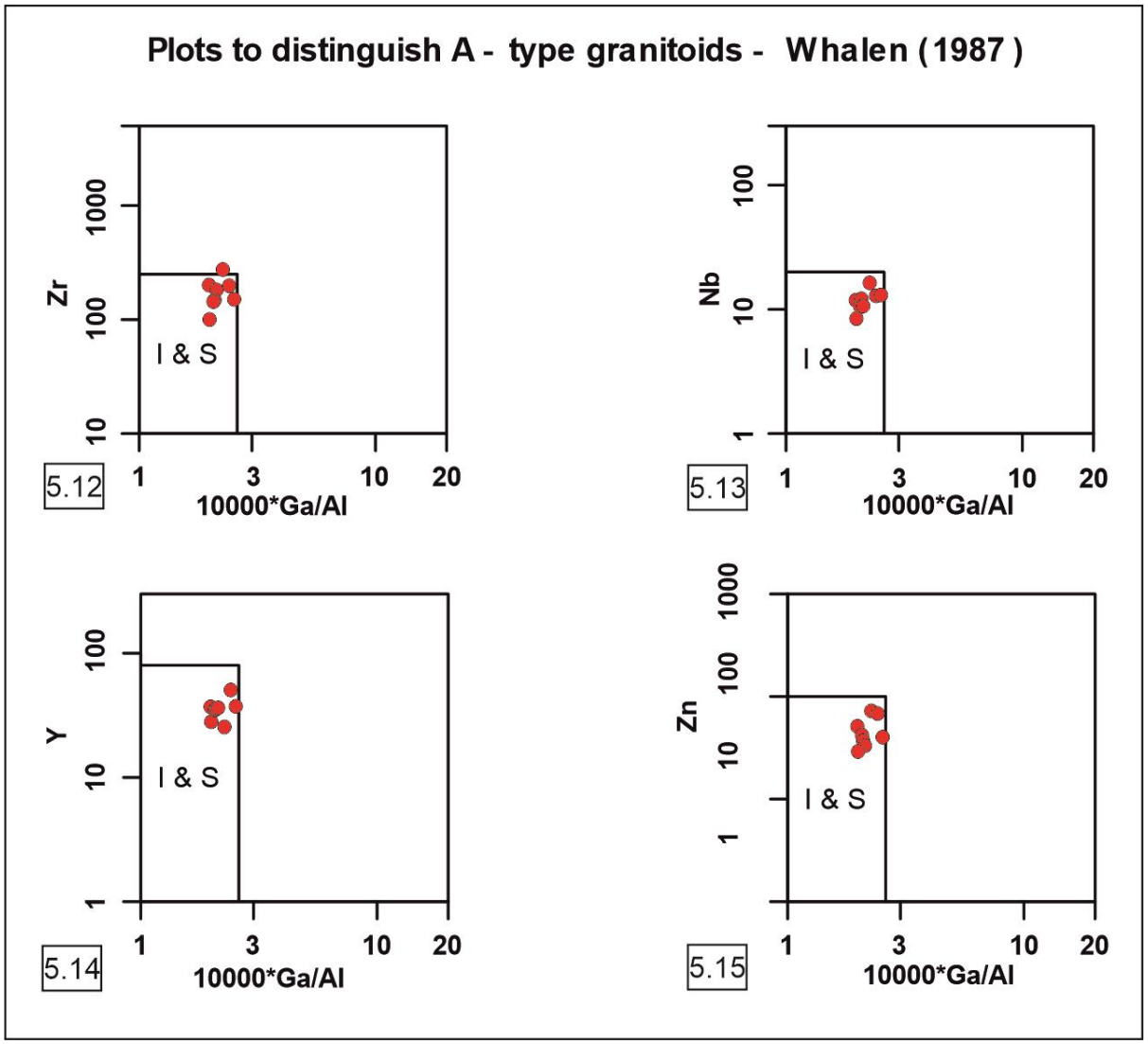

Figure 5.12-5.15: Tectonic discrimination diagram of Whalen (1987) showing I & S type granite.

On the other hand, the concentrations of large ionic lilhophile elements (LILEs) such as Rb, Ba, Th, and U seem to be similar in each group of granites (Figure 5.16), whereas those of high field strength elements (HFSEs) such as Nb, Zr, and Y are largely different (Figure 5.17).

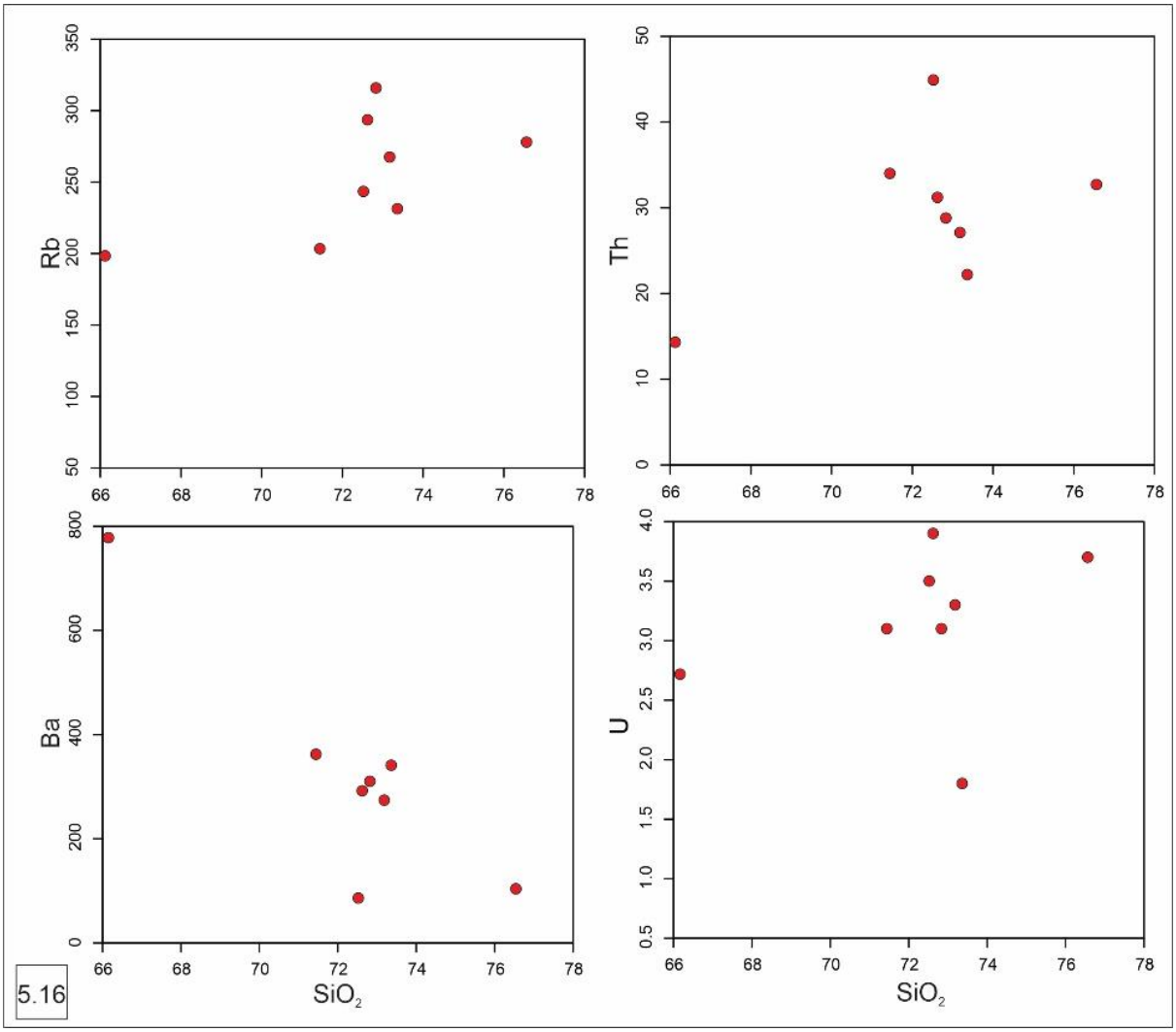

Figure 5.16: Trace elements vs. SiO_2 variation diagrams showing Rb, Ba, Th, and U vs. SiO_2 plot.

In terms of trace elements, this rock is characterised by high amount of HREE such as Y, Nb, Zr, Zn and Ga content. This criteria is actually used by trace element discrimination diagram of Pearce et al. (1984) and Whalen et al. (1987). The rock shows enrichment in HFSE elements. There is an enrichement of incompatible elements. Primitive mantle normalized (Sun and McDonough, 1989) trace element spider diagram for these granites shows enriched levels for incompatible elements (Figure 5.18). All the granite samples show a pronounced

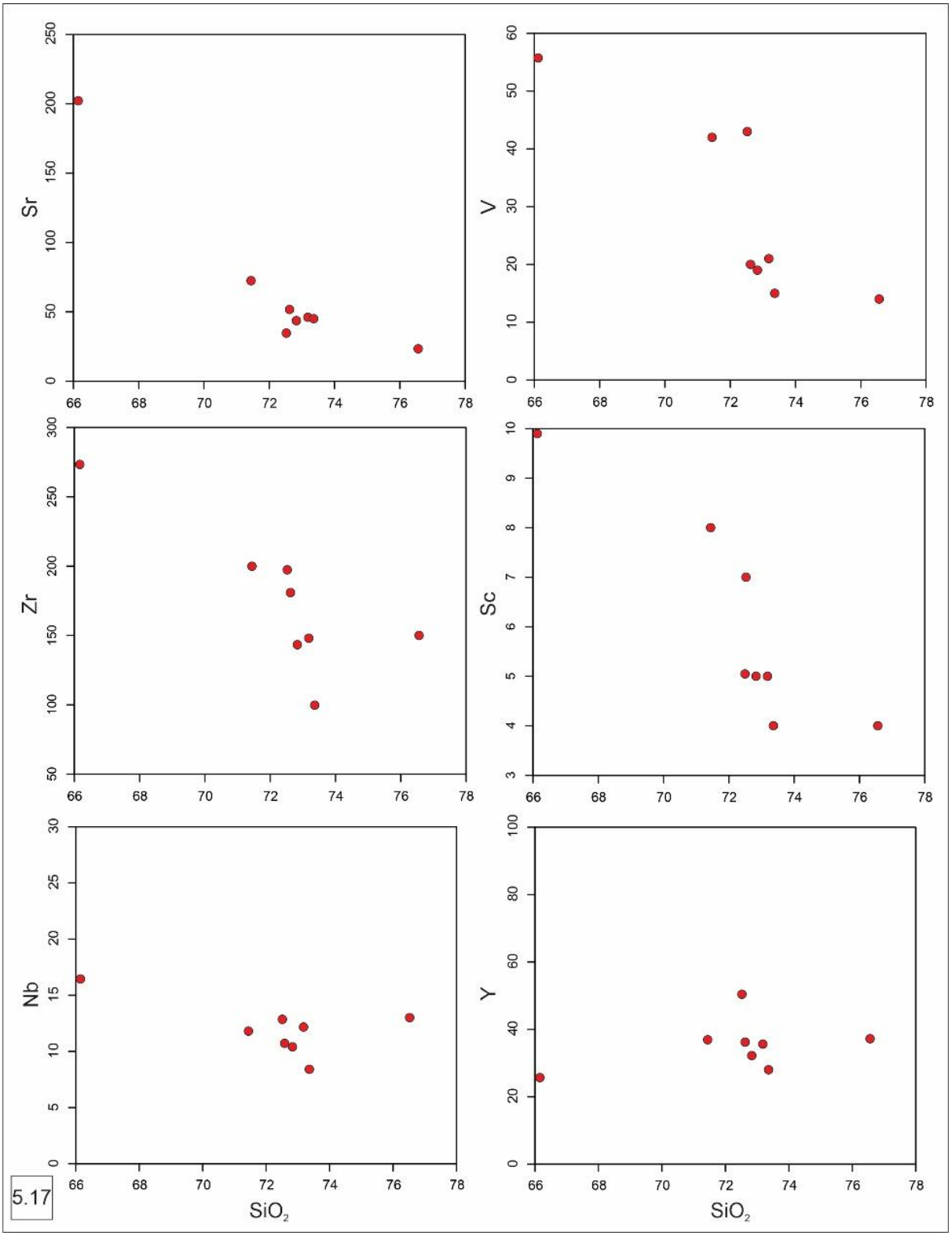

Figure 5.17: Trace elements vs. SiO_2 variation diagrams showing Sr, V, Zr, Sc, Nb and Y vs. SiO_2 plot.

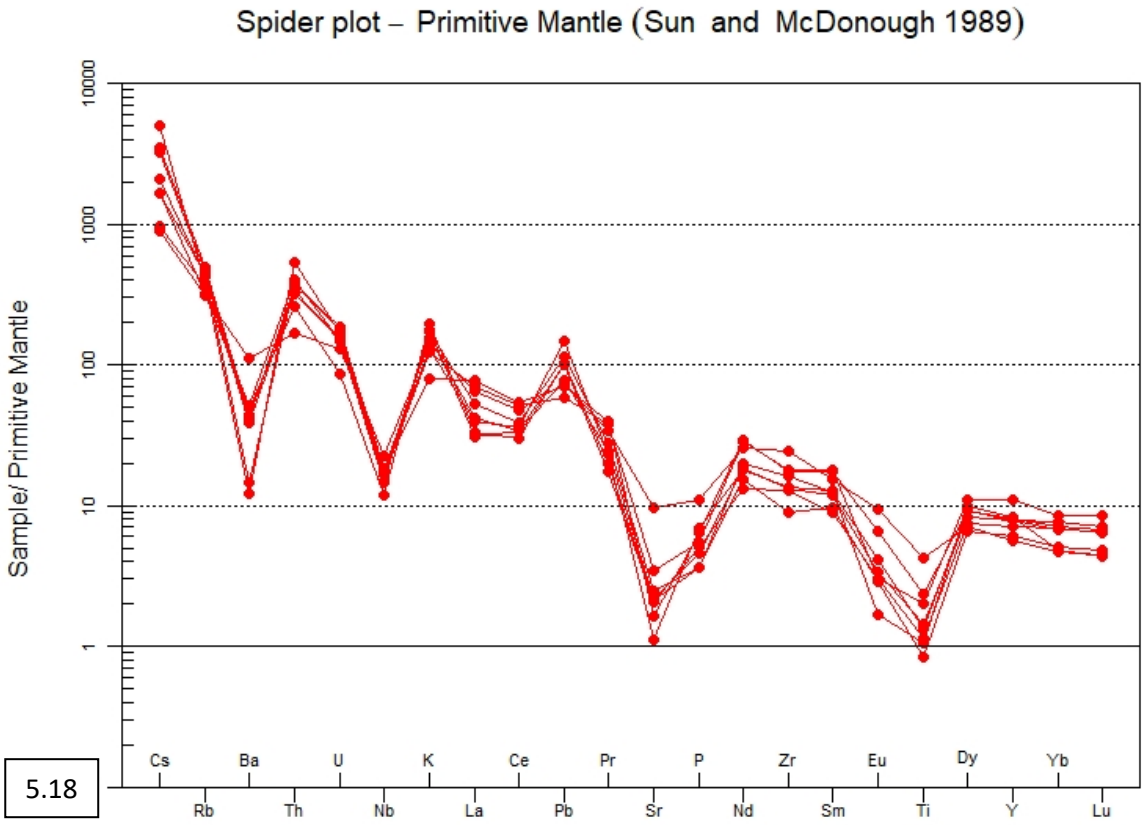

Figure 5.18: Primitive mantle normalized (Sun and McDonough, 1989) trace element spider diagram.

negative Nb, P and Ti-anomaly and small Ba, Sr, Zr and Pb anomalies. The REE Primitive mantle normalized (McDonnough and Sun, 1995) (Figure 5.19) for these rocks shows large LREE enrichment and flat HREE trends for most samples. The ocean ridge granite (ORG) normalized patterns (values from Pearce et al., 1984; Figure 5.7) demonstrate that all the studied granites are particularly depleted relative to ORG with notable Nb–Ta negative anomalies. This granite show similar patterns with a higher degree of REE fractionation ((La/Yb)N = 4.18–13.02). The granite shows high ΣREE (an average 172.46 ppm) content and moderate LREE enrichment((La/Sm)N = 3.00–4.17) with moderate but relatively flat HREE ((Gd/Yb)N = 1.00–

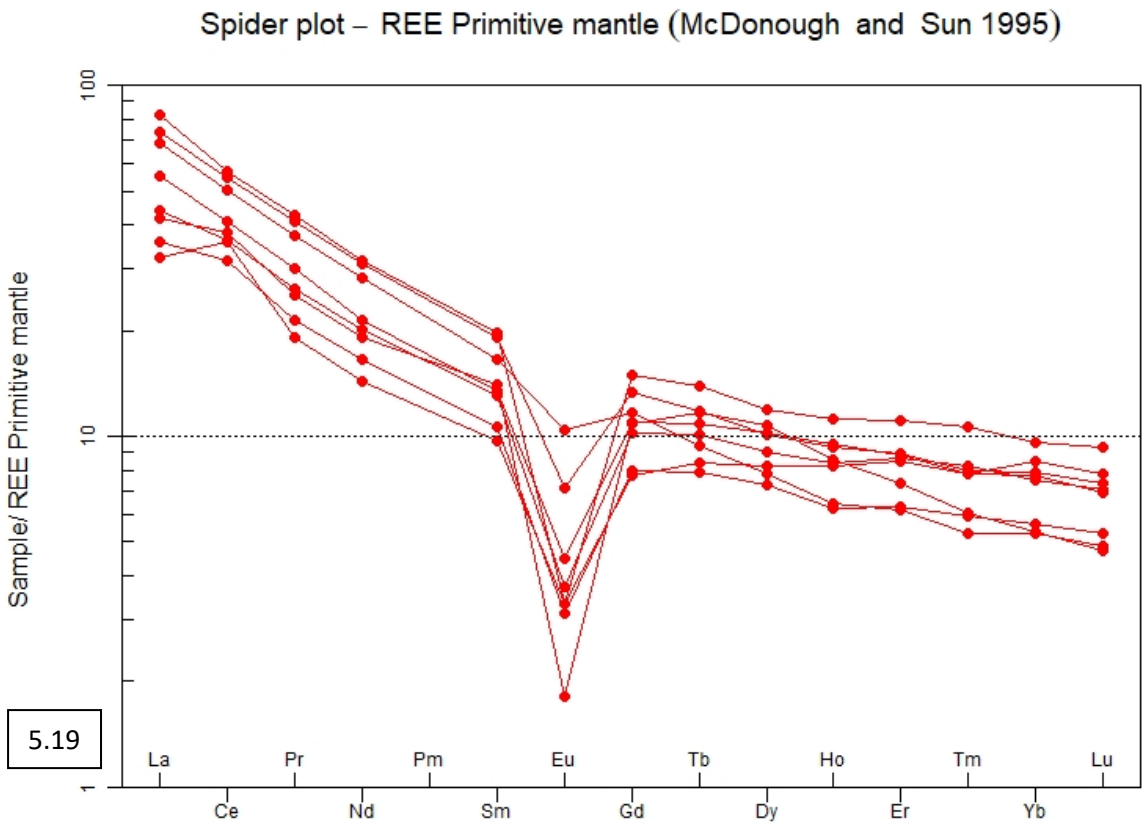

Figure 5.19: REE primitive mantle normalized (McDonough and Sun, 1995) trace element spider diagram.

2.22) patterns. The Europium anomaly is the phenomenon whereby the europium (Eu) concentration in a mineral is either enriched or depleted relative to some standard, commonly a chondrite or mid-ocean ridge basalt (MORB). All the samples show moderate negative Eu anomalies [(Eu/Eu*)=0.15-0.75] (McDonough and Sun, 1995) that can be due to plagioclase removal or represent a source characteristic.

5.5 Volume Strain and Volume Calculation:

To examine the chemical fractionation entailed by volume strain, eight least deformed and four deformed samples were used. TiO_2, MgO, and Al_2O_3 are considered as immobile elements (Ague, 1994) and show a negative correlation with SiO_2 (Figures 5.20-5.22) (Breeding and Ague, 2002). The Al_2O_3-TiO_2 plot shows a positive correlation (Figure 5.23). As

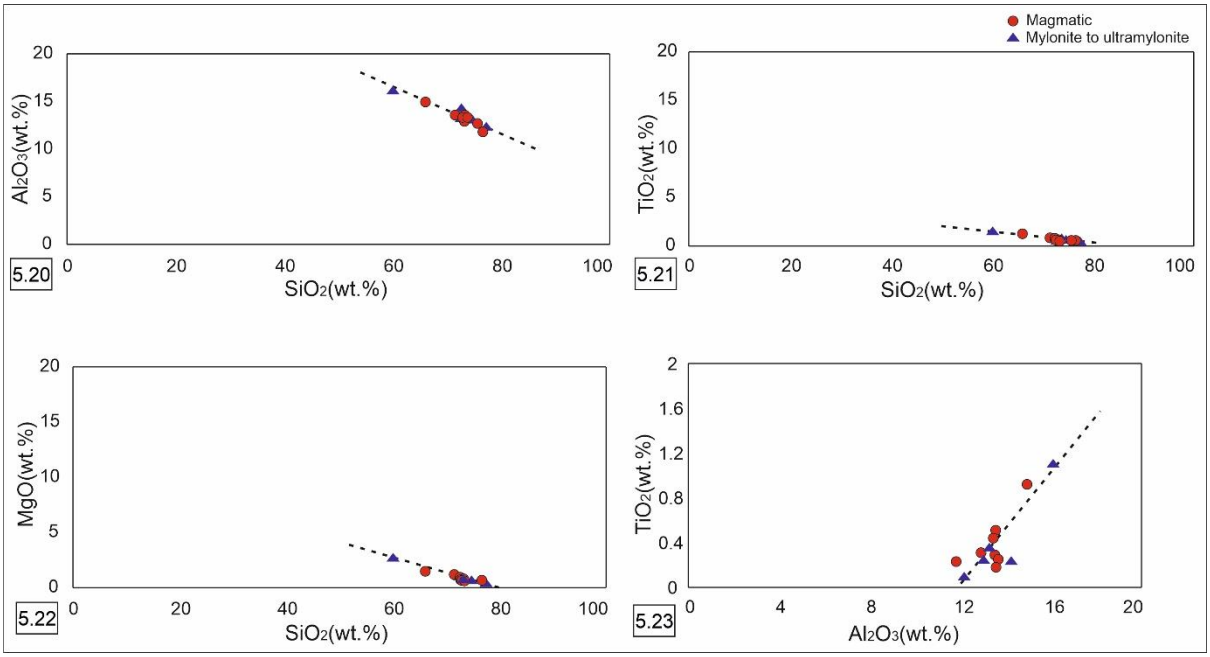

Figure 5.20-5.23: Plots of TiO_2, MgO, and Al_2O_3 vs. SiO_2 (5.20-5.22) and Al_2O_3 vs. TiO_2 (5.23).

SiO_2 shows a negative correlation with TiO_2, MgO, and Al_2O_3, with deformation SiO_2 content increases and as Al_2O_3-TiO_2 plot reveals a positive correlation, both the oxides are increased.

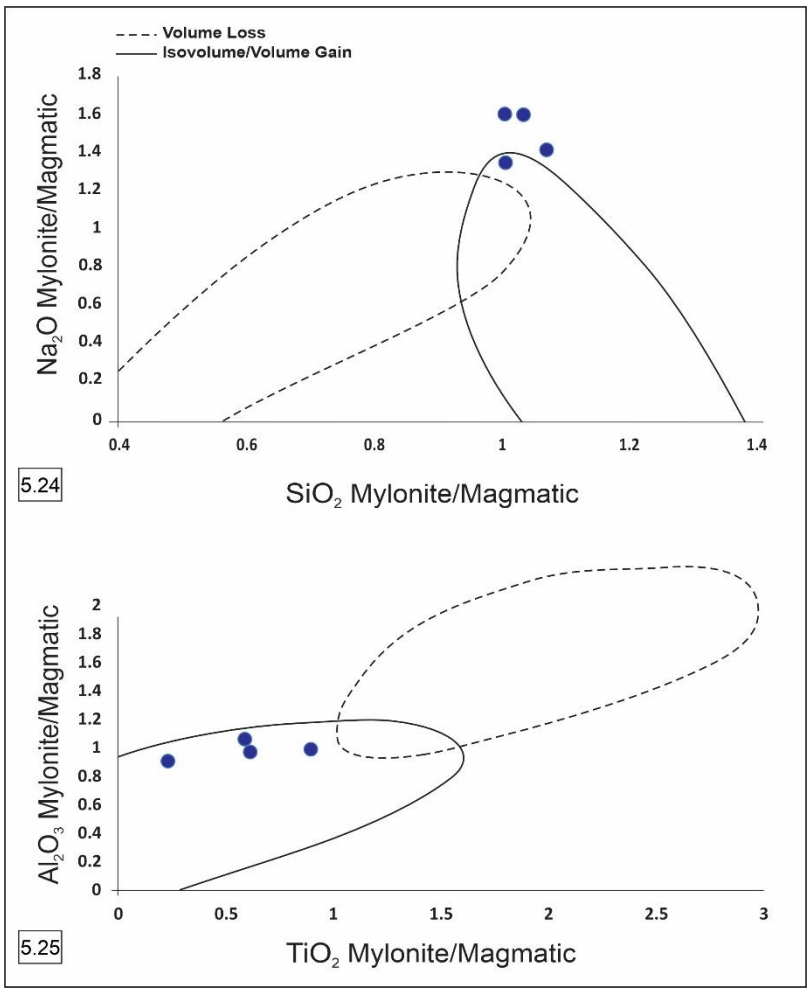

Figure 5.24-5.25: Plot of concentration ratios mylonite/magmatic (5.24) for Na_2O and SiO_2 and (5.25) Al_2O_3 and TiO_2 for the four mylonites or composite mylonites/ultramylonites used in this investigation. The fields for volume-loss and isovolume/volume-gain mylonitic shear zones, determined from 'isocon analyses' calculated from published chemical analyses worldwide, are approximations from data given in Condie and Sinha (1996).

On the other hand, calculating changes in rock volume in volume-gain or volume-loss situations (Ramsay, 1980; O'Hara, 1988; Bailey et al., 1994) was

taken a step further in Condie and Sinha's (1996) study of many shear zones worldwide. These authors' devised plots of normalized mylonite/protolith ratios for selected oxides, in particular SiO_2, Al_2O_3, Na_2O and TiO_2, that allowed discrimination amongst volume-loss and volume-gain shear deformation and mylonitization processes. These discriminants have been applied in the case of the mylonites and magmatic variety of Phulad granite. So, there is the volume-gain/isovolume category in the high-strain shear zone (Figures 5.24-5.25).

5.6 Mass-Balance Calculation:

Mass-balance calculation is an important tool in different geological processes to quantify the mass transfer and its associated volume change in a particular geological setting (Gresens, 1967; Grant, 1986; Ague, 1994; Durand et al., 2015). Many workers have used different methods to quantify the qualitative gains or losses in chemical mass and associated volume change during shear zone development. Based on the mass-balance equation (Gresens, 1967) isocon diagrams (Grant, 1986, 2005) were constructed, which have been widely used to study fluid-rock interaction in the shear zones (e.g., O'Hara, 1988; Newman and Mitra, 1993; Ring, 1999; Rolland et al., 2003; Yonkee et al., 2003; Tart`ese et al., 2012; Maggi et al., 2014; Durand et al., 2015). Here, the isocon method was also used, a graphical approach for the quantitative analysis of chemical mass transfer during progressive deformation derived from the equation after Grant (1986) to show the compositional changing relation between the protolith/magmatic and the mylonites:

$M^A(C^A_n/C^O_n) = M^O$ (Grant, 1986, 2005), (1)

Where C^O_n and C^A_n represent the concentration of the n^{th} component of protolith/magmatic and mylonites respectively. M^O and M^A represent the equivalent masses of their respective composition. As the immobile elements do not show any mass gain or loss, ΔC_n of Gresens'

(1967) equation is negligible and thus equation (1) represents the isocon equation that is represented by the immobile element. Based on the assumption that the elements are immobile or sustained during deformation and the ratios of their concentrations in the protolith/magmatic and mylonites prevail constant. These ratios could be used as parameters to evaluate changes in mass. In the isocon diagram, concentrations of the components of protolith/magmatic (C^O_n) and altered (C^A_n) rocks are plotted in the X and Y axis, respectively. In this plot, the best-fit line represents the isocon and the slope of the line defines the change in mass relative to M^O during the chemical mass transfer process.

Major element distribution is associated with the formation of the mylonitic variety of the Phulad granite. Relative to the least deformed/magmatic variety, water increases in the mylonitic variety as measured by Loss on ignition (LOI) (~10%), but there is little change in other major elements. SiO_2 wt.% increased around 3% whereas other major oxides show losses with the exception of CaO and Na_2O show gain such as 3% and 49% respectively. TiO_2, K_2O and Al_2O_3 show losses of 42%, 48% and 2% respectively. In the mylonitic variety, there is a slight increase in CaO, SiO_2 and a large increase in Na_2O accompanied by decreases in Al_2O_3, FeO^T, TiO_2, MgO, K_2O and P_2O_5 (Figure 5.26).

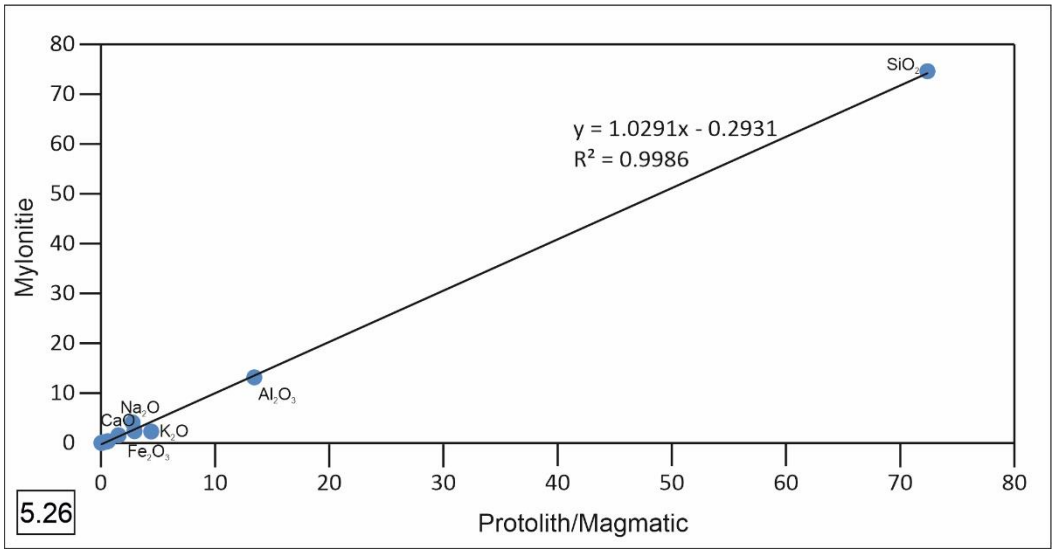

Figure 5.26: Isocon diagram showing comparison between the major oxides of mylonitic or altered to the magmatic variety of Phulad granites.

5.7 Summary:

The eight samples most of them fall in the granite segment of Middlemost (1994), De la Roche et al. (1980). Some of them fall in granodiorite field. But overall, the samples show the granitic nature.

Major element geochemistry of the granitic rock confirms the granite nomenclature. The granite shows characteristic high SiO_2 and low concentration of Fe_2O_3 and MgO. The granitic samples which are least deformed show higher concentration of K_2O (4.41 wt.%) than Na_2O (2.76 wt.%) and it characteristically includes high total alkali content, low CaO and a high Fe_2O_3/MgO (5.24 wt.%) content. Geochemical signature of the granite show ferroan type, calc-alkalic and metaluminous in nature which suggests they have formed from the partial melting of granodioritic to tonalitic crustal rock. Trace element tectonic discremination diagram of Pearce et al. (1984) indicates the granite falls under the category of syn-collisional granite (Figure 5.7). Plotting the data in series of bivarient graph of Whalen et al. (1987) suggests the rock is I&S-type granitoid. These clearly suggests that it was derieved from a felsic source.

The incompatible behaviour of Eu indicates melting of a source with little plagioclase. The other probable explanation for the depleted HREE could be the late-stage fractionation of heavy mineral phases like zircon, apatite, and monazite because of their extremely high partition coefficients for HREE (Peter Gromet and Silver, 1983; Rollinson, 1993). These features can be explained by melting of such source rock will result in melts with negative Eu anomalies and enriched HREE with low LREE/HREE ratios (Barker, 1979; Martin, 1999). These features can further be explained by the fractional crystallization of plagioclase from the melt followed by late-stage hornblende crystallization to deplete the LREE and impart the low LREE/HREE ratios (Barker and Arth, 1976; Barker, 1979). The smaller Ba and Sr anomalies

suggest that earlier fractionation of K-feldspar and plagioclase was significant. Barium readily substitutes for K in feldspar and biotite, so that the negative Ba anomaly may be related to high temperature feldspar fractionation (Rollinson, 1993; Arslan and Aslan, 2006).

The Phulad granite shows volume-gain/isovolume signature as Na_2O and SiO_2 increase. An increase in SiO_2 with deformation in the shear zone reflects the introduction of quartz. In the ductile shear zone effect of fluid is common, and in this present study, it can be seen that SiO_2 wt.% increased around 3% where other major oxides show losses except for CaO and Na_2O show gain; TiO_2, K_2O and Al_2O_3 show losses.

Chapter 6

Geochronology

6.1 Introduction:

The U-Th-Pb age dating technique is a precise and powerful method to date crystallization ages and metamorphic events. The mineral zircon ($ZrSiO_4$) is suitable for age dating as it is extremely robust and remaining essentially unaffected by subsequent geological events and often contains relatively large amounts of U, Th and Pb. In situ micro beam techniques enable the study of individual growth zones in zircons which can reveal vital information about the growth sequence and evolution of the mineral and its host rocks. Apart from zircon, in-situ chemical age determinations in monazite grains were also done using Electron Microprobe Analyzer (EPMA) for the Phulad granite. In this work radiometric age data discussed to deliver implications of our data for the tectonics of northwestern India. There is a brief description of U-Th-Pb geochronology method below.

6.2 U-Th-Pb Method:

The U-Th-Pb method is based on the radioactive decay of U and Th to stable isotopes of Pb. U naturally occurs as radiogenic isotopes ^{238}U, ^{235}U and ^{234}U and Th primarily as radiogenic ^{232}Th. Pb exists as radiogenic isotopes ^{206}Pb, ^{207}Pb, ^{208}Pb and non-radiogenic isotope ^{204}Pb. ^{204}Pb is also referred to as common Pb and often represents contamination on the surface of the sample. Each of the U and Th isotopes reflects the parent of a chain of radiogenic daughter isotopes which all decay to a stable isotope of Pb, i.e., ^{238}U decays to ^{206}Pb, ^{235}U to ^{207}Pb and ^{232}Th to ^{208}Pb. The U, Th and Pb concentrations in the Earth's mantle are very low. During partial melting of the mantle U, Th and Pb preferentially get incorporated into the liquid phase. This leads to enrichment of U, Th and Pb in the crust in comparison to the mantle. In common rock forming minerals the concentrations of U and Th are very low. However, high

abundances can be found in accessory minerals, e.g., zircon and monazite where U and Th are either a major constituent of the mineral or substitute for other elements. Zircon is commonly used for U-Th-Pb geochronology as it is the most abundant accessory mineral in most igneous and metamorphic rocks. It has the advantage of being chemically and mechanically extremely robust and it readily incorporates U and Th but not Pb. Therefore, at the time of crystallization virtually no Pb is present in the zircon. After crystallization is completed the radioactive decay of U and Th begins to produce Pb. By measuring the concentrations of U, Th and Pb in the zircon sample and determining the isotopic composition of Pb the age of the zircon can be calculated.

6.3 Sample Preparation for Zircon and Monazite Grains:

U-Pb geochronology of zircon was carried out on one representative granite sample (P-647) (Figure 2.8). Zircon was separated from 3 to 5 kg of rock samples following the procedure mentioned in the flow chart (Figure 6.1). Thereafter, zircon grains were handpicked under a stereo microscope and zircon grains were mounted in epoxy. The mounted zircon grains were then polished using 8, 5, 3, 1, and 0.25 µm diamond paste. After mounting the zircon grains cathodoluminescence (CL) images of were obtained at Indian Institute of Technology, Kharagpur.

Monazite grains were identified by their lozenge shape in thin section under the transmitted microscope and marked them for further analysis.

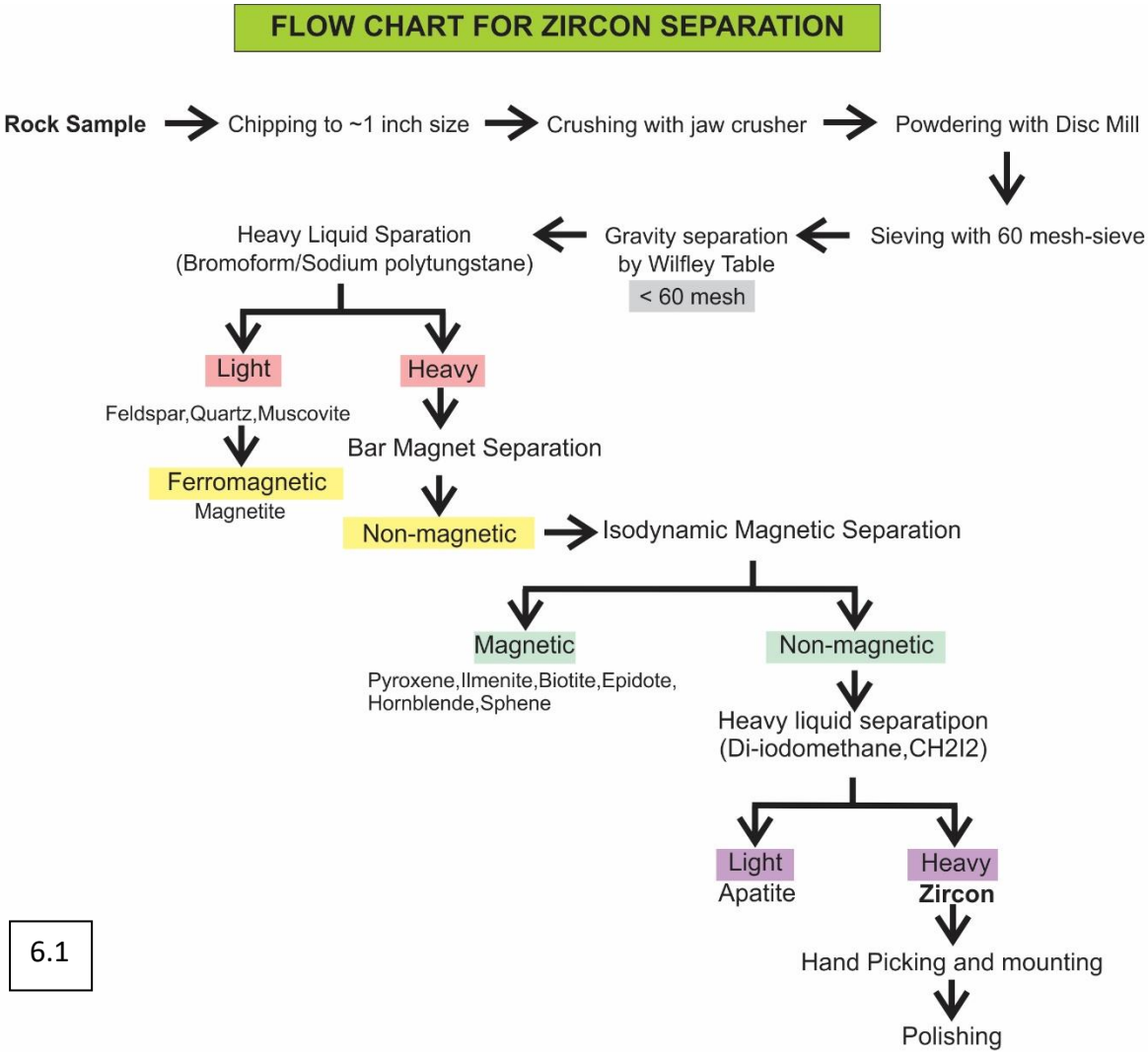

Figure 6.1: Flow chart for zircon separation.

6.4 Monazite Age Determination:

In-situ chemical age determinations in monazite grains were carried out on five samples; two samples from Phulad granites (P-671, P-673; sample locations are shown in figure 2.8) and three samples from the pegmatites of N-S bends (P-462, P-794, P-822; sample locations are shown in figure 2.8). Quantitative microprobe analyses of monazite grains were carried out using the Cameca SX-100 EPMA at the Department of Geology and Geophysics, Indian Institute of Technology, Kharagpur. Quantitative analyses of major elements, REEs, Y, U, Pb

and Th in monazites were done with 20 kV acceleration voltage and 200 nA beam current (details of analytical protocol is provided in Prabhakar, 2013). Data quality was controlled by measuring an ID-TIMS dated monazite standard, e.g., JCA-08 M3 from Brazil [TIMS age of 487 ± 1 Ma, Crowley et al., 2005; EPMA age of 497 ± 10 Ma, Spear et al., 2009; TIMS age of 509.3 ± 0.5 Ma, Spear et al., 2009]. The standard yielded age of 490.4 ± 4.6 Ma (n = 61, mean square weighted deviation; MSWD = 0.28). Calculation of spot ages was done using the formulation of Montel et al. (1996) and the age probability plots were constructed using the Isoplot\Ex software (Ludwig, 2003). The representative analytical data are shown in table 6.1.

The monazites within Phulad granites are 50 to 100 µm in diameter (Figures 6.2, 6.3) with dominantly euhedral faces. They are mainly included in primary minerals most notably in quartz, feldspar, and biotite grains (Figures 6.4-6.6). These monazites do not occur in clusters.

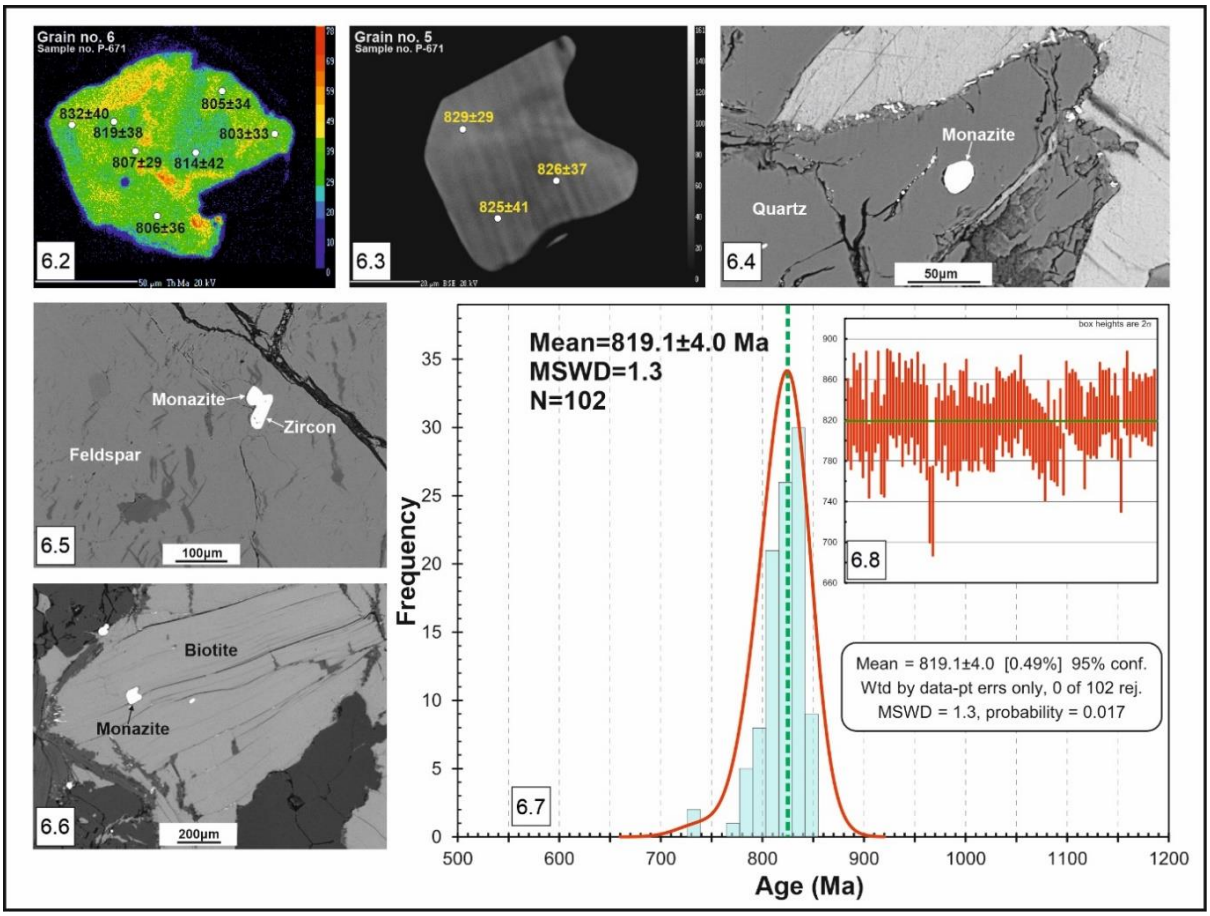

Figure 6.2-6.8: Photomicrographs in Th X-ray map (6.2) and BSE image (6.3) showing the euhedral monazite grains, BSE images (6.4-6.6) showing monazite grain included in quartz, feldspar, and biotite grains in Phulad granite respectively, (6.7) plot of relative probability and frequency of spot ages in monazite grains of Phulad granite, (6.8) weighted average age of the Phulad granite monazite=819.1 ± 4 Ma with MSWD=1.3.

The morphology, internal structure and their high Th value of these monazite grains suggest magmatic origin and therefore the ages obtained are taken to represent the timing of granite crystallization. All the monazite spot ages in Phulad granite correspond to a single age group (Figure 6.7). The weighted average age is 819.1 ± 4 Ma with MSWD (mean square weighted deviation) = 1.3 (Figure 6.8). Monazites in the pegmatites are 50 to 150 µm in diameter and exhibit strongly resorbed margins (Figures 6.9, 6.10). All the monazite spot ages in pegmatites also correspond to a single age group (Figure 6.11). The weighted average age is 819.7 ± 4.5 Ma with MSWD = 2.1 (Figure 6.12).

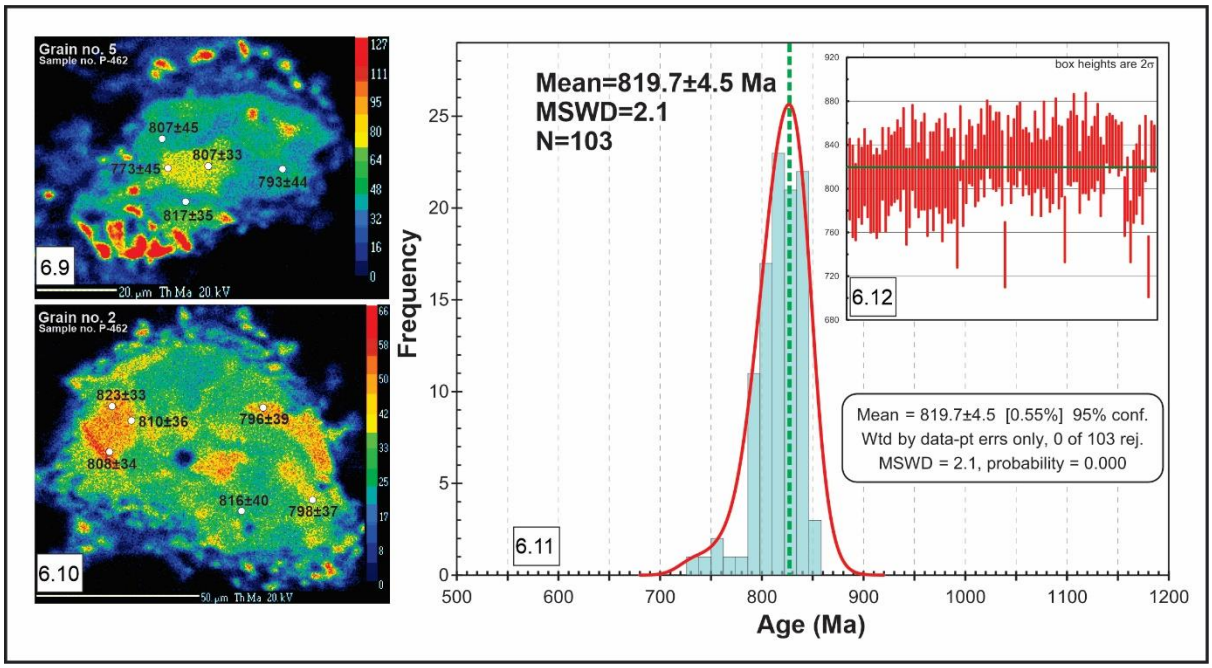

Figure 6.9-6.12: Photomicrographs in Th X-ray map (6.9-6.10) showing monazite grains from pegmatite, (6.11) plot of relative probability and frequency of spot ages in monazite grains from pegmatite and (6.12) weighted average age of pegmatite monazite=819.7 ± 4.5 Ma with MSWD=2.1.

Table 6.1: Y, Pb, Th, and U concentrations and calculated ages (With 2σ Errors) in Monazites in the Phulad granite and Pegmatites.

a. Granite

Sample Number	Y_2O_3	PbO	ThO_2	UO_2	Age (Ma)	Age error
P-671	1.906	0.439	10.685	0.423	845	33
	1.825	0.507	12.453	0.498	836	30
	1.819	0.474	11.582	0.472	839	31
	1.755	0.398	9.572	0.477	832	35
	1.706	0.418	10.397	0.426	825	34
	1.754	0.470	11.809	0.454	822	31
	1.759	0.365	9.590	0.365	788	35
	1.807	0.493	12.562	0.450	817	30
	1.741	0.362	9.267	0.304	820	37
	1.743	0.415	10.651	0.349	819	33
	1.713	0.486	12.351	0.474	813	30
	1.701	0.319	7.835	0.321	836	41
	1.711	0.493	12.198	0.454	838	31
	1.903	0.471	11.722	0.417	838	31
	1.809	0.480	11.892	0.426	840	31
	1.942	0.484	12.287	0.470	814	30
	1.906	0.457	10.150	0.780	834	32
	1.988	0.458	9.975	0.941	813	31
	1.691	0.326	8.963	0.293	766	36
	1.922	0.536	13.039	0.535	842	29
	1.608	0.326	8.055	0.276	847	41
	2.015	0.452	11.351	0.469	816	32
	1.945	0.504	12.430	0.482	837	30
	1.994	0.552	13.580	0.565	832	28
	2.015	0.532	12.959	0.561	836	29
	1.960	0.545	13.419	0.574	829	29
	1.640	0.489	12.038	0.484	835	31
	1.795	0.416	10.523	0.347	829	33
	1.831	0.412	10.328	0.377	829	34
	2.007	0.526	12.916	0.500	840	30
	1.718	0.360	8.996	0.373	819	38
	1.719	0.397	10.052	0.434	805	34
	2.084	0.478	11.739	0.532	824	30
	2.210	0.471	9.732	1.155	807	29
	1.701	0.306	7.650	0.330	814	42
	2.172	0.417	9.156	0.886	803	33
	1.839	0.367	9.229	0.419	806	36
	1.760	0.325	7.889	0.364	832	40
	2.108	0.481	9.208	1.246	837	31
	1.783	0.350	8.827	0.325	823	38
	1.963	0.536	13.317	0.525	829	29
	1.857	0.346	8.692	0.322	826	37
	1.772	0.313	7.662	0.351	825	41
	1.982	0.462	11.269	0.480	836	33
	1.998	0.528	13.134	0.518	828	30

Table 6.1: Continued

Sample Number	Y2O3	PbO	ThO2	UO2	Age (Ma)	Age error
P-671	1.702	0.406	9.910	0.372	848	36
	1.777	0.365	8.673	0.501	823	37
	2.067	0.520	12.882	0.557	823	30
	2.029	0.491	12.195	0.545	816	30
	1.898	0.399	9.372	0.652	806	34
	1.796	0.470	11.883	0.489	810	31
	1.867	0.353	9.025	0.385	800	37
	1.860	0.434	11.144	0.445	801	32
	1.737	0.277	7.262	0.298	784	43
	1.715	0.340	8.363	0.393	820	39
	2.018	0.499	12.832	0.568	791	29
	1.675	0.313	8.056	0.320	800	40
	1.981	0.479	12.580	0.501	785	29
	1.989	0.522	12.887	0.574	822	29
	2.244	0.443	9.172	1.233	777	30
P-673	1.730	0.330	8.162	0.362	821	40
	1.756	0.321	7.914	0.393	812	40
	1.840	0.276	6.756	0.267	841	45
	1.915	0.330	8.024	0.374	829	40
	1.771	0.263	6.558	0.249	828	48
	1.996	0.335	8.419	0.398	802	38
	1.716	0.255	6.317	0.230	839	49
	2.077	0.349	9.272	0.350	780	36
	2.005	0.340	8.578	0.365	809	38
	2.061	0.392	9.886	0.363	824	35
	1.753	0.290	7.041	0.289	843	45
	2.165	0.281	6.281	0.604	791	43
	2.009	0.230	4.814	0.581	795	50
	1.890	0.229	5.036	0.404	836	54
	1.723	0.338	8.291	0.301	847	41
	1.790	0.385	9.538	0.340	840	37
	1.776	0.420	10.632	0.355	828	34
	1.915	0.348	8.513	0.323	846	40
	1.862	0.300	7.621	0.289	816	41
	1.693	0.340	8.527	0.273	838	40
	1.965	0.312	7.836	0.285	829	42
	1.931	0.370	9.180	0.319	842	38
	2.017	0.330	8.249	0.350	817	40
	1.943	0.295	7.205	0.288	842	45
	1.735	0.296	7.472	0.312	812	43
	1.814	0.274	6.838	0.258	829	46
	1.724	0.270	6.857	0.279	808	46
	1.948	0.303	8.446	0.348	737	37
	1.905	0.224	6.306	0.257	731	44
	2.314	0.419	10.797	0.389	809	33

Table 6.1: Continued

Sample Number	Y_2O_3	PbO	ThO_2	UO_2	Age (Ma)	Age error
P-673	1.971	0.359	9.119	0.332	819	37
	2.025	0.367	9.426	0.365	804	35
	1.863	0.324	7.974	0.321	836	40
	1.790	0.291	7.359	0.326	803	41
	2.002	0.289	7.446	0.258	812	42
	2.001	0.332	8.011	0.468	810	39
	1.952	0.324	8.419	0.324	795	39
	1.762	0.247	6.149	0.263	820	49
	1.872	0.296	7.372	0.299	825	43
	1.697	0.244	6.059	0.235	831	49
	2.055	0.372	8.816	0.579	807	36
	3.142	0.351	7.772	0.710	806	36
b. Pegmatite						
P-462	1.691	0.421	10.536	0.330	842	34
	1.993	0.454	11.856	0.436	796	30
	1.783	0.455	11.682	0.387	818	31
	1.837	0.539	13.536	0.454	834	29
	1.835	0.602	15.135	0.531	830	27
	2.095	0.607	14.750	0.817	810	26
	1.708	0.387	9.802	0.342	824	35
	1.698	0.477	11.914	0.389	841	32
	1.747	0.547	14.381	0.351	821	28
	1.667	0.486	12.159	0.350	850	31
	1.653	0.446	11.171	0.343	843	33
	1.617	0.477	12.257	0.331	831	31
	1.605	0.393	9.858	0.339	834	36
	1.937	0.413	10.318	0.357	836	34
	2.005	0.408	10.509	0.328	819	34
	1.926	0.413	11.663	0.412	740	30
	1.978	0.508	12.446	0.505	837	30
	2.115	0.482	9.424	1.292	817	30
	2.118	0.512	9.815	1.340	834	30
	1.888	0.382	9.378	0.368	839	37
	2.070	0.501	12.101	0.497	848	31
	1.958	0.487	12.167	0.487	824	30
	1.898	0.648	16.276	0.574	830	26
	1.836	0.541	13.656	0.500	823	28
	1.593	0.410	10.586	0.373	809	33
	1.702	0.375	9.384	0.329	834	37
	1.969	0.598	15.035	0.538	828	27
	1.858	0.372	9.661	0.313	810	35
	1.888	0.340	8.501	0.278	841	39
	1.898	0.611	15.659	0.530	818	26
	1.745	0.384	10.075	0.282	813	34
	1.636	0.338	8.599	0.280	826	39
	1.707	0.427	10.241	0.435	849	34

Table 6.1: Continued

Sample Number	Y_2O_3	PbO	ThO_2	UO_2	Age (Ma)	Age error
P-462	1.582	0.344	8.719	0.314	820	38
	1.946	0.453	9.300	1.044	825	32
	1.892	0.436	12.202	0.345	763	30
	1.740	0.493	12.401	0.409	834	30
	1.755	0.332	9.189	0.250	773	45
P-822	1.140	0.827	22.292	0.388	818	22
	1.092	0.937	24.555	0.393	845	21
	1.591	0.593	14.960	0.433	842	27
	1.483	0.754	19.440	0.422	843	24
	1.044	0.879	23.083	0.382	841	22
	1.487	0.751	19.489	0.438	835	23
	1.094	0.829	21.806	0.369	839	22
	1.310	0.514	14.066	0.368	784	27
	1.061	0.489	13.377	0.268	800	29
	1.288	0.479	13.581	0.340	761	28
	1.037	0.405	10.881	0.271	802	33
	1.037	0.437	11.706	0.263	809	32
	1.074	0.440	11.477	0.286	826	32
	1.100	0.487	13.259	0.299	797	29
	1.562	0.513	12.864	0.421	837	30
	1.137	0.447	13.384	0.289	729	28
	1.134	0.763	19.999	0.363	839	23
	1.051	0.928	24.528	0.392	837	21
P-794	1.293	0.410	10.376	0.314	837	34
	1.771	0.340	8.334	0.304	847	40
	2.112	0.518	12.990	0.427	837	30
	2.234	0.529	13.280	0.607	806	28
	1.745	0.433	10.781	0.415	829	33
	1.405	0.278	6.897	0.240	842	46
	2.239	0.510	12.303	0.664	819	29
	2.144	0.561	14.105	0.499	829	28
	1.606	0.408	10.863	0.167	832	34
	1.591	0.407	10.697	0.168	843	35
	1.770	0.360	9.370	0.297	811	36

6.5 Zircon Age Determination:

U-Pb LA-ICP-MS zircon geochronology from one representative Phulad granite sample (P-647) was carried out using a Resonetics Resolution M-50 series 193nm excimer laser ablation system equipped with a Laurin Technic Pty S-155 ablation cell at Activation Laboratories, Ancaster, Ontario, Canada. The data were standardized against FC1 zircon (1099 ± 2 Ma) which was analyzed at least 16 times per run and distributed evenly throughout the sequence.

Each ablation lasted for 30 seconds and was preceded by 30 seconds of background collection. The data were reduced offline using VizualAge (Petrus and Kamber, 2012) and Iolite v2.5 (Paton et al., 2011) running as plugins in Wavemetrics Igor Pro 6.23. Concentration data were calculated relative to NIST610 (distributed throughout the sequence) and using the Iolite trace-elements "internal standardization" data reduction scheme. All diagrams were produced using the Isoplot V3.0 program of Ludwig [4.1]. The representative analytical data are shown in table 6.2.

Table 6.2: LA-ICP-MS U–Pb Zircon age data of Phulad Granite (Sample no-647).

PPM			Ratio with error						U-Pb age (Ma)					
Pb	U	Th	$^{207}Pb/^{206}Pb$	±2σ	$^{207}Pb/^{235}U$	±2σ	$^{206}Pb/^{238}U$	±2σ	$^{207}Pb/^{206}Pb$	±2σ	$^{207}Pb/^{235}U$	±2σ	$^{206}Pb/^{238}U$	±2σ
95	1451	3034	0.0698	0.0052	1.213	0.099	0.126	0.002	921	140	806	45	766	10
34	1452	495	0.0700	0.0057	1.291	0.110	0.136	0.002	940	160	843	49	822	10
89	2627	412	0.0718	0.0017	1.114	0.025	0.113	0.002	977	47	759	12	689	13
145	1145	235	0.0673	0.0032	1.236	0.074	0.135	0.002	862	89	820	34	817	13
30	890	44	0.0663	0.0016	1.201	0.026	0.132	0.001	821	53	802	12	798	6
107	2590	506	0.0676	0.0033	1.274	0.047	0.139	0.002	846	100	836	22	838	13
157	2150	419	0.0686	0.0036	1.301	0.082	0.141	0.002	883	110	844	36	847	10

Zircon grains in Phulad granite (P-647) are mostly euhedral, 70–200 µm in length with aspect ratio varies between 2 to 4 (Figures 6.13-6.18). Zircon grains are optically clear, colourless and inclusion free. Cathodoluminescence (CL) images clearly show the magmatic oscillatory zoning and do not show any overgrowth textures. The morphology and their internal structure suggest that they are magmatic in origin and therefore the ages obtained are taken to represent the timing of granite crystallization. Both the core and rim were analyzed from this magmatic zircon grains to confirm the crystallization age. Data plot of

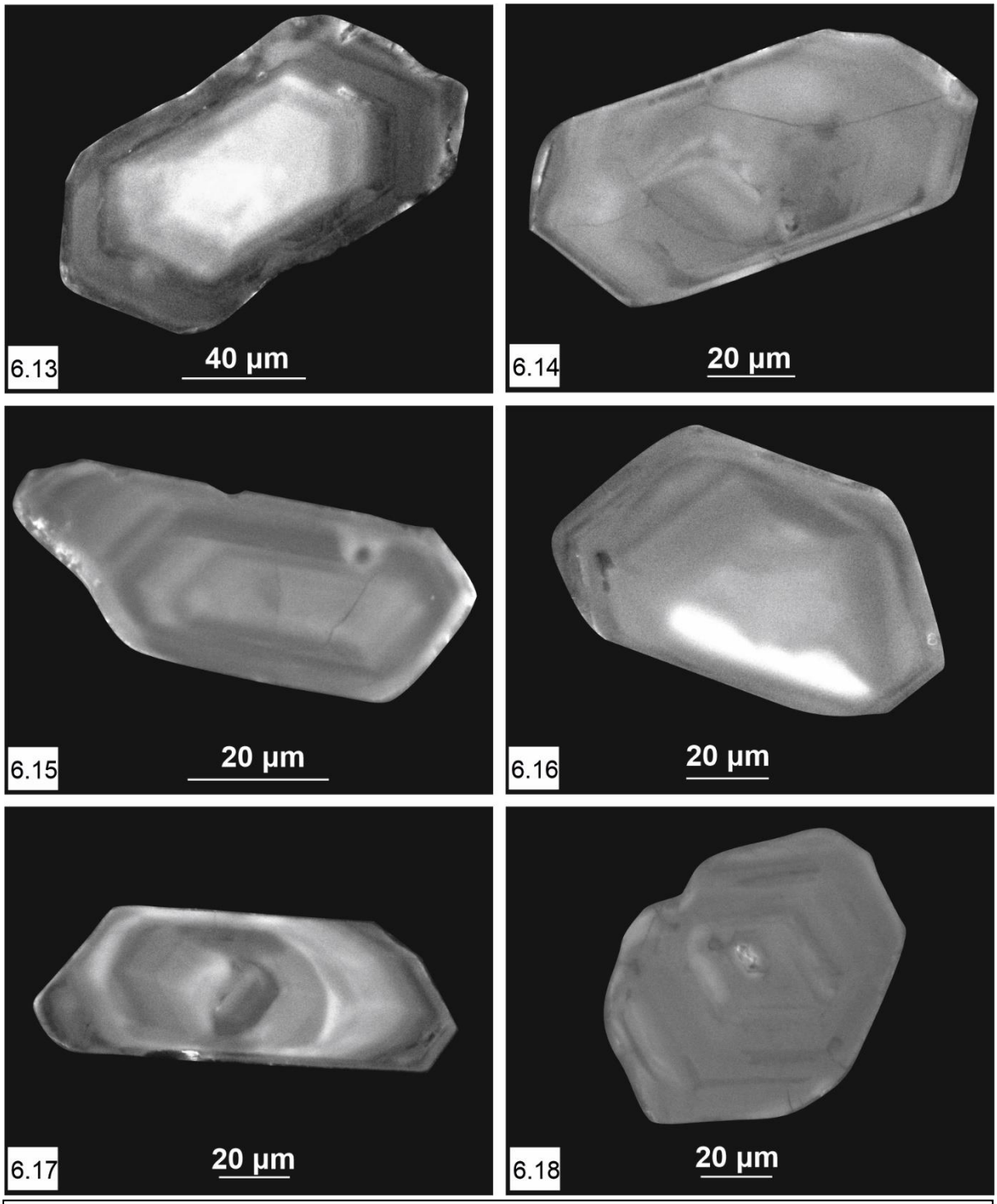

Figure 6.13-6.18: Photomicrographs in Cathodoluminescence (CL) image of zircon grains of Phulad granite.

$^{206}Pb/^{238}U$ and $^{207}Pb/^{235}U$ ratios in Concordia diagram gives an upper intercept age of 818±18 Ma with MSWD = 0.83 (Figure 6.19). The weighted average of $^{206}Pb/^{238}U$ of near Concordia data is 816±27 Ma with MSWD = 21 (Figure 6.20). Though the numbers of ablated zircon

grains are statistically low (N=7) nevertheless their morphology, internal structure and concordant data confirms their magmatic age.

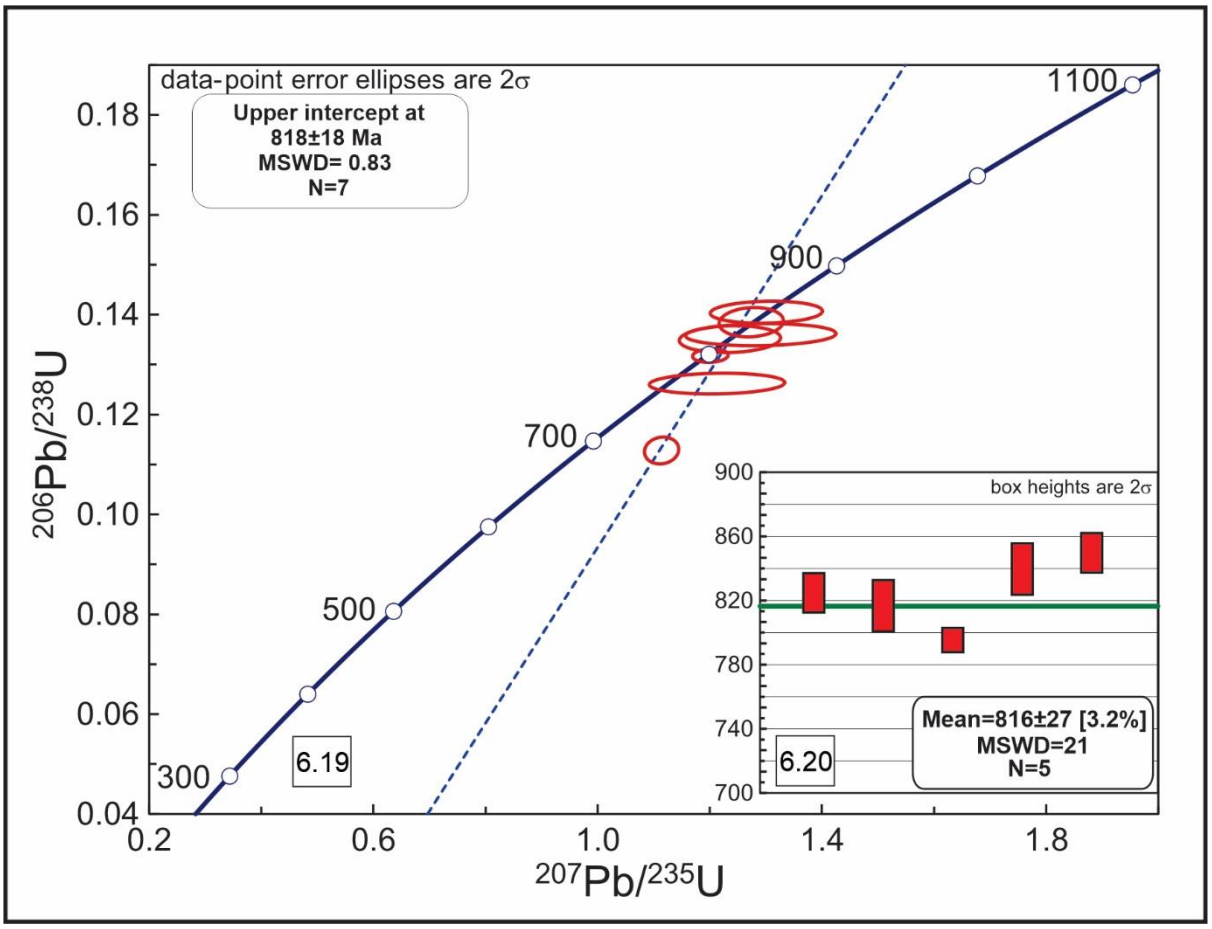

Figure 6.19-6.20: Concordia diagram (6.19) showing the upper intercept age of 818 ± 18 Ma (MSWD = 0.83) and weighted average age (6.20) near concordia age is 816 ± 27 Ma (MSWD = 21).

Chapter 7

Discussion and Conclusions

7.1 Introduction:

The PSZ has a regional NE-SW trend with small bends of N-S orientations at regular intervals. This shear zone is characterized by steep southeasterly dipping mylonitic foliation and steep oblique stretching lineation. The PSZ has developed in a ductile transpression with a top-to-the-NNW reverse sense of movement. The Phulad granite, which intrudes the PSZ and its wall rocks, is variably deformed with well-developed solid-state fabric.

Megacrysts of K-feldspar from Phulad granite show aligned euhedral shapes with planar crystal faces, moreover, microgranitoid enclaves also have a parallel orientation with aligned K-feldspar megacrysts. Microstructures under transmitted light microscope suggesting the igneous origin of the megacrysts. Some of the megacrysts contain euhedral shaped inclusions of plagioclase, quartz and micaceous minerals which correlate with Igneous precursors. Moreover, it does not contain any kind of metamorphic or metasomatic growth, like inclusion trails and the absence of xenoblastic nature of the megacrysts suggests that the K-feldspar megacrysts in deformed Phulad granite are residual phenocryst, not porphyroblast.

7.2 Evidence of Magmatic Foliation in Phulad Granite:

At the mesoscopic scale, the Phulad granite shows a preferred alignment of euhedral feldspar phenocrysts with simple twin interfaces parallel to the direction of elongation (Figure 2.15). This feature is also obvious from the microscopic study (Figures 3.4, 4.6). To explain the rotation of these euhedral feldspar grains to a particular alignment, without interference with neighbouring minerals, enough melt must be present during deformation (Paterson et al., 1989). The elongated microgranitoid enclaves are aligned parallel to the direction of feldspar alignment (Figures 2.17, 4.3). All these features suggest evidence of magmatic flow (Paterson

et al., 1989) and the foliation defined by these aligned euhedral feldspar phenocrysts and microgranitoid enclaves are considered to represent magmatic foliation. Parallel to this magmatic foliation Phulad granite exhibits development of solid-state foliation indicating that they formed under same deformation. This further explains that the deformation was there before complete crystallization of the granite magma.

7.3 Evidence of Dilation in Transpression Shear Zone:

PSZ is not a perfectly planar, but rather curviplanar because of the change in regional orientation from NE-SW to N-S trends (Figure 2.8). Oblique reverse movement of PSZ produces a component of sinistral slip movement on the horizontal section (Figures 2.6, 2.7). This component of sinistral movement causes the development of zones of dilation in the left stepping N-S trending bend zone (releasing bend, Crowell, 1974) of PSZ. In this N-S oriented releasing bends the extension is along the E-W direction (Figure 7.1). The existence of dilation

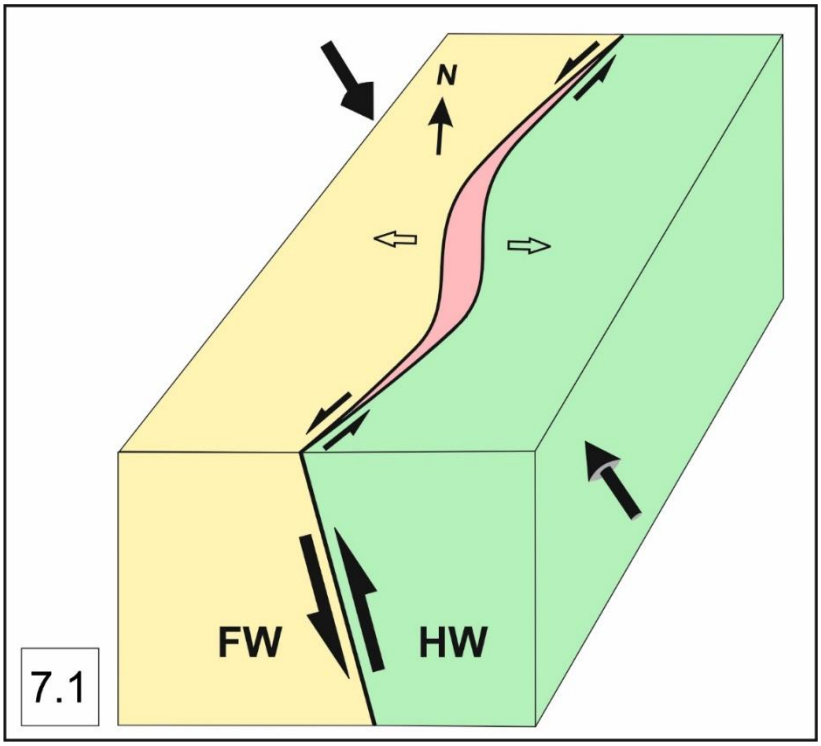

Figure 7.1: Schematic diagram showing the formation of dilation because of sinistral slip movement on horizontal section in the N-S trends.

is corroborated by occurrences of N-S trending pegmatite bodies in these N-S segments of PSZ (Hutton, 1982; McCaffrey, 1989, 1992; Ingram and Hutton, 1994) (Figures 7.2-7.5).

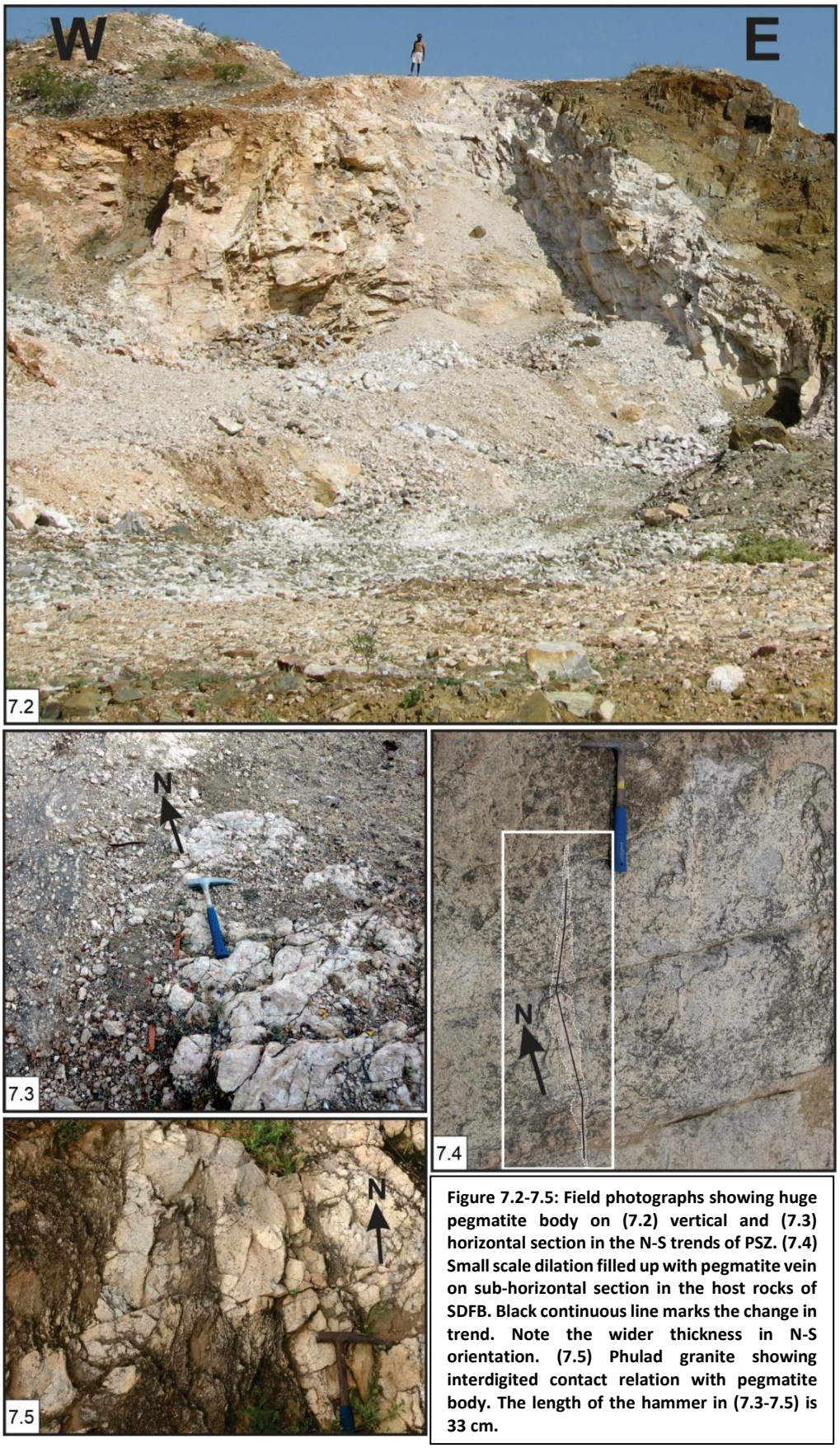

Figure 7.2-7.5: Field photographs showing huge pegmatite body on (7.2) vertical and (7.3) horizontal section in the N-S trends of PSZ. (7.4) Small scale dilation filled up with pegmatite vein on sub-horizontal section in the host rocks of SDFB. Black continuous line marks the change in trend. Note the wider thickness in N-S orientation. (7.5) Phulad granite showing interdigited contact relation with pegmatite body. The length of the hammer in (7.3-7.5) is 33 cm.

Since the N-S bends occur as fractal in nature so the size of these pegmatite bodies varies from 100's of meter to few cm depending on the size of the N-S bend (Figures 7.2-7.5). Also, mesoscopic N-S dilation within this regional NE-SW segment explains the occurrence of sheet like Phulad granites in the regional NE-SW segment of PSZ (Figure 2.13).

7.4 Evidence of Syn-Tectonic Emplacement of Phulad Granite:

The length of Phulad granite is more than 200 km long and ~6 km wide (maximum width 9 km) suggesting strong tabular body with long axis parallel to the shear zone (Figure 2.12). This remarkable narrowness of Phulad granite may be because of transpression shear zone extending along the orogen length (Crawford et al., 1987; McCaffrey, 1989, 1992; Ingram and Hutton, 1994; Hutton, 1997; Saint-Blanquat et al., 1998; Klepeis and Crawford, 1999; Nummer et al., 2007). The magmatic foliation and the solid-state foliation in the Phulad granite are parallel (Figures 2.15, 2.17, 2.31, 2.32). This solid-state foliation in Phulad granite is the same and continuous with regional foliation in the country rocks (Figures 2.10-2.11) and hence is considered as tectonic foliation. In the mesoscopic scale, the deformed feldspar phenocrysts of Phulad granite show evidence of stretching in both XZ and YZ sections, indicating a flattening type of deformation. The asymmetric tail patterns of deformed feldspar phenocrysts of Phulad granite on the XZ section show a top-to-the-NNW reverse sense of movement (Figure 2.40). Both the magmatic and tectonic foliation and lineation in Phulad granite show similarity in geometry and style with that of the regional foliation and lineation of PSZ. This implies that magmatic and tectonic foliation in Phulad granite and the mylonitic foliation of the shear zone country rocks has developed under the same progressive deformation and is broadly synchronous. Petrographic study reveals a range of well-

developed magmatic (Figures 3.3, 4.5), sub-magmatic (Figures 3.4-3.5), high temperature (chess board in quartz, figure 3.6) and solid-state deformation structures (Figures 3.7-3.8) in Phulad granite. The presence of quartz feldspar aggregates between fragmented primary feldspar grains provides evidence of deformation in presence of migrating melt (Bouchez et al., 1992) (Figures 3.5, 3.12, 4.7). The microstructural study provides evidence of deformation during the transition from magmatic-submagmatic to high temperature solid-state deformation in Phulad granite (Paterson et al., 1989; Miller and Paterson, 1994; Vernon, 2004). Both mesoscopic and microscopic features mentioned above show strong criteria for syn-tectonic emplacement of Phulad granite i.e., the granite emplaced during the shearing of PSZ prior to its complete crystallization (Paterson et al., 1989; Saint-Blanquat and Tikoff, 1997; Vernon et al., 2004).

The geochemical characteristics of the phulad granite suggest emplacement in a magmatic arc of syn-collisional set up. Also the present geochemical study of the Phulad granite of the Phulad Shear Zone suggests crustal origin that developed in a compressional tectonic setting. Coherent geochemical trend and similarities in the trace element behavior along with certain differences in the REE pattern suggest a key role of fractional crystallization during petrogenesis of these granites. The major and trace elements along with inter-elemental variation diagrams suggest a key role of fractional crystallization processes during petrogenesis of these granites. Trace element characteristics, REE and the tectonic discrimination diagrams reveal that they were derived from a predominant crustal source with a variable degree of mantle input. Volume gain and mass balance calculation indicates the effect of fluid at the shear zone.

U-Th-Pb (total) monazite and U-Pb zircon age determinations in Phulad granite indicate a magmatic age of 819.1 ± 4 Ma (MSWD = 1.3) and 818 ± 18 Ma (MSWD = 0.83) respectively.

EPMA monazite ages in the pegmatite bodies from the N-S bends of PSZ show 819.7 ± 4.5 Ma (MSWD = 2.1). All the dates overlap with the ~810 Ma shearing age of PSZ and 809 Ma metamorphic age of the SDFB (Chatterjee et al., 2017) implying that the crystallization of Phulad granite, shearing of PSZ and regional metamorphism of country rock is broadly synchronous. Granites showing similar structural features of equivalent age are reported from the areas that are close to the PSZ (Choudhury et al., 1984; Van Lente et al., 2009; Dharma Rao et al., 2013; Anand et al., 2018; Wang et al., 2018; Zhao et al, 2018). However, these granites are named differently, for example: porphyritic granite of Sai (808 ± 3.1 Ma SHRIMP U-Pb zircon age; Dharma Rao et al., 2013), Erinpura granite (807.3 ± 13.8 Ma U-Pb zircon age; Wang et al., 2018; 800 ± 2 Ma TIMS U-Pb zircon age, Van Lente et al., 2009), Balda granite (795 ± 11 Ma Rb-Sr age, Anand et al., 2018), Pali granite (811 ± 11.8 Ma U-Pb zircon age, Zhao et al., 2018).

7.5 Regional Implications:

The position and participation of the Greater India landmass within the Rodinia supercontinent have been widely questioned (Dalziel, 1991; Hoffman, 1991; Moores, 1991; Li et al., 1996, 2008; Radhakrishna and Mathew, 1996; Torsvik et al., 1996, 2001a, 2001b; Weil et al., 1998; Mezger and Cosca, 1999; Powell and Pisarevsky, 2002; Kröner and Cordani, 2003; Pisarevsky et al., 2003; Malone et al., 2008; Gregory et al., 2009; Bhattacharya et al., 2016). In this connection the tectonics of northwestern India has been extensively discussed and debated. Palaeomagnetic studies in the ~750 Ma Malani Igneous Suite (MIS) (Pareek, 1984; Eby and Kochhar, 1990; Pandit et al., 1999; Torsvik et al., 2001b) in the Marwar craton suggest that MIS-Seychelles-North Madagascar was a coherent terrane separated from the remaining parts of present-day Peninsular India at ~750 Ma (Torsvik et al., 2001a, 2001b; Tucker et al.,

2001). However, the timing and suturing of MIS hosting the Marwar craton with the remaining India remains speculative. Studies from northwestern India provide evidence of Grenvillian age collisional orogeny between the Marwar craton to the west and the North Indian block to the east (Deb et al., 2001; Bhowmik et al., 2009, 2010). Recent work of Chatterjee et al. (2017), based on textural controlled in-situ monazite age dating, showed that the Greater India landmass was accreted with the MIS hosted Marwar craton along PSZ at ~810 Ma. The present work reveals unequivocal evidence of syn-tectonic emplacement of Phulad granite

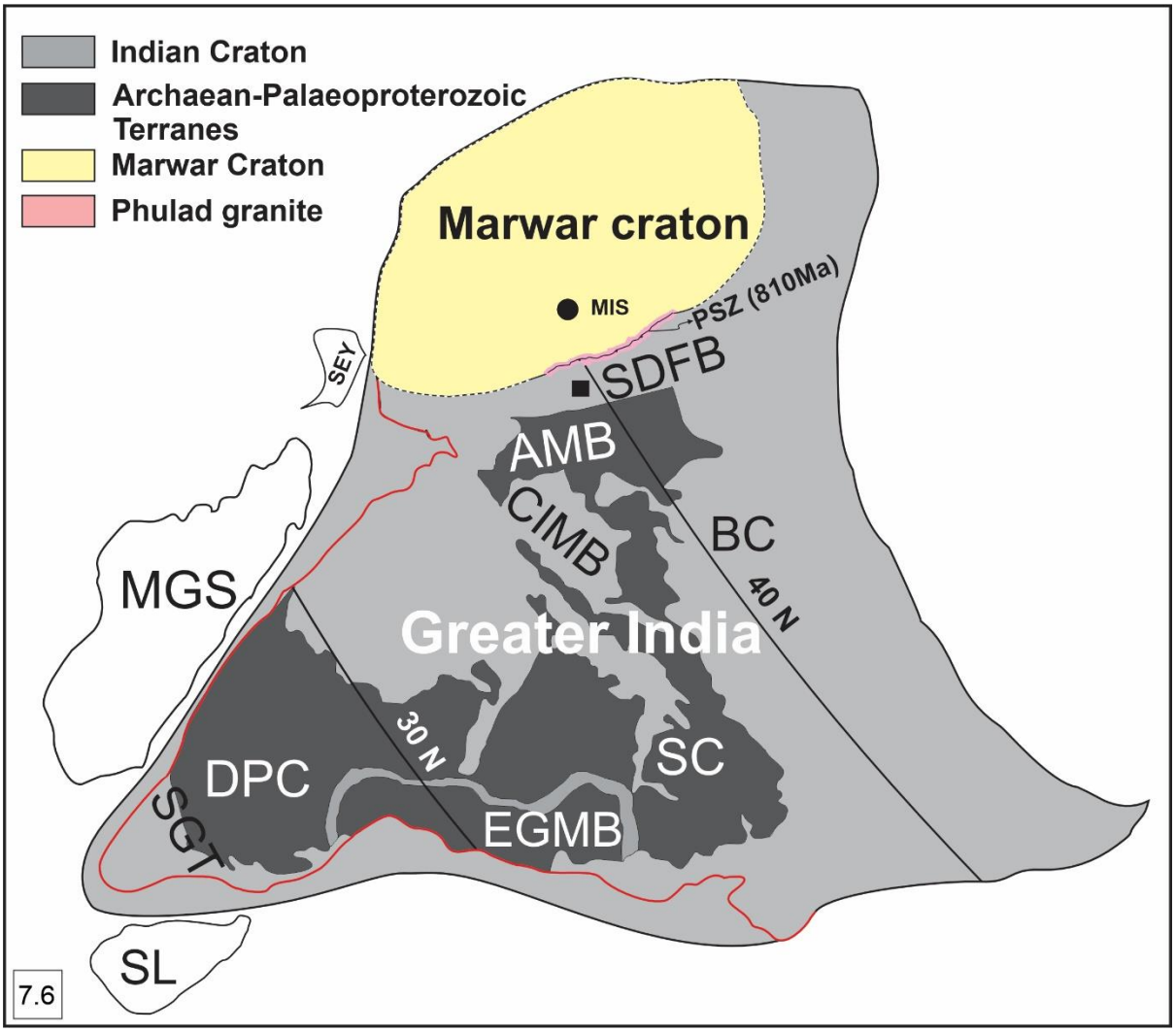

Figure 7.6: Geological map showing the position of stitching pluton (Phulad granite) at the contact (PSZ) of Marwar craton with the remaining part of the Greater India (modified after Torsvik et al., 2001a, 2001b; Collins and Pisarevsky, 2005). The width of the Phulad granite is exaggerated in the map. The palaeolatitude lines are superimposed from Meert (2003). The red line shows the outline of India. AMB: Aravalli Mobile Belt, BC: Bundelkhand Craton, CIMB: Central India Mobile Belt, DPC: Dharwar Protocontinent, EGMB: Eastern Ghats Mobile Belt, MGS: Madagascar, MIS: Malani Igneous suit, SDFB: South Delhi Fold Belt, PSZ: Phulad Shear Zone, SC: Singhbhum Craton, SEY: Seychelles, SGT: Southern Granulite Terrane, SL: Sri Lanka.

during the shearing of PSZ, and the granite also intrudes both the rocks of the Marwar craton and SDFB. Since PSZ is the suture that joins the Marwar craton with the remaining part of India, therefore, Phulad granite is suggested to represent a syn-tectonic stitching pluton (Mittwede, 1988; Johnson and Kattan, 2001; Han et al., 2010) (Figure 7.6). This further implies that the Marwar craton and SDFB were not contiguous before the mid-Neoproterozoic. The fact that the Marwar craton and the remaining part of the Greater Indian terrane were contiguous during the mid-Neoproterozoic provides an important constraint on paleogeographic reconstructions of the Greater India. Data of this work indicate that releasing bends of N-S orientation of PSZ causes the dilation and played an important role to provide the space required for syn-tectonic emplacement of Phulad granite in a transpression regime. Present work suggests that Phulad granite acted as a stitching pluton during suturing of the Marwar craton with the remaining India to form the Greater India along PSZ at 810 – 820 Ma.

References

Ague, J.J. (1994). Mass transfer during Barrovian metamorphism of pelites, southcentral Connecticut. II: Channelized fluid flow and the growth of staurolite and kyanite. American Journal of Science, 294, 1061–1134.

Anand, S.V., Pandian, M.S., Balakrishnan, S., and Sivasubramaniam, R. (2018). Fluid inclusion, geochemical, Rb–Sr and Sm–Nd isotope studies on tungsten mineralized Degana and Balda granites of the Aravalli craton, NW India. Journal of Earth System Science, 127, 52.

Anderson, J.G.C. (1937). The Etive granite complex. Journal of the Geological Society, London, 93, 487–533.

Arslan, M., and Aslan, Z. (2006). Mineralogy, petrography and whole-rock geochemistry of the Tertiary granitic intrusions in the Eastern Pontides, Turkey. Journal of Asian Earth Sciences, 27(2), 177–193.

Bailey, C.M., Simpson, C., and De Paor, D.G. (1994). Volume loss and tectonic flattening strain in granitic mylonites from the Blue Ridge province, central Appalachians. Journal of Structural Geology, 16, 1403–1416.

Baker, B.H., Goles, G.G., Leeman, W.P., and Lindstrom, M.M. (1977). Geochemistry and petrogenesis of basalt benmoreite -- trachyte suite from the southern part of the Gregory Rift, Kenya. Contributions to Mineralogy & Petrology, 64, 303-332.

Barker, F., and Arth, J.G. (1976). Generation of Trondhjemitic-Tonalitic Liquids and Archean Bimodal Trondhjemite-Basalt Suites. Geology, 4, 596–600. https://doi.org/10.1130/0091-7613(1976)4<596:GOTLAA>2.0.CO;2.

Barker, F. (1979). Trondhjemite: definition, environment and hypotheses of origin, in: Barker, F. (ed.), Trondhjemites, Dacites and Related Rocks. Elsevier Amsterdam, pp. 1–12.

Barraud, J., Gardien, V., Allemand, P., and Grandjean, P. (2001). Analog Modelling of Melt Segregation and Migration During Deformation. Physics and Chemistry of the Earth (A), 26(4-5), 317–323.

Bateman, P.C., Clark, L.D., Huber, N.K., Moore, J.G., and Rinehart, C.D. (1963). The Sierra Nevada Batholith--a synthesis of recent work across the central part. United States Geological Survey Professional Paper, 414-D: D1- D46.

Bell, T.H., and Jhonson, S.E. (1989). The role of deformation partitioning in the deformation and recrystallization of plagioclase and K-feldspar in the Woodroffe Thrust mylonite zone,

central Australia. Journal of Metamorephic Geology, https://doi.org/10.1111/j.1525 1314.1989.tb00582.x.

Berlin, R., and Henderson, C.M.B. (1969). The distribution of Sr and Ba between the alkaii feldspar, plagioclase and groundmass phases of prophyritictrachytes and phonolites. Geochimica et Cosmochimica Acta, 33, 2, 247–255.

Bhattacharya, A., Das, H.H., Bell, E., Bhattacharya, A., Chatterjee, N., Saha, L., and Dutt, A. (2016). Restoration of Late Neoarchean-Early Cambrian tectonics in the Rengali orogen and its environs (eastern India): The Antarctic connection. Lithos, 263, 190–212.

Bhowmik, S.K., Bernhardt, H.J., and Dasgupta, S. (2010). Grenvillian age high-pressure upper amphibolite-granulite metamorphism in the Aravalli-Delhi Mobile Belt, Northwestern India: New evidence from monazite chemical age and its implication. Precambrian Research, 178,168–184.

Bhowmik, S.K., Saha, L., Dasgupta, S., and Fukuoka, M. (2009). Metamorphic phase relations in orthopyroxene-bearing granitoids: implication for high-pressure metamorphism and prograde melting in the continental crust. Journal of Metamorphic Geology, 27, 295-315.

Bhushan, S.K. (1995). Late Proterozoic continental growth: Implications from geochemistry of acid magmatic events of West Indian craton, Rajasthan. Geological Survey of India Memorandum, 34, 339–355.

Bose, N., and Mukherjee, S. (2020). Estimation of deformation temperatures, flow stresses and strain rates from an intra-continental shear zone: The Main Boundary Thrust, NW Himalaya (Uttarakhand, India). Marine and Petroleum Geology, 112, 104094.

Bose, N., Dutta, D., and Mukherjee, S. (2018). Role of grain-size in phyllonitisation: Insights from mineralogy, microstructures, strain analyses and numerical modeling. Journal of Structural Geology, 112, 39–52.

Bouchez, J L., Delas, C., Gleizes, G., Nédélec A., and Cuney, M. (1992). Submagmatic microfractures in granites. Geology, 20, 35–38.

Breeding, C.M., and Ague, J.J. (2002). Slab-derived fluids and quartz vein formation in an accretionary prism, Otago Schist, New Zealand. Geology, 30, 499–502.

Brown, M., and Solar, G.S. (1998). Granite ascent and emplacement during contractional deformation in convergent orogens, Journal of Structural Geology, 20, 9–10.

Büttner, S.H. (1999). The geometric evolution of structures in granite during continuous deformation from magmatic to solid-state conditions: An example from the central European Variscan Belt. American Mineralogist, 84, 1781–1792.

Chatterjee, S.M., Roy Choudhury, M., Das, S., and Roy, A. (2017). Significance and dynamics of the Neoproterozoic (810 Ma) Phulad Shear Zone, Rajasthan, NW India. Tectonics, 36, 1432–1454. https://doi.org/10.1002/2017TC004554.

Choudhary, A.K., Gopalan, K., and Sastry, C.A. (1984). Present status of the geochronology of the Precambrian rocks of Rajasthan. Tectonophysics, 105, 131–140.

Collins, A.S., and Pisarevsky, S.A. (2005). Amalgamating eastern Gondwana: The evolution of the Circum Indian Orogens. Earth Science Review, 7, 229–270.

Condie, K.C., and Sinha, A.K. (1996). Rare earth and other trace element mobility during mylonitization: a comparison of the Brevard and Hope Valley shear zones in the Appalachian Mountains, USA. Journal of Metamorphic Geology, 14, 213–226.

Coulson, A.L. (1933). The Geology of Sirohi State, Rajputana, Geological Society of India Memorandum, 63, 166.

Crawford, A.R. (1970). The Precambrian geochronology of Rajasthan and Bundelkhand, Northern India. Canadian Journal of Earth Science, 7, 91–110.

Crawford, M.L., Hollister L.S., and Hollister, L.S. (1987). Crustal deformation and Regional metamorphism across a terrane boundary, Coast Plutonic Complex, British Columbia. Tectonics, 6(3), 343–361.

Cross, A.J., Kidder, S., and Prior, D.J. (2015a). Using microstructures and TitaniQthermobarometry of quartz sheared around garnet porphyroclasts to evaluate microstructural evolution and constrain an Alpine Fault Zone geotherm. Journal of Structural Geology, 75, 17–31. https://doi.org/10.1016/j.jsg.2015.02.012.

Cross, A.J., Ellis, S., and Prior, D.J. (2015b). A phenomenological numerical approach for investigating grain size evolution in ductiley deforming rocks. Journal of Structural Geology, 76, 22-34. https://doi.org/10.1016/j.jsg.2015.04.001.

Crowell, J.C. (1974). Origin of late Cenozoic basins in southern California. In: Dickinson, W. R. (ed.), Tectonics and sedimentation, 22, 190-204, Special Publication Society of Economic Palaeontologists and Mineralogists. Tulsa, Oklahoma.

Crowley, J.L., Chatterjee, N., Bowring, S.A., Sylvester, P.J., Myers, J.S., and Searle, M.P. (2005). U–(Th)–Pb dating of monazite and xenotime by EMPA, LA-ICPMS, and IDTIMS: Examples

from the Yilgarn Craton and Himalayas, in 15th Annual Goldschmidt Conference, Abstract A19.

Cruden, A.R. (1998). On the emplacement of tabular granites, Journal of the Geological Society, London, 155, 853–862.

D'Lemos, R.S., Brown, M., and Strachan, R.A. (1992). Granite magma generation, ascent and emplacement within a transpressional orogen, Journal of Geological Society, London, 149, 487–490.

Dalziel, I.W.D. (1991). Pacific margins of Laurentia and East Antarctica–Australia as conjugate rift pair: Evidence and implications for an Eocambrian supercontinent. Geology, 19, 598–601.

De la Roche, H., Leterrier, J., Grandclaude, P., and Marchal, M. (1980). A Classification of Volcanic and Plutonic Rocks Using R1-R2 Diagrams and Major Element Analyses—Its Relationships with Current Nomenclature. Chemical Geology, 29, 183–210. http://dx.doi.org/10.1016/0009-2541(80)90020-0.

De Wall, H., Pandit, M.K., and Chauhan, N.K. (2012). Paleosol at the archean –proterozoic contact in udaipur, Precambrian Research, 216, 120-131. doi:10.1016/j.precamres.2012.06.017.

De Wall, H., Pandit, M.K., Sharma, K.K., Schöbel, S., and Just, J. (2014). Deformation and granite intrusion in the Sirohi area, SW Rajasthan - constraints on Cryogenian to Pan-African crustal dynamics of NW India. Precambrian Research, 254, 1–18.

De Wall, H., Regelous, A., Schulz, B., Hahn, G., Bestmann, M., and Sharma, K.K. (2022). Neoproterozoic geodynamics in NW India – evidence from Erinpura granites in the South Delhi Fold Belt. International Geology Review, 64(8), 1051–1080.

Deb, M., Thorpe, R.I., Kristic, D., Corfu, F., and Davis, D.W. (2001). Zircon U-Pb and galena Pb isotope evidence for an approximate 1.0 Ga terrane constituting the western margin of the Aravalli-Delhi orogenic belt, northwestern India. Precambrian Research, 108, 195–213.

Dharma Rao, C.V., Santosh, M., Kim, S.W., and Li, S. (2013). Arc magmatism in the Delhi Fold Belt: SHRIMP U-Pb zircon ages of granitoids and implications for Neoproterozoic convergent margin tectonics in NW India. Journal of Asian Earth Sciences, 78, 83–99.

Dickson, F.W. (1966). Growth of K-feldspar and plagioclases by replacement processes in rocks of the Papoose Flat pluton and in country rocks, Inyo Mountains, California (abstr). In:

Cooper AR, Fahey PL (eds) Geology and ore deposits of the American Cordillera. Geol Soc Am Spec Pap 101:53.

Dickson, F.W. (1996). Porphyroblasts of barium-zoned K-feldspar and quartz, Papoose Flat, Inyo Mountains, California; genesis and exploration implications. In: Coyner AR, Fahey PL (eds) Geology and ore deposits of the American Cordillera, Reno, NV, United States. Geological Society of Nevada, Reno, 909–924.

Durand, C., Oliot, E., Marquer, D., and Sizun, J.P. (2015). Chemical mass transfer in shear zones and metacarbonate xenoliths: a comparison of four mass balance approaches. European Journal of Mineralogy, 27, 731–754.

Eby, G.N., and Kochhar, N. (1990). Geochemistry and petrogenesis of the Malani igneous suite, Northern India. Journal of Geological Society of India, 36, 109–130.

Eggleton, R.A., Halford, G.E., and Beams, S.D. (1979). Hiortdahlite from Jingera, New South Wales. Journal of the Geological Society of Australia, 26:1-2, 81–85, doi: 10.1080/00167617908729069.

Eggleton, R.A., and Buseck, P.R. (1980). The orthoclase-microcline inversion: A high-resolution transmission electron microscope study and strain analysis. Contribution to Mineralogy and Petrology, 74, 123–133, https://doi.org/10.1007/BF01131998.

Emmermann, R. (1968). Differentiation and metasomatose des albal - ganits (Sudschwarz-wald): Neues Jahrbuchfiir Mineralogie Abhandlungen, 109, 94–130.

Fazio, E., Fiannacca, P., Russo, D., and Cirrincione, R. (2020). Submagmatic to solid-state deformation microstructures recorded in cooling granitoids during exhumation of ate-Variscan crust in North-Eastern Sicily. Geosciences, 10, 311. https://doi.org/10.3390/geosciences10080311.

Flinn, D. (1962). On folding during three- dimensional progressive deformation: Quarterly Journal of the Geological Society of London, v. 118, p. 385– 428, https:// doi .org /10 .1144 /gsjgs .118 .1 .0385.

Forte, A.M., and Bailey, C.M. (2007). Testing the utility of the porphyroclast hyperbolic distribution method of kinematic vorticity analysis. Journal of Structural Geology, 29, 983–1001.

Fossen, H., Tikoff, B., and Teyssier, C.T. (1994). Strain modeling of transpressional and transtensional deformation, NorskGeologiskTidsskrift, 74, 134–145.

Frost, B.R., Barnes, C.G., Collins, W.J., Arculus, R.J., Ellis, D.J., and Frost, C.D. (2001). A Geochemical Classification for Granitic Rocks. Journal of Petrology, 42(11), 2033–2048.

Fry, N. (1979). Random point distributions and strain measurement in rocks. Tectonophysics, 60(1-2), 89– 105, https:// doi .org /10 .1016 /0040 -1951 (79) 90135-5.

Gangopadhyay, P.K., and Lahiri, A. (1986). Some problems on geochronology of the Precambrian rocks of Rajasthan: an appraisal. Indian Journal of Earth Science, 13, 169-188.

Gerald, J.D.F., and McLaren, A.C. (1982). The microstructures of microcline from some granitic rocks and pegmatites. Contribution to Mineralogy and Petrology, 80, 219–229. https://doi.org/10.1007/BF00371351.

Ghosh, S.K. (1987). Measure of non-coaxiality. Journal of Structural Geology, 9, 111-113.

Ghosh, S.K., and Ramberg, H. (1976). Reorientation of inclusions by combination of pure shear and simple shear. Tectonophysics, 34, 170.

Ghosh, S.K., Hazare, S., and Sengupta, S. (1999). Planar, non-planar and refolded sheath folds in the Phulad Shear Zone, Rajasthan. Journal of Geological Society of India, 21, 1715–1729.

Ghosh, S.K., Sen, G., and Sengupta, S. (2003). Rotation of long tectonic clasts in transpressional shear zones. Journal of structural geology, 25, 1083–1096.

Ghosh, S., Bose, S., Mandal, N., and Dasgupta, S. (2017). Dynamic recrystallization mechanisms and their transition in the Daling Thrust (DT) zone, Darjeeling–Sikkim Himalaya. Tectonophysics, 674, 166–181.

Gilbert, G.K. (1906). Gravitational assemblage in granite. Bulletin of the Geological Society of America, 17, 321–328.

Glazner, A.F., and Johnson, B.R. (2013). Late crystallization of K-feldspar and the paradox of megacrystic granites. Contribution to Mineralogy and Petrology, 166:777–799. doi: 10.1007/s00410-013-0914-1.

Golani, P.R., Reddy, A.B., and Bhattacharjee, J. (1998). The Phulad Shear Zone in Central Rajasthan and Its Tectonostratigraphic Implications, edited by B. S. Paliwal, 272–278, The Indian Precambrian, Scientific Publishers (India), Jodhpur, India.

Goodwin, L.B., and Tikoff, B. (2002). Competency contrast, kinematics, and the development of foliations and lineations in the crust. Journal of Structural Geology, 24(6), 1065-1085.

Grant, J.A. (1986). The isocon diagram; a simple solution to Gresens' equation for metasomatic alteration. Economic geology, 81, 1976–1982.

Grant, J.A. (2005). Isocon analysis: a brief review of the method and applications. Physics and Chemistry of the Earth, 30, 997–1004. https://doi.org/10.1016/j.pce.2004.11.003.

Gregory, L.C., Meert, J.G., Bingen, B., Pandit, M.K., and Torsvik, T.H. (2009). Paleomagnetism and geochronology of the Malani igneous suite, Northwest India: Implications for the configuration of Rodinia and the assembly of Gondwana. Precambrian Research, 170, 13–26.

Greiling, R.O., de Wall, H., Sadek, M.F., and Dietl, C. (2014). Late Pan-African granite emplacement during regional deformation, evidence from magnetic fabric and structural studies in the Hammamat–Atalla area, Central Eastern Desert of Egypt. Journal of African Earth Sciences, 99, 109–121.

Gresens, R.L. (1967). Composition-volume relationships of metasomatism. Chemical Geology, 2, 47–65.

Gromet, L. Peter, and Silver, Leon T. (1983). Rare earth element distributions among minerals in a granodiorite and their petrogenetic implications. Geochimica et Cosmochimica Acta, 47 (5), 925–939. ISSN 0016-7037.

Guineberteau, B., Bouchez, J.L., and Vigneresse, J.L. (1987). The Mortagne Granite Pluton (France) emplaced by pull-apart along a shear zone: structural and gravimetric arguments and regional implication. Geological Society of America Bulletin, 99, 763–770.

Guo, J., and Green, T.H. (1989). Barium partitioning between alkali feldspar and silicate liquid at high temperature and pressure. Contribution to Mineralogy and Petrology, 102, 328–335. https://doi.org/10.1007/BF00373726.

Gupta, S.N., Arora, Y.K., Mathur, R.K., Iqbaluddin, B.P., Prasad, B., Sahai, T.N., and Sharma, S.B. (1980). Lithostraigraphic map of Aravalli Region, southern Rajasthan and northeastern Gujrat: Geological Survey of India, Calcutta.

Gupta, P., Fareeduddin, Reddy, M.S., and Mukhopadhyay, K. (1995). Stratigraphy and structure of Delhi Supergroup of rocks in central part of Aravalli Range, Geological Survey India. 120(2-8), 12–26.

Han, B.F., Guo, Z.J., Zhang, Z.C., Zhang, L., Chen, J.F., and Song, B. (2010). Age, geochemistry, and tectonic implications of a late Paleozoic stitching pluton in the North Tian Shan suture zone, western China. Geological Society of America Bulletin, 122(3-4), 627–640.

Heier, K.S. and Taylor, S.R. (1959). Distribution of Ca, Sr and Ba in southern Norwegian alkali feldspars. Geochimica et Cosmochimica Acta, 17(3-4), 286--304.

Heron, A.M. (1953). The geology of central Rajputana, Geological Survey of India Memranadam, 79, 1–389.

Higgins, N.C., and Kawachi, Y. (1977). Microcline megacrysts from the Green Lake Granodiorite, eastern Fiordland, New Zealand. New Zealand Journal of Geology and Geophysics, 20: 273-286.

Hirth, G., and Tullis, J. (1992). Dislocation creep regimes in quartz aggregates. Journal of Structural Geology, 14, 145–159.

Hobbs, B.E., Means, W.D., and Williams, P.F. (1976). An Outline of Structural Geology. John Wiley & Sons, Inc., New York.

Hoffman, P.F. (1991). Did the breakout of Laurentia turn Gondwanaland inside out? Science, 252, 1409–1412.

Holyoke, C.W., and Kronenberg, A.K. (2010). Accurate differential stress measurement using the molten salt cell and solid salt assemblies in the Griggs apparatus with applications to strength, piezometers and rheology. Tectonophysics, 494, 17–31. https://doi.org/10.1016/j.tecto. 2010.08.001.

Hutton, D.H.W. (1982). A tectonicmodel for the emplacement of the Main Donegalgranite, N.W. Ireland. Journal of Geological Society, London, 139, 615–631.

Hutton, D.H.W. (1988a). Granite emplacement mechanism and tectonic controls: Inferences from deformation studies. Royal Society Ed Trans, 79, 245–255.

Hutton, D.H.W. (1988b). Igneous emplacement in a shear zone termination: The biotite granite at Strontian, Scotland. Geological Society of America Bulletin, 100, 1392–1399.

Hutton, D.H.W., Dempster, T.J., Brown, P.E., and Becker, S.D. (1990). A new mechanism of granite emplacement: Intrusion in active extensional shear zones. Nature, 343,452–455.

Hutton, D.H.W., and Reavy, R.J. (1992). Strike-slip tectonics and granite pedogenesis. Tectonics, 11, 960–967.

Hutton, D.H.W. (1996). The 'spaceproblem' in the emplacement of granite, Episodes, 19(4), 114-119.

Hutton, D.H.W. (1997). Syntectonic granites and the principle of effectivestress: A general solution to the space problem? In J. L. Bouche, et al. (Eds.), Granite: From Segregation of Melt to Emplacement Fabrics, (189-197), Petrology and Structural Geology Series (Volume 8. 358 pp). Dordrecht, Boston, London: Kluwer.

Ingram, G.M., and Hutton, D.H.W. (1994). The Great Tonalite Sill: Emplacement into a contractional shear zone and implications for Late Cretaceous to early Eocene tectonics in southeastern Alaska and British Columbia. Geological Society of America Bulletin, 106, 715–728.

Irvine, T.N., and Baragar, W.R.A. (1971). A Guide to the Chemical Classification of the Common Volcanic Rocks. Canadian Journal of Earth Science, 8, 523–548.

Johnson, B.R., and Glazner, A.F. (2009). Formation of K-feldspar megacrysts in granodioritic plutons by thermal cycling and late-stage textural coarsening. Contribution to Mineralogy and Petrology. DOI 10.1007/s00410-009-0444-z.

Johnson, P.R., and Kattan, F. (2001). Oblique sinistral transpression in the Arabian shield: the timing and kinematics of a Neoproterozoic suture zone. Precambrian Research, 107, 117–138.

Just, J., Schulz, B., De Wall, H., Jourdan, F., and Pandit, M.K. (2011). Monazite CHIME/EPMA dating of granitoid deformation: implications for Neoproterozoic tectono-thermal evolution of NW India. Gondwana Research, 19, 402–412.

Kalita, P., Goswami, T.K., Phukon, P., and Srivastava, H.B. (2022). Deformation temperature, differential stress, and strain rate variation across the Bomdila Gneiss, western Arunachal Himalaya, India. International Journal of Earth Sciences, 111, 607–622. https://doi.org/10.1007/s00531-021-02132-7.

Karlstrom, K.E. (1989). Toward a syntectonic paradigm for granitoids. EOS, 70, 32, 762.

Kawachi, Y., and Sato, T. (1978). Orthoclase magacrysts in the Yakushima granite, southern Kyushu, Japan. N. Jb. Miner. AM., 132, 136–152.

Kerrick, D.M. (1969). K-feldspar megacrysts from porphyritic quartz monzonite, central Sierra Nevada, California. American Mineralogist, 54, 839–848.

Klepeis, K.A., and Crawford, M.L. (1999). High-temperature arc-parallel normal faulting and transtension at the roots of an obliquely convergent orogen. Geology, 27(1), 7–10.

Kretz, R. (1966). Grain-size distribution for certain metamorphic minerals in relation to nucleation and growth. The Journal of Geology, 74(2), https://doi.org/10.1086/627152.

Kröner, A., and Cordani, U.G. (2003). African, southern Indian and South American cratons were not part of the Rodinia supercontinent: Evidence from field relationships and geochronology. Tectonophysics, 375, 325–352.

Kruhl, J.H. (1996). Prism- and basal-plane parallel subgrain boundaries in quartz: a microstructural geothermobarometer. Journal of Metamorphic Geology 14, 581–589. http://dx.doi. org/10.1046/j.1525-1314.1996.00413.x.

Kruhl, J.H., and Nega, M. (1996). The fractal shape of sutured quartz grain boundaries: application as a geothermometer. Geologische Rundschau, 85, 38–43.

Kuryvial, R.J. (1976). Element partitioning in alkali feldspars from three intrusive bodies of the central Wasatch Range, Utah. Geological Society of America Bulletin, 87, 657–660.

Law, R.D., Knipe, R.J., and Dayan, H. (1984). Strain-path partitioning within thrust sheets: microstructural and petrofabric evidence from the Moine thrust zone at Loch Eriboll, northwest Scotland. Journal of Structural Geology, 6, 477–497.

Law, R.D., Schmid, S.M., and Wheeler, J. (1990). Simple shear deformation and quartz crystallographic fabrics: a possible natural example from the Torridon area of NW Scotland. Journal of Structural Geology, 12, 29–45.

Li, Z.X., Zhang, L., and Powell, C.M. (1996). Positions of the East Asian cratons in the Neoproterozoic supercontinent Rodinia. Australian Journal Earth Sciences, 43, 593-604.

Li, Z.X., et al. (2008). Assembly, configuration, and break-up history of Rodinia: A synthesis. Precambrian Research, 160, 179–210.

Lister, G.S., and Snoke, A.W. (1984). S-C mylonites. Journal of Structural Geology, 6, 617-638.

Long, P.E., and Luth, W.C. (1979). Petrogenesis of microcline megacrysts from Precambrian granitic rocks of the Dixon-Penasco area, northern New Mexico, New Mexico Geological Society, 145-153. https://doi.org/10.56577/FFC-30.145.

Louis, E., Guinea, F., and Flore, F. (1986). The fractal nature of fracture. In Fractals in Physics, eds L. Pietronero and E. Tosatti, 177–180. Elsevier, Amsterdam.

Ludwig, K.R. (2003). Isoplot/EX version 3.0, A geochronological toolkit for Microsoft Excel, Berkeley Geochronology Center Special Publication, Berkeley, Calif.

Maggi, M., Rossetti, F., Ranalli, G., and Theye, T. (2014). Feedback between fluid infiltration and rheology along a regional ductile-to-brittle shear zone: the East Tenda Shear Zone (Alpine Corsica). Tectonics, 33, 253–280. https://doi.org/10.1002/2013TC003370.

Malone, S.J., Meert, J.G., Banerjee, D.M., Pandit, M.K., Tamrat, E., Kamenova, G.D., Pradhana, V.R., and Sohl, L.E. (2008). Paleomagnetism and detrital zircon geochronology of the Upper Vindhyan sequence, Son Valley and Rajasthan, India: A ca. 1000 Ma closure age for the Purana Basins? Precambrian Research, 164, 137–159.

Mamtani, M.A., and Greiling, R.O. (2010). Serrated quartz grain boundarie, temperature and strain rate: testing fractal techniques in a syntectonic granite. Geological Society London Special Publications, 332, 35–48. https://doi.org/10.1144/SP332.3.

Martin, H. (1999). Adakitic magmas: modern analogues of Archean granitoids. Lithos, 46, 411–429.

Martins, H.C.B., Sant'Ovaia, H., and Noronha, F. (2013). Late-Variscan emplacement and genesis of the Vieira do Minho composite pluton, Central Iberian Zone: Constraints from U-Pb zircon geochronology, AMS data and Sr-Nd-O isotope geochemistry. Lithos, 162-163, 221–235.

McCaffrey, K.J.W. (1989). The emplacement and deformation f granitic rocks in a transpressional shear zone: The Ox Mountains Igneous Complex, Ph.D. dissertation Univ. of Durham, Durham, England.

McCaffrey, K.J.W. (1992). Igneous emplacement in a transpressive shear zones: Ox Montains igneous complex. Journal of Geological Society London, 149, 221–235.

McDonough, W.F., and Sun, S.S. (1995). The composition of the Earth, Chemical Geology, 120(3–4), 223–253.

McKenzie, D. (1979). Finite deformation during fluid flow. Geophysical Journal of the Royal Astronomical Society, 58, 689–715.

Means, W.D., Hobbs, B.E., Lister, G.S., and Williams, P.F. (1980). Vorticity and non-coaxiality in progressive deformations. Journal of Structural Geology, 2, 371–378.

Meert, J.G. (2003). A synopsis of events related to the assembly of eastern Gondwana. Tectonophysics, 362, 1–40.

Meert, J.G., Pandit, M.K., and Kamenov, G.D. (2013). Further geochronological and paleomagnetic constraints on Malani (and pre-Malani) magmatism in NW India. Tectonophysics, 608, 1254–1267.

Mehnert, K.R., and Buesch, W. (1981). The Ba-content of K-feldspar megacrysts in granites: a criterion for their formation. Neues Jahrbuch für MineralogieAbhandlungen, 140, 221–252.

Merle, O., and Vendeville, B. (1995). Experimental modelling of thin-skinned shortening around magmatic intrusions. Bulletin of Volcanology, 57, 33-43.

Mezger, K., and Cosca, M.A. (1999). The thermal history of the Eastern Ghats Belt (India) as revealed by U–Pb and 40Ar/39Ar dating of metamorphic and magmatic minerals: Implications for the SWEAT correlation. Precambrian Research, 94, 251–271.

Michels, Z.D., Kruckenberg, S.C., Davis, J.R., and Tikoff, B. (2015). Determining vorticity axes from grain-scale dispersion of crystallographic orientations, Geology, 43 (9), 803–806.

Middlemost, E.A.K. (1994). Naming Materials in the Magma/Igneous Rock System. Earth-Science Reviews, 37, 215-244. doi: http://dx.doi.org/10.1016/0012-8252(94)90029-9.

Mittwede, S.K. (1988). Ultramafites, Melanges, and Stitching granites as suture markers in the central piedmont of the southern Appalachians. Journal of Geology, 96, 693-708.

Montel, J.M., Foret, S., Veschambre, M., Nicollet, C., and Provost, A. (1996). Electron microprobe dating of monazite. Chemical Geology, 131(1-4), 37–53.

Moore, J.G., and Sisson, T.W. (2008). Igneous phenocrystic origin of K-feldspar megacrysts in granitic rocks from the Sierra Nevada batholith. Geosphere, 4(2), 387-400 https://doi.org/10.1130/GES00146.1.

Moores, E.M. (1991). Southwest U.S.–East Antarctic (SWEAT) connection: A hypothesis, Geology, 19(5), 425–428.

Mukherjee, S. (2017). Review on symmetric structures in ductile shear zones. International Journal of Earth Sciences, 106, 1453–1468.

Mulchrone, K.F., and Mukherjee, S. (2016). Kinematics and shear heat pattern of ductile simple shear zones with 'slip boundary condition'. International Journal of Earth Sciences, 105, 1015–1020.

Němec , D. (1975). Barium in K-feldspar megacrysts from granite and syenitic rocks of the Bohemian Massif. Tschermaks Mineralogie und Petrographische Mitteilungen, 22, 109–116.

Newman, J., and Mitra, G. (1993). Lateral variations in mylonite zone thickness as influenced by fluid-rock interactions, Linville falls fault, North Carolina. Journal of Structural Geology, 15, 849–863. https://doi.org/10.1016/0191-8141(93)90180-I.NJ, USA.

Nummer, A.R., Machado, R., and Dehler, N.M. (2007). Pluton emplacement in a releasing bend in a transpressive regime: the arrozal granite in the Paraíba do Sul shear belt, Rio de Janeiro. Annals of the Brazilian Academy of Sciences, 79(2), 299–305.

O'Hara, K. (1988). Fluid flow and volume loss during mylonitization: an origin for phyllonite in an overthrust setting NC, USA. Tectonophysics, 156, 21–36.

Pandit, M.K., Shekhawat, L.S., Ferreira, V.P., Sial, A.N., and Bohra, S.K. (1999). Trondhjemite and Granodiorite assemblage from west of Barmer: Probable basement for Malani Magmatism in western India. Geological Society of India, 53, 89–96.

Pareek, H.S. (1984). Pre-quaternary geology and mineral resources of northwestern Rajasthan, Memoir Geological Survey of India, 115, 99.

Parsons, A.J., Coleman, M.J., Ryan, J.J., Zagorevski, A., Joyce, N.L., Gibson, H.D., and Larson, K.P. (2018). Structural evolution of a crustal-scale shear zone through a decreasing temperature regime: The Yukon River shear zone, Yukon-Tanana terrane, Northern Cordillera. Lithosphere, 10, 760–782.

Passchier, C.W., and Trouw, R.A.J. (1996). Journal of Petrology, 38, 971–972, Microtectonics, by C.W. Passchier and R.A.J. Trouw. Springer-Verlag, Berlin 1996. ISBN 3540587136. 289 p. Hardback. DM 64.00.

Passchier, C.W., and Trouw, R.A.J. (2005). Microtectonics; Springer: Berlin/Heidelberg, Germany, ISBN 3-540-64003-7.

Paterson, S.R., Vernon, R.H., and Tobisch, O.T. (1989). A review of criteria for the identification of magmatic and tectonic foliations in granitoids. Journal of Structural Geology, 11, 349–363.

Paterson, S.R., Fowler, T.K., Schmidt, K.L., Yoshinobu, A.S., Yuan, E.S., and Miller, R.B. (1998). Interpreting magmatic fabric patterns in plutons. Lithos, 44, 53–82.

Paton, C., Hellstrom, J.C., Paul, B., Woodhead, J.D., and Hergt, J.M. (2011). Iolite: Freeware for the visualisation and processing of mass spectrometric data. Journal of Analytical Atomic Spectrometry, 26, 2508–2518.

Pearce, J.A., Harris, N.B.W., and Tindle, A.G. (1984). Trace Element Discrimination Diagrams for the Tectonic Interpretation of Granitic Rocks. Journal of Petrology, 25(4), 956–983.

Petford, N., Cruden, A.R., McCaffrey, K.J.W., and Vigneresse, J.L. (2000). Granite magma formation, transport and emplacement in the Earth's crust. Nature, 408, 669–673.

Petrus, J.A., and Kamber, B.S. (2012). VizualAge: A novel approach to laser ablation ICP-MS U-Pb geochronology data reduction. Geostandards and Geoanalytical Research, 36, 247–270.

Pierozynski, W.J., and Henderson, C.M.B. (1978). Distribution of Sr, Ba and Rb between alkali feldspar and silicate melt. In: Mackenzie WS (ed) Progress in experimental petrology. NERC Publ Ser D 11, 40–46.

Pisarevsky, S.A., Wingate, M.T.D., Powell, C.M., Johnson, S., and Evans D.A.D. (2003). Models of Rodinia assembly and fragmentation, in Proterozoic East Gondwana: Supercontinent Assemblyand Breakup, Geological Society of London, Special Publications, 206, edited by M. Yoshida, B. F. Windley, and S. Dasgupta, 35–55, London.

Pitcher, W.S. (1997). The Nature and Origin of Granite. 1-377, Chapman & Hall, Landon.

Poirier, J.P. (1985). Creep of Crystals, Cambridge University Press, Cambridge.

Powell, C.M., and Pisarevsky, S. A. (2002). Late Neoproterozoic assembly of East Gondwana. Geology, 30, 3–6.

Prabhakar, N. (2013). Resolving poly-metamorphic Paleoarchean ages by CHIME dating of monazites using multi-spectrometer U, Th and Pb analyses and sub-counting methodology. Chemical Geology, 347, 255–270.

Pryer, L.L., and Robin, P.-Y.F. (1995). Retrograde metamorphic reactions in deforming granites and the origin of flame perthite. Journal of Metamorphic Geology, 14, 645–658.

Pryer, L.L., and Robin, P.-Y.F. (1996). Differential stress control on the growth and orientation of flame perthite: A palaeostress-direction indicator. Journal of Structural Geology, 18(9), 1151-1166, ISSN 0191-8141, https://doi.org/10.1016/0191-8141(96)00037-5.

Radhakrishna, T., and Mathew, J. (1996). Late Precambrian (850-800 ma) palaeomagnetic pole for the south Indian shield from the Harohalli alkaline dykes: Geotectonic implications for Gondwana reconstructions. Precambrian Research, 80, 77–87.

Ramsay, J.G. (1980). Shear zone geometry: a review. Journal of Structural Geology, 2,83–89.

Reavy, R.J. (1989). Structural controls on metamorphism and syn-tectonic magmatism: the Portuguese Hercynian collision belt. Journal of Geological Society, London, 146, 649–657.

Ring, U. (1999). Volume loss, fluid flow, and coaxial versus noncoaxial deformation in retrograde, amphibolite facies shear zones, northern Malawi, east-central Africa. GSA Bulletin, 111, 123–142.

Robin, P.Y.F., and Cruden, A.R. (1994). Strain and vorticity patterns in ideally ductile transpression zones. Journal of Structural Geology, 16, 447–466.

Rolland, Y., Cox, S., Boullier, A.M., Pennacchioni, G., and Mancktelow, N. (2003). Rare earth and trace element mobility in mid-crustal shear zones: insights from the Mont Blanc Massif (Western Alps). Earth and Planetary Science Letters, 214, 203–219. https://doi.org/10.1016/S0012-821X(03)00372-8.

Rollinson, H.R. (1993). Using geochemical data: Evaluation, presentation, interpretation. Longman Scientific and Technical, Wiley, New York, 352.

Roy Choudhury, M., Das, S., Chatterjee, S.M., and Sengupta, S. (2016). Deformation of footwall rock of Phulad Shear Zone, Rajasthan: Evidence of transpressional shear zone. Journal of Earth System Science, 125(5), 1033–1040.

Roy, A.B., and Sharma, K.K. (1999). Geology of the region around Sirohi Town, western Rajasthan-a story of Neoproterozoic evolution of the Aravalli crust. In: Paliwal, B.S. (Ed.),19–33. Geological Evolution of the Northwestern India. Scientific Publishers, Jodhpur, India.

Roy, A.B., and Jakhar, S.R. (2002). Mesoproterozoic Delhi Fold Belts, Geology of Rajasthan (Northwest India) Precambrian to recent India, 205. Jodhpur, Scientific Publishers.

Saint-Blanquat, M. de, and Tikoff, B. (1997). Development of Magmatic to Solid-State Fabrics during Syntectonic Emplacement of the Mono Creek Granite, Sierra Nevada Batholith, J.L. Bouchez et al. (eds.) 231–252, Granite: From Segregation of Melt to Emplacement, Kluwer Academic Publishers.

Saint-Blanquat, M. de, Tikoff, B., Teyssier, C., and Vigneresse, J.L. (1998). Transpressional kinematics and magmatic arcs. In: Holdsworth, R. E., Strachan, R. A. Dewzy, J. E (eds) 1998. Continental Transpressional and Transtensional Tectonics. Geological Society, London, Special Publications, 135, 327–340.

Saint-Blanquat, M. de, Law, R.D., Bouchez, J.L., and Morgan, S. (2001). Internal structure & emplacement of the Papoose Flat pluton: an integrated structural, petrographic & magnetic susceptibility study. Geological Society of America Bulletin, 113(8), 976-995.

Saint-Blanquat, M. de, Habert, G., Horsman, E., Morgan, S., Tikoff, B., Launeau, P., and Gleizes, G. (2006). Mechanisms and duration of non-tectonically-assisted emplacement in the upper-crust: The Black Mesa pluton, Henry Mountains, Utah. Tectonophysics, 428(1-4), 1–31.

Saint-Blanquat, M. de, Habert, G., Horsman, E., Law, R., Morgan, S., Tikoff, B., and Vanderhaeghe, O. (2011). Multiscale magmatic cyclicity, duration of pluton construction, and the paradoxical relationship between tectonism and plutonism in continental arcs. Tectonophysics, 500(1-4), 20–33.

Sen, S. (1980). Precambrian stratigraphic sequence in a part of the Aravalli range, Rajasthan: a reevaluation. The Quarterly Journal of the Geological, Mining, Metallurgical Society of India, 52(2), 67–76.

Sengupta, S., and Ghosh, S.K. (2004). Analysis of transpressional deformation from geometrical evolution of mesoscopic structures from Phulad shear zone, Rajasthan, India. Journal of Structural Geology, 26, 1961–1976.

Sengupta, S., and Ghosh, S.K. (2007). Origin of striping lineation and transposition of linear structures in shear zones. Journal of Structural Geology, 28, 273–287.

Sengupta, S., and Chatterjee, S.M. (2016). Microstructural variation in quartzofeldspathic mylonites and vorticity analysis using rotating porphyroclasts in Phulad Shear Zone, Rajasthan, India. in Ductile Shear Zones from Micro to Macro-Scales, edited by S. Mukherjee and K. Mulchrone, 128–140, Wiley Blackwell's, London.

Shand, S.J. (1943). Eruptive Rocks. Their Genesis Composition. Classification, and Their Relation to Ore-Deposits with a Chapter on Meteorite. John Wiley & Sons, New York.

Shand, S.J. (1949). Rocks of the Mid-Atlantic Ridge. The Journal of Geology, 57(1), 89–92.

Simpson, C., and Wintsch, R.P. (1989). Evidence for deformation-induced K-feldspar replacement by myrmekite. Journal of Metamorphic Geology, 7(2), 261–275.

Simpson, C., and De Paor, D.G. (1993). Strain and kinematic analysis in general shear zones. Journal of Structural Geology, 15, 1–20.

Simpson, C., and De Paor, D.G. (1997). Practical analysis of general shear zones using the porphyroclast hyperbolic distribution method: an example from the Scandinavian Caledonides. In: Sengupta, S. (Ed.), Evolution of Geological Structures in Micro- to Macro-Scales (169–184). London, Chapman and Hall.

Singh, Y.K., Waele, B.D., Karmakar, S., Sarkar, S., and Biswal, T.K. (2010). Tectonic setting of the Balaram-Kui-Surpagla-Kengora granulites of the South Delhi Terrane of the Aravalli Mobile Belt, NW India and its implication on correlation with the East African Orogen in the Gondwana assembly. Precambrian Research, 183, 669–688. doi: 10.1016/j.precamres.2010.08.005.

Singh, S., DeWaele, B., Shukla, A., Umasankar, B.H., and Biswal, T.K. (2021). Tectonic fabric, geochemistry and zircon- monazite geochronology as proxies to date an orogeny: Example of South Delhi orogeny, NW India and implications for East Gondwana tectonics. Frontiers in Earth Science, 8, (594355), doi:10.3389/feart.2020.594355.

Sinha-Roy, S. (1988). Proterozoic Wilson Cycles in Rajasthan. In: A.B. Roy (cd.) Precambrian of the Aravalli Mountain, Rajasthan, India, Geological survey of India memorandum. 7, 95–107.

Sinha-Roy, S., Mohanty, M., Malhotra, G., Sharma, V.P., and Joshi, D.W. (1993). Conglomerate horizons in south-central Rajasthan and their significance on Proterozoic stratigraphy and tectonics of the Aravalli and Delhi Fold Belts. Journal of Geological Society of India, 41, 331–350.

Sinha-Roy, S., Malhotra, G., and Guha, D.S. (1995). A transect across Rajasthan Precambrian terrain in relation to geology, tectonics and crustal evolution of south-central Rajasthan. In: Sinha-Roy, S. & Gupta, K. R. (Eds) Continental Crust of North Western and Central India. Memoir Geological Survey of India, 31, 63–90.

Sinha-Roy, S., Malhotra, G., and Guha, D.B. (1998). Geology of Rajasthan. Special Publish Geological Society of India. Bangalore, 262.

Spear, F.S., Pyle, J.M., and Cherniak, D. (2009). Limitations of chemical dating of monazite. Chemical Geology, 266, 218–230.

Stipp, M., Stünitz, H., Heilbronner, R., and Schmid, S.M. (2002a). The eastern Tonale fault zone: a “natural laboratory” for crystal plastic deformation of quartz over a temperature range from 250 to 700°C. Journal of Structural Geology, 24, 1861–1884.

Stipp, M., Stünitz, H., Heilbronner, R., and Schmid, S.M. (2002b). Dynamic recrystallisation of quartz: Correlation between natural and experimental conditions. Geological Society of London Special Publication, 200, 171–190. https://doi.org/10.1144/GSL.SP.2001.200.01.11.

Stipp, M., and Tullis, J., (2003). The recrystallized grain size piezometer for quartz. Geophysical Research Letters, 30, 2088, https://doi.org/10.1029/ 2003GL018444.

Stipp, M., Tullis, J., and Behrens, H. (2006). Effect of water on the dislocation creep microstructure and flow stress of quartz and implications for the recrystallized grain size piezometer. Journal of Geophysical Research Atmospheres, 111, B04201, https://doi.org/10.1029/2005JB003852.

Stipp, M., Tullis, J., Scherwath, M., and Behrmann, Jan H. (2010). A new perspective on paleo-piezometry: Dynamically recrystallized grain size distributions indicate mechanism changes. Geology, 38, 759–762. https://doi.org/10.1130/G31162.1.

Stone, M., and Austin, W.G.C. (1961). The metasomatic origin of the potash feldspar megacrysts in the granites of southwest England. The Journal of Geology, 69(4), 464–472.

Sugden, T.J., Deb, M., and Windley, B.F. (1990). The tectonic setting of mineralisation in the Proterozoic Aravalli–Delhi orogenic belt, NW India. In: Naqvi, S. M. (ed.) Precambrian Continental Crust and its Economic Resources, Amsterdam Elsevier, 367–390.

Sun, S.S., and McDonough, W.F. (1989). Chemical and Isotopic Systematics of Oceanic Basalts: Implications for Mantle Composition and Processes. In: Saunders, A.D., Norry, M.J., Eds., Magmatism in the Ocean Basins. Geological Society, London, Special Publications, 42, 313–345. https://doi.org/10.1144/GSL.SP.1989.042.01.19.

Sychanthavong, S.P.H., and Desai, S.D. (1977). Protoplate tectonics controlling the Precambrian deformations and metallogenic epochs of NW Peninsular India, Mineral Science Engineering, 9, 218–237.

Takahashi, M., Nagahama, H., Masuda, T., and Fujimura, A. (1998). Fractal analysis of experimentally, dynamically recrystallized quartz grains and its possible application as a strain rate meter. Journal of Structural Geology, 20, 269–275.

Tart`ese, R., Boulvais, P., Poujol, M., Chevalier, T., Paquette, J., Ireland, T.R., and Deloule, E. (2012). Mylonites of the South Armorican Shear Zone: insights for crustal-scale fluid flow and water – rock interaction processes. Journal of Geodynamics., 56, 86–107. https://doi.org/10.1016/j.jog.2011.05.003.

Taylor, S.R., Heier, K.S., and Sverdrup, P.L. (1960). Contribution to the mineralogy of Norway, No. 5. Trace element variations in three generations of feldspars from the Landsverk I pegmatite, Evje, southern Norway. Nor. Geol. Tidsskr., 40, 133--156.

Tewari, H.C., Divakarrao, V., Naryana, B.L., Dixit, M.M., Madhavrao, N., Murthy, A.S.N., Rajendraprasad, B., Reddy, P.R., Venkateswarlu, N., Vijayarao, V., Mishra, D.C., and Gupta, S.B. (1998). Nagaur-Jhalawar Geotransect across the Delhi/Aravalli fold belt in Northwest India. Journal of Geological Society of India, 52, 153–161.

Tikoff, B., and Fossen, H. (1995). The limitations of three-dimensional kinematic vorticity analysis. Journal of Structural Geology, 17, 1771–1784.

Tikoff, B., and Blanquat, M.D.S. (1997). Transpressional shearing and strike-slip partitioning in the Late Cretaceous Sierra Nevada magmatic arc, California. Tectonics, 16(3), 442–459.

Tikoff, B., and Greene, D. (1997). Stretching lineations in transpressional shear zones: An example from the Sierra Nevada Batholith, California. Journal of Structural Geology, 19, 29–39.

Torsvik, T.H., Smethurst, M.A., Meert, J.G., VanderVoo, R., McKerrow, W.S., Brasier, M.D., Sturt, B.A., and Walderhaug, H.J. (1996). Continental break-up and collision in the Neoproterozoic and Palaeozoic-A tale of Baltica and Laurentia, Earth Science Reviews, 40, 229–258.

Torsvik, T.H., Ashwal, L.D., Tucker, R.D., and Eide, E.A. (2001a). Neoproterozoic geochronology and palaeogeography of the Seychelles microcontinent: The India link. Precambrian Research, 110, 47–59.

Torsvik, T.H., Carter, L.M., Ashwal, L.D., Bhushan, S.K., Pandit, M.K., and Jamtveit, B. (2001b). Rodinia refined or obscured: Palaeomagnetism of the Malani igneous suite (NW India). Precambrian Research, 108, 319–333.

Trépied, L., Doukhan, J.C., and Paquet, J. (1980). Subgrain boundaries in quartz theoretical analysis and microscopic observations. Physics and Chemistry of Minerals, 5, 201–218. https://doi.org/10.1007/BF00348570.

Trullenque, G., Kunze, K., Heilbronner, R., Stünitz, H., and Schmid, S.M. (2006). Microfabrics of calcite ultramylonites as records of coaxial and non-coaxial deformation kinematics: examples from the Rocher de l'Yret shear zone (Western Alps). Tectonophysics, 424, 69–97.

Tucker, R.D., Ashwal, L.D., and Trosvik, T.H. (2001). U-Pb geochronology of Seychelles granitoids: A Neoproterozoic continental arc fragment. Earth planetary science letters, 185, 27–38.

Twiss, R.J. (1977). Theory and applicability of a recrystallized grain size paleopiezometer. Pure and Applied Geophysics, 115, 227–244.

Twiss, R.J., and Moores, E.M. (2007). Structural Geology. second ed. W.H. Freeman and Company, New York.

Van Lente B., Ashwal, L.D., Pandit, M.K., Bowring, S.A., and Torsvik, T.H. (2009). Neoproterozoic hydrothermally altered basaltic rocks from Rajasthan, northwest India: Implications for late Precambrian tectonic evolution of the Aravalli craton, Precambrian Research, 170, 202–222.

Vegas, N., Rodriguez., Cuevas, J., Siebel, W., Esteban, J.J., Túbia, J.M., and Basei, M. (2011). The sphene-centered ocellar texture: an effect of grain-supported flow and melt 762 migration in a hyperdense magma mush. The Journal of Geology, 119, 143–157.

Vernon, R.H. (2004). A Practical Guide to Rock Microstructure, Cambridge University Press, 1–606, ISBN-10 0521891337.

Vernon, R.H. (1968). Microstructures of High-grade Metamorpbic Rocks at Broken Hill, Australia. Journal of Petrology, 9(1),1–22.

Vernon, R.H. (1976). Metamorphic Processes. Reactions and Microstructure Development. Geological Magazine, 113, 394.

Vernon, R.H., Williams, V.A., and D'arcy, W.F. (1983). Grain-size reduction and foliation development in a deformed granitoid batholith. Tectonophysics, 92, 123–145.

Vernon, R.H. (1986). K-feldspar megacrysts in granites — Phenocrysts, not porphyroblasts. Earth-Sciences Reviews, 23(1), 1–63, https://doi.org/10.1016/0012-8252(86)90003-6.

Vernon, R.H. (1990). K-feldspar augen in felsic gneisses and mylonites - deformed phenocrysts or porphyroblasts? Geol Föreningens Stockholm Förhandlingar, 112,157–167.

Vernon, R.H. (1991). Questions about myrmekite in deformed rocks. Journal of Structural Geology, 13, 979–985.

Vernon, R.H. (1999). Quartz and feldspar microstructures in metamorphic rocks. The Canadian Mineralogist, 37(2), 513–524.

Vernon, R.H., and Paterson S.R. (2002). Igneous origin of K-feldspar megacrysts in deformed granite of the Papoose Flat Pluton, California, USA. Visual Geosciences, 7, 1–28, doi: 10.1007/s10069-002-0005-3.

Vernon, R.H., Johnson, S.E., and Melis, E.A. (2004). Emplacement-related microstructures in the margin of a deformed pluton: The San Jose´ tonalite, Baja California, Mexico. Journal of Structural Geology, 26(10), 1867-1884.

Vigneresse, J.L., Tikoff, B., and Ameglio, L. (1999). Modification of the regional stress field by magma intrusion and formation of tabular granitic plutons. Tectonophysics, 302, 203–224.

Vigneresse, J.L. (2006). Granitic batholiths: from pervasive and continuous melting in the lower crust to discontinuous and spaced plutonism in the upper crust. Transactions of the Royal Society of Edinburgh: Earth Sciences, 97, 311–324.

Volpe, A.M., and Macdougall, J.D. (1990). Geochemistry and isotopic characteristics of mafic (Phulad ophiolite) and related rocks in the Delhi Supergroup, Rajasthan, India: Implications for rifting in the Proterozoic. Precambrian Research, 48, 167–191.

Wang, W., Pandit, M.K., Zhao, J.H., Chen, W.T., and Zheng, J.P. (2018). Slab break-off triggered lithosphere – asthenosphere interaction at a convergent margin: The Neoproterozoic bimodal magamtism in NW India. Lithos, 296–299, 281–296.

Weijermars, R. (1991). The role of stress in ductile deformation. Journal of Structural Geology, 13, 1061–1078.

Weil, A.B., Vandervoo, R., Mac Niocaill, C., and Meert, J.G. (1998). The Proterozoic supercontinent Rodinia: Paleomagnetically derived reconstructions for 1100 to 800 Ma. Earth planetary science letters, 154, 13–24.

Whalen, J.B., Curie K.L., and Chappel, B.W. (1987). A-type granites: Geochemical characteristics, discrimination and petrogenesis. Contributions to Mineralogy and Petrology, 95, 407–419.

White, A.J.R. (1979). Sources of granite magmas. Geological Society of America, Abstracts with Programs, 11, 539.

Whitford, D.J. and Jezek, P.A. (1979). Origin of late Cenozoic lavas from the Banda arc, Indonesia: trace elements and Sr isotope evidence. Contribution to Mineralogy and Petrology, 68(2), 141–150.

Xypolias, P., and Koukouvelas, I.K. (2001). Kinematic vorticity and strain rate patterns associated with ductile extrusion in the Chelmos Shear Zone (External Hellenides, Greece). Tectonophysics, 338, 59–77.

Xypolias, P. (2009). Some new aspects of kinematic vorticity analysis in naturally deformed quartzites. Journal of Structural Geology, 31, 3–10.

Xypolias, P., Spanos, D., Chatzaras, V., Kokkalas, S., and Koukouvelas, I. (2010). Vorticity of flow in ductile thrust zones: examples from the Attico-Cycladic Massif (Internal Hellenides, Greece). In: Law, R. D., Butler, R. W. H., Holdsworth, R.E., Krabbendam, M., Strachan, R.A. (Eds.), Continental Tectonics and Mountain Building: The Legacy of Peach and Horne (687–714). London, Special Publish Geological Society.

Yonkee, W.A., Parry, W.T., and Bruhn, R.L. (2003). Relations between progressive deformation and fluid-rock interaction during shear-zone growth in a basement-cored thrust sheet, Sevier orogenic belt. Utah. American Journal of Science, 303, 1–59.

Zhao, J.H., Pandit, M.K., Wang, W., and Xia, X.P. (2018). Neoproterozoic tectonothermal evolution of NW India: Evidence from geochemistry and geochronology of granitoids. Lithos, 316–317, 330–346.

Zibra, I., Smithies, R.H., Wingate, M.T.D., and Kirkl, C.L. (2014). Incremental pluton emplacement during inclined transpression. Tectonophysics, 623, 100–122.

List of Publications Annexure –I

Publications from present research work

1. **Ayan Kumar Sarkar**, Anirban Manna, Sadhana M. Chatterjee, and Alip Roy (2023). Interpretation of deformation microstructures in syn-tectonic granite: insights from Phulad granite, Rajasthan, NW India. **Geosciences Journal**, doi: 10.1007/s12303-023-0028-3.

2. Sadhana M. Chatterjee, **Ayan Kumar Sarkar**, Alip Roy, and Anirban Manna (2020). Mid-Neoproterozoic tectonics of northwestern India: Evidence of stitching pluton along 810 Ma Phulad Shear Zone. **Tectonics**, 39, e2019TC005902, doi: 10.1029/2019TC005902.

3. Sadhana M. Chatterjee, Alip Roy, Anirban Manna, and **Ayan Kumar Sarkar** (2023). Early Neoproterozoic tectonics in the Marwar Crustal Block, NW India, the relevance of the Phulad Shear Zone, and implications for Rodinia reconstruction. **Geosphere**, 19 (4), 1080-1102, doi:10.1130/GES02565.1.

4. **Ayan Kumar Sarkar**, Soumyadip Chakraborty, and Sadhana M. Chatterjee (2023). Origin of K-feldspar megacryst in Phulad granite, is it porphyroclast or porphyroblast? (Submitted).

Other Publications

5. Upama Dutta, **Ayan Kumar Sarkar**, Sadhana M. Chatterjee, Anirban Manna, Alip Roy, and Subhrajyoti Das (2022). Implication of element redistribution on metamorphic phases: Insights from meta-granite of South Delhi Fold Belt, Rajasthan, India **Geological Magazine**, 159, 735-760, DOI: https://doi.org/10.1017/S0016756821001345.

6. Anirban Manna, Sadhana M. Chatterjee, **Ayan Kumar Sarkar,** and Alip Roy (2023). Polyphase deformation in a part of South Delhi Fold Belt, Rajasthan, NW India and its implications. **Journal of scientific research, BHU** (accepted).